Title	Quadrupole moment of the doubly-closed-shell-plus-one-nucleon uncleus 41Sc and its core deformation
Author(s)	福田, 茂一
Citation	大阪大学, 1995, 博士論文
Version Type	VoR
URL	https://doi.org/10.11501/3106801
rights	
Note	

Quadrupole moment of the doubly-closed-shell-plus-one-nucleon nucleus ^{41}Sc and its core deformation

Shigekazu Fukuda

Acknowledgments

The present paper aims at enabling the reader to obtain a concrete knowledge of the experiment of measuring nuclear moments. Attention is concentrated on the doubly-closed-shell-plus-one-nucleon nucleus ^{41}Sc and, especially, on its quadrupole moment and its core deformation.

The study on the magnetic moment of ^{41}Sc was achieved by many predecessors and the study enabled us to understand nuclear structure quantitatively. The present study on the quadrupole moment of ^{41}Sc enables us to discuss the core-deformation effect to the magnetic moment quantitatively. Anyway, I could not complete the present paper if there were not collaborations of the following persons.

Firstly, I would like to express my thanks to
Prof. T. Minamisono for giving me the chance to study in Van de Graaff accelerator facility in Osaka University and for his fruitful suggestions on my research works.
Associate Prof. Y. Nojiri for his constant collaboration, discussions, and encouragement.
Research Associate K. Matsuta for his constant collaboration, discussions, and encouragement.
Research Associate M. Fukuda for his constant collaboration, discussions, and encouragement.

As well as the above-mentioned researchers, I would like to express my thanks to the following engineers
Mr. Y. Takahashi for his technical supports for the Van de Graaff Accelerator and for preparations of the target.
Mr. M. Sakamoto for his technical supports for preparations and arrangements of the experimental apparatus.
Mr. H. Iwata and Mr. T. Mizuta for their technical supports and advises concerning electronic circuits for data-taking applied in the present experiments.
Mr. Onishi for his support for calculations by use of computers.

I would like to express my thanks to the following seniors and colleges:
Dr. A. Kitagawa for his technical advises concerning the data-taking program of the β-NMR technique.
Dr. T. Ohtsubo for his constant collaboration and discussions concerning hyperfine interactions in crystals.
Dr. S. Momota for his constant collaboration, discussions, and encouragement.
Mr. M. Tanigaki, Mr. T. Izumikawa, Mr. Y. Nakayama and Mr. K .Sato for their

constant collaboration.

Of course. I could not complete this paper, if not collaboration of the following theorists. I would like to express my thanks to

Prof. H. Akai for his theoretical advise concerning the hyperfine field calculations.

Prof. A. Arima for his theoretical advise concerning the nuclear interactions and nuclear moments.

Prof. H. Sagawa for his theoretical advise concerning the nuclear interactions and theoretical calculations.

Dr. H. Kitagawa for his theoretical advise concerning the nuclear structure.

In the present experiment, it was very important to determine the electric field gradient that Sc atoms feel in the substitutional site of Ti ions of TiO_2 crystal. I would like to express my thanks to

Research Associate S. Takeda for his advise and support for the measurement and analysis of the FT-NMR spectrum of the crystal with a mixture of ^{45}Sc. I also would like to express my thanks to

Mr, M. Yoshida and Mr. Y. Kano, Earth Jewelry Company for synthesizing ^{45}Sc doped TiO_2(Sc) single crystals.

In order to perform the calculation of the hyperfine constants by use of MCHF method, we must use the powerful computer such as a super computer. I thanks to the following institute, which gave me much CPU time free of charge

The Computer Center, Institute for Molecular Science, Okazaki National Research Institutes for the use of the HITACHI M-680H and NEC SX-3R.

Finally, my parents for their encouragement.

July 1995

Abstract

The nuclear quadrupole moment of ^{41}Sc($I^\pi = 7/2^-, T_{1/2} = 0.596$s) has been measured to be $|Q(^{41}\mathrm{Sc};7/2^-)| = 17.8 \pm 0.3$ fm^2, by using a modified β-NMR technique. In the process of obtaining this result, the field gradient effective to the Sc atoms substituted at Ti site in TiO_2 was measured by detecting the FT-NMR of ^{45}Sc in TiO_2, and also the Sternheimer effect was calculated for the atomic field gradient of Sc atoms. The nuclear quadrupole moments of Sc isotopes were, therefore, deduced as $Q(^{43}\mathrm{Sc}) = -23.9 \pm 3.8\mathrm{fm}^2$, $Q(^{44}\mathrm{Sc}) = +11.3 \pm 0.5\mathrm{fm}^2$, $Q(^{44m}\mathrm{Sc}) = -20.8 \pm 1.9\mathrm{fm}^2$, $Q(^{45}\mathrm{Sc}) = -23.6 \pm 0.2\mathrm{fm}^2$, and $Q(^{47}\mathrm{Sc}) = -23.9 \pm 3.8\mathrm{fm}^2$. By combining the value with its mirror quadrupole moment, $Q(^{41}\mathrm{Ca}; 7/2^-)$, it is shown that the valence proton in ^{41}Sc carries more than 85% of the moment, and that of the remaining core carries about 15%. This is consistent with a picture in which the core of ^{41}Sc, ^{40}Ca, is deformed by about $\delta = -1.5 \pm 0.2\%$.

Contents

List of Figures

List of Tables

Chapter 1

Introduction

1.1 Nuclear quadrupole moment of ^{41}Sc

Nuclear electric quadrupole moments have been important and indispensable clues for investigating the nuclear shell structure and nuclear interaction [1]. One of the recent targets of such experimental and theoretical studies has been mirror nuclei, by which the radial and angular nucleon distributions are investigated [2]. Of particular interest is the quadrupole moment of ^{41}Sc($I^{\pi} = 7/2^{-}, T_{1/2} = 0.596$s), partly because of the simple nuclear structure of that state, *i.e.*, the state comprises a doubly closed-shell core, the ground state of ^{40}Ca, and only one extra proton attached to it. One other reason is that the magnetic moment and quadrupole moment of its mirror partner, ^{41}Ca($I^{\pi} = 7/2^{-}$), have already been well studied both experimentally [36] and theoretically [1, 5, 6], as well as the magnetic moment of ^{41}Sc[4, 5, 6]. Therefore, the present study of the quadrupole moment with the help of those known quantities makes our understanding of the nuclear structure more precise. Also, this may give a key to quantitative studies of one of the current topics in nuclear physics, e.g., non-nucleonic degrees of freedom in the nucleus [4, 5, 6]. For a derivation of mesonic and quark effects from precisely determined magnetic moments of the mass A=39 and 41 mirror doublets, a finer understanding on the long-standing question of the softness of the Ca core must be solved. Without any definite knowledge concerning the nuclear deformation corrections [9, 40] to the isoscalar and isovecter magnetic moments, no conclusive knowledge can be extracted. In the following sections, the mesonic and quark effects, non-nucleonic degrees of freedom, in the nuclear magnetic moment are explained briefly. In addition to the definition of the quadrupole moment, the way to derive knowledge concerning a deformation of the Ca core from the quadrupole moment of ^{41}Sc and the relation of the core deformation and the magnetic moment are also explained.

1.1.1 Meson and quark effects in the nuclear magnetic moment

The deformation of the Ca core was studied by Gerace *et al.* in order to account for the large transition rates and the rotational character of the spectra of ^{40}Ca, ^{41}Ca, ^{42}Ca and ^{41}Sc [40]. An attempt was made to explain the low-lying levels of ^{40}Ca, ^{41}Ca, ^{42}Ca and ^{41}Sc as being mixtures of shell-model and deformed states. The deformed states were constructed using the isospin coupling scheme of Zamick, and the matrix elements between spherical and deformed state were calculated using the Hamada-Johnston nucleon-nucleon force. They were able to obtain the result that within this model the electromagnetic transition probabilities and single-particle strength, so far calculated, had all been in partial agreement with the observed values.

In addition to the study of the energy spectra of ^{40}Ca, a suggestion concerning core deformation was gained from a study of the magnetic moment [4]. As explained in detail in Appendix A, the quark deconfinement of the nucleus can be derived from the analysis of the isoscalar magnetic moment, $\mu^{(0)}$, around the doubly closed shells. The renormalization of the proton mass was about $\kappa = 3\%$ for the nucleus around the mass 16 and 40, which means the nucleon mass in the nuclei around A=16, 40 is less than that of the free nuclei by 3%. Since, fortunately, the isoscalar magnetic moment is independent of core deformations, such mass renormalization was clearly extracted. Regarding extracting the effective g-factors of protons and neutrons in nucleus, *i.e.*, mesonic effects, we need to use both isoscalar and isovector magnetic moments in the analysis. However, unfortunately, the isovector magnetic moment is more or less dependent on the correction due to the core deformation, $\delta\langle\mu^{(1)}\rangle_{def}$, because of its isovector nature. Therefore, we need knowledge on the core deformation of A=41 and 39 systems in order to extract the mesonic effects from the magnetic moments as well as on the configuration mixing of the valence nucleon in a spherical potential. Since the quadrupole moment is a good clues to know sensitive to the core deformation, the knowledge on the quadrupole moment is very essential for the above described studies.

1.1.2 Nuclear quadrupole moment

As a general definition of the quadrupole moment, we use the expectation value of $(3z^2-r^2)$, within the angular-momentum state $|JM\rangle$ with the maximal projection $J = M$. The quadrupole moment is written as

$$Q \equiv \langle J; M = J|\sqrt{\frac{16\pi}{5}}\sum_{i=1}^{A}\frac{e_i}{e}r_i^2 Y_2^0(\theta_i,\varphi_i)|J; M = J\rangle, \qquad (1.1)$$

or, using the Wigner-Eckart theorem, as

$$Q = \begin{pmatrix} J & 2 & J \\ -J & 0 & J \end{pmatrix} \sqrt{\frac{16\pi}{5}} \langle J \| \sum_{i=1}^{A} \frac{e_i}{e} r_i^2 \mathbf{Y}_2(\theta_i, \varphi_i) \| J \rangle, \tag{1.2}$$

where $e_i = 1$ for proton and $e_i = 0$ for neutron. Filling out the Wigner $3j$-symbol explicitly, one obtains the resulting expression

$$Q = \sqrt{\frac{J(2J-1)}{(2J+1)(2J+3)(J+1)}} \sqrt{\frac{16\pi}{5}} \langle J \| \sum_{i=1}^{A} \frac{e_i}{e} r_i^2 \mathbf{Y}_2(\theta_i, \varphi_i) \| J \rangle. \tag{1.3}$$

For the case of a pure single-particle configuration,

$$\begin{aligned} & \langle J \| \sum_{i=1}^{A} \frac{e_i}{e} r_i^2 \mathbf{Y}_2(\theta_i, \varphi_i) \| J \rangle \\ = & \frac{e_A}{e} \langle j \| \mathbf{Y}_2) \| j \rangle \langle r^2 \rangle \\ = & \frac{e_A}{e} (2j+1) \sqrt{\frac{5}{4\pi}} \frac{3/4 - j(j+1)}{\sqrt{j(j+1)(2j-1)(2j+1)(2j+3)}} \langle r^2 \rangle \end{aligned} \tag{1.4}$$

is deduced; putting this relation into equation 1.3, the single-particle quadrupole moment is written as

$$Q_{SP}(j) = -\frac{(2j-1)}{(2j+2)} \frac{e_A}{e} \langle r^2 \rangle. \tag{1.5}$$

For a particle moving outside of a closed shell, a negative quadrupole moment appears. This is because the particle density for a nucleon in an orbital with j, $m = j$ is localized in the equatorial plane, giving rise to an oblate distribution, as shown in figure 1.1. The absence of a particle (a hole) then corresponds to a prolate distribution, giving a positive quadrupole moment. In case of ^{41}Sc with a $0f_{7/2}$ proton particle moving outside of the ^{40}Ca core in the equatorial plane. Inserting the appropriate spin values we obtain

$$Q_{SP}(^{41}\mathrm{Sc}; 0f_{7/2}) = -\frac{2}{3} \langle r^2 \rangle. \tag{1.6}$$

Table 1.1 and Fig. 1.2 show the quadrupole moment of doubly-closed shell±1nucleon nuclei. Q_{SP} is a quadrupole moment, which was calculated based on the single-particle model. Q_{CM} is the quadrupole moment calculated by including the effect of configuration mixing [1]. e_{eff} is a effective charge defined as a ratio of the observed quadrupole moment to that of the single particle model, and the effective charges can be estimated by the calculation including the configuration mixing. Here, it should be noticed that Q_{CM} can reproduce the experimental value better than Q_{SP}, but not completely.

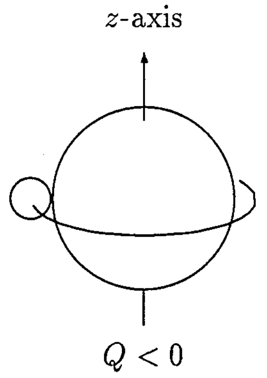

Figure 1.1: Quadrupole moment of the single-particle model
Single-particle quadrupole moment for a nucleon moving in the equatorial plane inducing an oblate mass distribution, relative to the z-axis.

Table 1.1: Q-moment of doubly-closed ±1 nucleon nuclei

nucleus	orbit	Q_{exp}	Q_{SP}	Q_{CM}	e_{eff}
^{17}F	$d_{5/2}(p;\pi)$	-10 ± 2	-6.37	-8.2	1.6 ± 0.3
^{17}O	$d_{5/2}(p;\nu)$	-2.578	-6.14	-2.7	0.42
^{39}K	$d_{3/2}(h;\pi)$	4.9 ± 0.4	5.38	6.95	0.91 ± 0.07
^{39}Ca	$d_{3/2}(h;\nu)$		-6.14	-2.7	
^{41}Sc	$f_{7/2}(p;\pi)$	$(-)17.8 \pm 0.3$	-11.0	-14.5	1.62 ± 0.03
^{41}Ca	$f_{7/2}(p;\nu)$	-9.00 ± 0.24	-10.6	-5.6	0.85 ± 0.02

1.1.3 Core deformation of ^{40}Ca

With respect to the nuclear quadrupole moment, the value of a state in a nucleus is given [2] by the sum of the quadrupole moments of the proton group and that of neutron group in the nucleus as

$$\begin{aligned} Q(N_p, N_n) &= \sqrt{\frac{16\pi}{5}} \Big[\langle \sum e_n^{eff} (\frac{1}{2} + t_z) r_i^2 Y_{20}(\Omega_i) \rangle \\ &\quad + \langle \sum e_p^{eff} (\frac{1}{2} - t_z) r_i^2 Y_{20}(\Omega_i) \rangle \Big] \\ &= e_n^{eff} \tilde{Q}(N_n) + e_p^{eff} \tilde{Q}(N_p), \end{aligned} \tag{1.7}$$

where $t_z = \frac{1}{2}\tau_z$ is the isospin operator. e_p^{eff} and e_n^{eff} are the effective charges for the proton and the neutron, respectively. The effective charge originates in an interaction between the valance nucleon and the inner core. It is obvious from the fact that the nucleus which

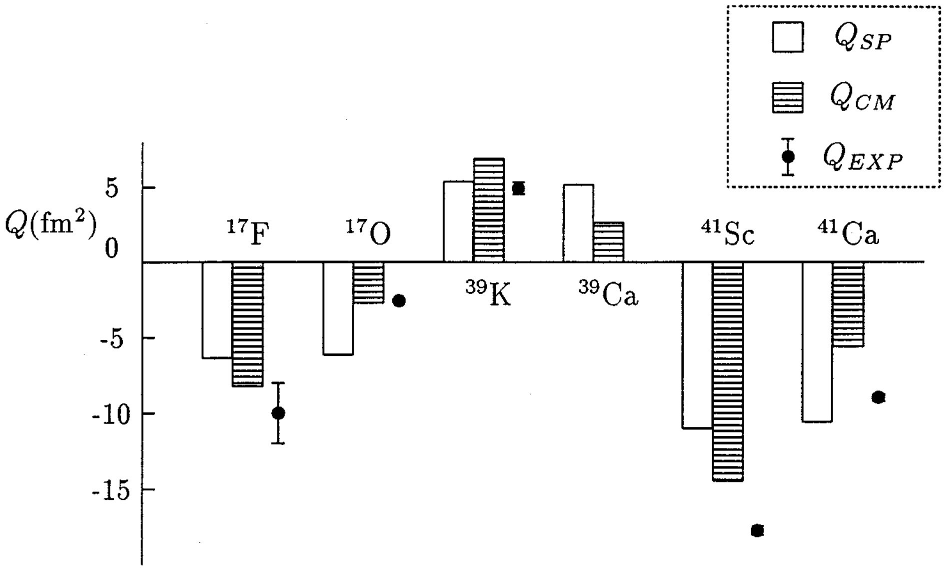

Figure 1.2: Q-moment of doubly-closed ±1 nucleon nuclei

has a neutron valance nucleon has a significant quadrupole moment, for example ^{17}O and ^{41}Ca. The effective charges $e_p^{eff} = +1.33$ and $e_n^{eff} = +0.64$ for protons and neutrons in the 0f1p shell have been given by Dahr and Bhatt [25] from their projected Hartree-Fock calculations, which reproduce the B(E2) data well. The values are similar to the effective charges obtained for light nuclei by Sagawa *et al.* [1], *i.e.*, $e_p^{eff} = +1.33$ end $e_n^{eff} = +0.52$ which were fixed so as to reproduce those nuclear properties of the sd-shell nuclei and the values $e_p^{eff} = +1.311$, $e_n^{eff} = +0.525$ obtained for the fp-shell nuclei in the same way. The difference in the effective charges obtained by Dahr and Bhatt and those by Sagawa lies in the calculation method, as explained in the discussion.

Their theoretical predictions of the quadrupole moment of ^{41}Sc and ^{41}Ca are listed in table 1.2. The difference between these theoretical calculations and an observed quadrupole moment gives direct information on a core deformation. Because these cal-

Table 1.2: Theoretical values of $\tilde{Q}(21)$ and $\tilde{Q}(20)$.

	$\tilde{Q}(21)_p$	$\tilde{Q}(21)_n$	e_p^{eff}	e_n^{eff}	$Q_{th}(^{41}\mathrm{Sc})$	$Q_{th}(^{41}\mathrm{Ca})$
Sagawa *et al.*	-11.0	-10.6	+1.311	+0.525	-14.5	-5.6
Richter *et al.*	-11.4	-11.4	+1.33	+0.64	-15.1	-7.3

culation were based on an assumption of a spherical Ca core and an experimental value includes the contribution from a core deformation. For the case of ^{41}Sc nuclei, the core deformation-effect to the quadrupole moment can make a contribution according to

$$Q_{exp}(^{41}\mathrm{Sc};7/2) = Q_{th}(p)e_p^{eff} + Q_{def}(\mathrm{Sc}). \tag{1.8}$$

In the same way, for ^{41}Ca nuclei, it can be obtained as

$$Q_{exp}(^{41}\mathrm{Ca};7/2) = Q_{th}(n)e_n^{eff} + Q_{def}(\mathrm{Ca}). \tag{1.9}$$

If we assume an oblate deformation,

$$\delta = \frac{R_z - R_x}{R_0}, \tag{1.10}$$

and a rotationally symmetric nucleus around z-axis with

$$R_0 = \frac{R_z - R_x}{2} \tag{1.11}$$

for the ^{40}Ca core, an extra quadrupole moment of

$$Q_{def} = \frac{2I-1}{2(I+1)} \cdot \frac{4}{3}\langle r^2\rangle Z\delta \ [\mathrm{fm}^2] \tag{1.12}$$

must be added to each value predicted by using only the valence nucleon in the calculation.

This core deformation can be described as a mixture of a single particle state and strongly-deformed states, and we can estimate a contribution to isovector magnetic moments originating from a core deformation with its deformed wave function. Originally, Gerace and Green introduced a deformed wave function into a single particle wave function in order to explain low-lying levels of ^{40}Ca, ^{41}Sc, and ^{41}Ca, and they used the mixed wave function of a single-particle wave function and a deformed wave function of $\beta = 0.25$ with a overlap factor of 0.15 as the ground state of ^{40}Ca [40]. Using this wave function, Arima and Shimizu *et al.* estimated the correction to a isovector magnetic moments and Gamow-Teller type β-decay matrix element $\langle \tau s\rangle$ in the $f_{7/2}$ orbit coming from the deformed states of the ^{40}Ca core, as listed in table 1.3 [7]. By using this correction of $\delta\langle\mu^{(1)}\rangle_{def}/\langle\mu^{(1)}\rangle_S$ and equation A.18, we can obtain a 8.4% less $g_s^{(1)}$ than a previous value including no correction due to a core deformation, which is in better agreement of a $g^{(1)}$ in A=16 system.

However, because the deformed wave function introduced by Gerace and Green included only 3p-2h states, the overlap factor, $\alpha = 0.15$, could be changed significantly, when including such higher order configurations as 5p-3h and so on. By measuring a quadrupole moment of ^{41}Sc nuclei, we can estimate this effect due to a core deformation, that is, we can determine the overlap factor, α, through the relation 1.8.

Table 1.3: Corrections to the isovector magnetic moment and $\langle \tau s \rangle$ coming from the deformed states of the ^{40}Ca core

	$\delta\langle \mu^{(1)} \rangle / \langle \mu^{(1)} \rangle_S$ (%)	$\delta\langle \tau s \rangle / \langle \tau s \rangle_S$ (%)
(a) Deformed states	-11.9	-11.0
(b) cm (3p-2h)	-3.6	-0.9
(c) (a)-(b)	-8.3	-10.1

1.2 A new experimental method in β-NMR (NNQR)

For studies of core deformation and configuration mixing in the wave functions of this mass, $A = 41$ system, quadrupole moments are especially suitable clues, because those corrections to the moments are usually additive, as shown in the previous section. Therefore, it is easy to detect such large corrections, and to identify the origin of each contribution. In spite of such urgent needs, measurements of the quadrupole moment of ^{41}Sc have been very difficult, even by using the efficient β-NMR method. This has been due to the difficulties in obtaining well defined field gradients which ^{41}Sc nucleus interact with, and in maintaining the nuclear-spin polarization in a catcher (which provides an electric-field gradient to the ^{41}Sc) as long as its rather long nuclear half-life, $T_{1/2} = 0.596$s. Also, such detection of ^{41}Sc with a large nuclear spin, $I = 7/2$, are very difficult, since the β-NMR signals by use of a monochromatic rf are very small, *i.e.*, the quadrupole spectra detected by the β-NMR are very complicated. Finally, no simple and suitable field gradients for moderate quadrupole interactions (compared with the magnetic interaction) have been available in natural crystals that contain the stable Sc isotope, in the site where the implanted ^{41}Sc ions are going to be substituted.

1.2.1 Development of NNQR

Of course, the β-NMR technique, in which the asymmetric β-ray distribution from the spin-polarized (β-emitting) nuclei is monitored, has been effectively used for the magnetic-moment study of ^{41}Sc [4]; it can also be suitable for the present experimental purposes. Unfortunately, however, the available nuclear-spin polarization obtained through the nuclear reaction ^{40}Ca(d, n)^{41}Sc is small, about $P \sim 3\%$; even more, the production rate of the ^{41}Sc has been limited to less than 10^2s^{-1}, even with use of the present improved experimental system [4]. It is again pointed out that the detectable NMR effect is very small because the full NMR effect of $2AP \sim 6\%$ is distributed to all quadrupole lines of

$2 \times I = 7$. For this case, the observable β-NMR effect by using monochromatic rf for one rf transition is very small, about 1/84 of the full effect [4, 11, 13].

Therefore, it is impossible to measure a quadrupole spectrum by use of the conventional β-NMR. In order to solve these difficulties, the β-NMR technique has been modified; a newly developed quadrupole resonance technique (NNQR) has been developed for efficient and reliable measurements of the nuclear quadrupole coupling constant of β-emitting nuclei [14, 15]. In this method, β-NMR is detected as a function of the quadrupole coupling frequency, *i.e.*, a set of $2 \times I$ transition frequencies that correspond to a coupling frequency are simultaneously applied to the β-emitters for their spin manipulation. It is easy to see that this technique has been designed especially for short-lived nuclide with high spins and with relatively small nuclear-spin polarization.

1.2.2 Search for suitable field gradients

It is indispensable for the NNQR experiment to prepare a catcher that can: 1) keep the implanted nuclei (atoms) in a unique site of unit cell, 2) maintain the polarization produced through the reaction during the lifetime of the implanted nuclei, and 3) provide a proper electric-field gradient in it. It is the best to prepare a crystal in which a stable isotope of the implanted nuclei is included with high concentration. For example, for measuring $Q(^{17}\mathrm{F})$, a $\mathrm{MgF_2}$ crystal was available [13]. For the present case of Sc, however, no suitable natural crystal was available; Although a $\mathrm{Sc_2O_3}$ crystal is available, the field gradients at the Sc isotope are too much complex.

In general, it had been thought that polarization is difficult to maintain in insulator crystals in which no isotopes of implanted nuclei are included, because the relaxation time of the polarization is very much reduced due to radiation damage and the paramagnetic atomic states created by the recoil ions in the crystal and because the atomic configuration of the ion may be unstable. It was shown, however, in the systematic study that the implanted nuclei are very much isolated from such damage at low temperature. Furthermore, if the crystal contains isotopes close to the implanted nuclei, the implanted nuclei can play the role of the isotope practically. For example, when polarized ^{39}Ca nuclei were implanted into a KBr crystal, the polarization was maintained for as long as 4 sec [17]. The mechanism used to account for this phenomenon was that one of the unpaired electrons of ^{39}Ca is used for coupling with the adjacent Br atoms when a Ca with one other valence electrons is left far away. That is, the Ca atom does play the role of a K atom. Another good example is the implantation of ^{41}Sc in CaO crystal in which ^{41}Sc set in Ca substitutional site with diamagnetic surroundings. A narrow NMR line with T_1(^{41}Sc in CaO)$\sim$4 sec at room temperature was observed [4]. Based on an analogy involving the above-mentioned mechanism, it was expected that in the case of the implantation of Sc nuclei into a TiO_2, its polarization would be maintained as long as its lifetime. In fact, it was observed that the relaxation time was sufficiently long to perform a measurement of the quadrupole moment by the NNQR method, and that the TiO_2 crystal was useful for providing the proper electric-field gradient. At the Ti site field gradients vertical to c-axis, i.e., parallel to $\langle 110 \rangle$ or $\langle 1\bar{1}0 \rangle$ with the same amount are expected. Therefore, the Sc ions at Ti sites are energetically equivalent when a strong holding magnetic field is parallel to c-axis.

1.3 Contents of this paper

Two independent experiments were performed: a measurement of the electric quadrupole interaction of ^{41}Sc in a TiO_2 crystal, $|eqQ(^{41}\text{Sc in TiO}_2)|$, by the NNQR method, and a measurement of $|eqQ(^{45}\text{Sc in TiO}_2)|$ by the Fourier-Transformed pulse-NMR (FT-NMR) method. These experimental aspects and a theoretical one are described in the following chapter along with an explanation of indispensable equipment used in the present experiment. By taking the ratio of these coupling constants, $Q(^{41}\text{Sc})/Q(^{45}\text{Sc})$ was deduced, as given in chapter 3. $Q(^{45}\text{Sc})$ was determined by combining the known hyperfine coupling constant, B, with a calculation of the electric-field gradient at the nucleus of a free Sc atom; $Q(^{41}\text{Sc})$ was determined using the ratio relation. These are given in detail in chapter 4, and finally the quadrupole moments of A = 41 system and the ^{41}Ca core deformation are discussed.

Chapter 2

Experimental method and setup

2.1 Principle of the β-NMR method

The experimental method and apparatus used in the present measurements were essentially similar to the previous NMR detection system used in a magnetic-moment study of the β-emitting nucleus ^{41}Sc [4] and a quadrupole moment study of ^{17}F [13]. The major differences from that described in ref.[4] were first in the selection of the catcher for the implantation of the recoil ^{41}Sc nuclei produced through the ^{40}Ca(d, n)^{41}Sc reaction; instead of using a CaO crystal, a TiO_2 crystal was used in order to obtain a proper electric-field gradient. Other differences involved the employment of a modified β-NMR technique, a newly developed quadrupole resonance technique (NNQR), in which the nuclear polarization was manipulated by using multi-radio-frequency (RF) magnetic fields. All other experimental conditions were kept essentially the same as those used in the previous work [4] with the present experimental conditions listed in table 2.1; the experimental setup is shown in figure 2.1. The target, the collimator, the catcher and the RF coil were all placed in a vacuum chamber. The vacuum in the chamber was 10^{-7} Torr.

Table 2.1: Experimental conditions for the measurement of $Q(^{41}\mathrm{Sc})$

Production reaction	$^{40}\mathrm{Ca}(d,n)^{41}\mathrm{Sc}$
Incident beam	$E_d = 4.1\mathrm{MeV}$, $I_d \sim 10\mu\mathrm{A}$
Recoil angle	$20°\pm6.5°$
Target	Ca metal (150 mg/cm^2 thick)
Magnetic field	$H_0 = 0.6\mathrm{T}$
Catcher	TiO_2
β-decay mode	$^{41}\mathrm{Sc}(I^\pi = 7/2^-) \to {}^{41}\mathrm{Ca}(I^\pi = 7/2^-) + \beta^+$
Maximum energy of β^+	$E_{\beta^+} = 5.47$ MeV

The target and the catcher were in a strong magnetic field of 0.6 T. The β-rays from the ^{41}Sc in the recoil stopper were detected by two sets of counter telescopes; one of them comprised a 1 mm thick plastic counter as well as a 10 mm thick one. An RF coil having 30 turns and $30\phi \times 30$ mm produced an oscillating field, H_1, of 0.2mT perpendicular to the static magnet field in order to manipulate the nuclear spin.

The β-NMR method involved four process: (1) production of polarized nuclei, (2) preservation of the nuclear polarization, (3) manipulation of the nuclear spin, and (4) detection of any change in the distribution of β-rays due to manipulation of the spin. In the following sections, the experimental method of newly-developed nuclear quadrupole resonance (NNQR) is explained according to the principle of the β-NMR method.

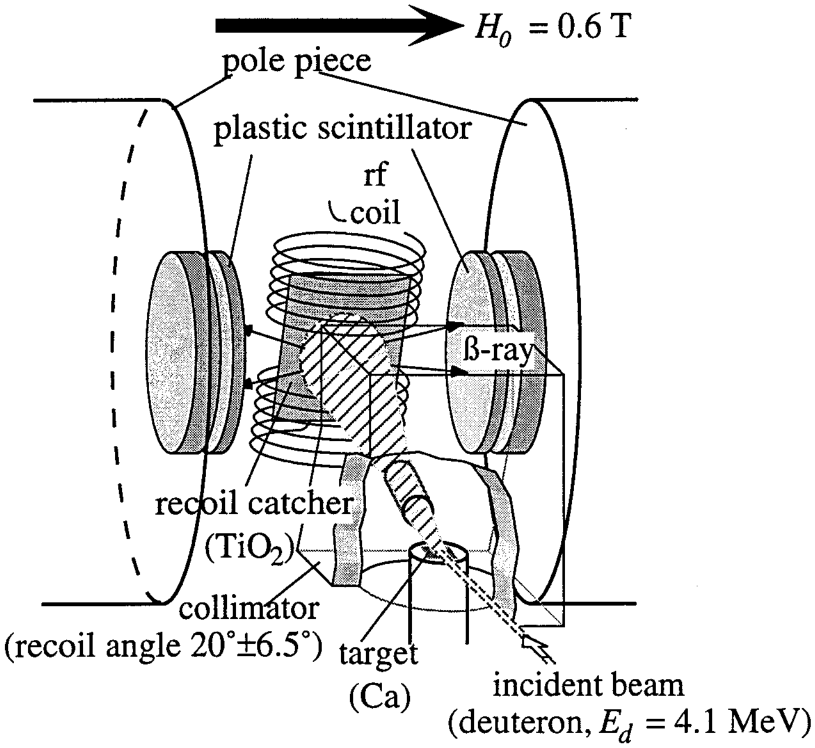

Figure 2.1: Schematic view of the experimental setup

2.2 Production of nuclear polarization

^{41}Sc nuclei were produced through the nuclear reaction ^{40}Ca(d, n)^{41}Sc whose Q-value is -1.14 MeV. The deuteron was accelerated to E_d = 4.1MeV using the 4.75 MeV Van de Graaff at Osaka University, and bombarded a metal Ca target (150 mg/cm^2 thick) evaporated on a copper backing. The ^{41}Sc nuclei ejected from the target to a recoil angle of 20°±6.5° were selected by a recoil collimator in order to obtain a nuclear polarization. As shown in figure 2.2, the maximum recoil energy at this recoil angle was 0.44 MeV. The

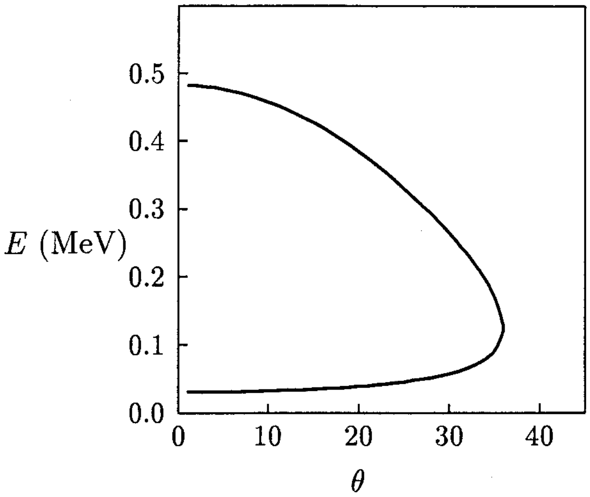

Figure 2.2: Reaction kinematics.
Kinematic energy, E (MeV), of ^{41}Sc nuclei produced through the reaction ^{40}Ca(d,n)^{41}Sc with E_d=4.1MeV was calculated as a function of the recoil angle, θ (degrees), in the laboratory system of coordinates.

^{41}Sc nuclei produced in this way were implanted into the TiO_2 catcher and distributed uniformly from the surface to 0.32 μm. By counting the β-rays from the ^{41}Sc nuclei, they were to be identified with the index of a lifetime of ^{41}Sc, $T_{1/2} = 0.596$ s. The typical time spectrum of β-rays from ^{41}Sc nuclei is shown in figure 2.3.

The direction of the nuclear polarization produced by this reaction is perpendicular to the reaction plane defined by the incident beam and the recoil beam axis. In general, the magnitude of the produced nuclear polarization depends on the condition of the nuclear reaction, *i.e.*, the beam energy and the selected recoil angle. In this experimental condition, we obtained a 3% nuclear spin polarization and about a 100/sec production rate.

2.3 Preservation of nuclear polarization

The polarized ^{41}Sc nuclei were implanted into the substitutional position of Ti in the TiO_2 crystal, as shown in figure 2.4. The nuclear polarization is depolarized: (1) in flight from the catcher to the stopper if the atomic states are not decoupled from the nuclei in the high magnetic field, and (2) in the stopper medium after a nucleus is stopped because of various nuclear spin-lattice relaxation mechanisms.

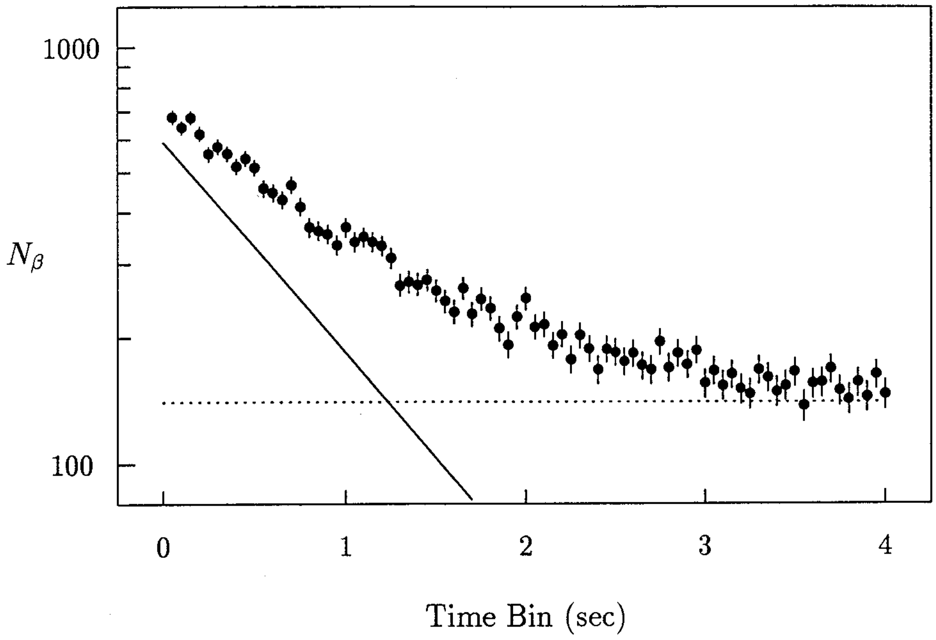

Figure 2.3: Typical time spectrum of β-rays from ^{41}Sc.
In this figure, the solid line is the component of ^{41}Sc ($T_{1/2}$ = 0.596s), and the dotted line is that of the long background.

2.3.1 Preservation of polarization in a high field

As for the recoil atom passing through free space, the system can be described as a free atom. The angular momentum $\boldsymbol{L}$ and spin $\boldsymbol{S}$ are combined to give the total angular momentum $\boldsymbol{J}$ of the extranuclear electrons. $\boldsymbol{J}$ and $\boldsymbol{I}$ are similarly combined to give a resultant, in order to obtain the total angular momentum $\boldsymbol{F}$ of the whole atom, including the nuclear spin $\boldsymbol{I}$. The nuclear spin with $\boldsymbol{I}$ precesses around the total spin, $\boldsymbol{F} = \boldsymbol{I} + \boldsymbol{J}$, combined with the atomic angular momentum $\boldsymbol{J}$, as shown in figure 2.5. Such a precession causes a decrease in the nuclear polarization, because the precession means that the average of the observable I_z is associated with that of F_z with a constant k, $\langle |I_z| \rangle = k \cdot \langle |F_z| \rangle$; in free space the direction of $\boldsymbol{F}$ is random, $\langle |F_z| \rangle = 0$, namely, $\langle |I_z| \rangle = 0$. In a strong magnetic field, the total angular momentum $\boldsymbol{F}$ precesses around it, with $\langle |F_z| \rangle \neq 0$; we thus have $\langle |I_z| \rangle \neq 0$. Therefore, the nuclear polarization can be preserved. In an actual experiment for the case of Sc, 0.6T was sufficient to preserve the nuclear polarization.

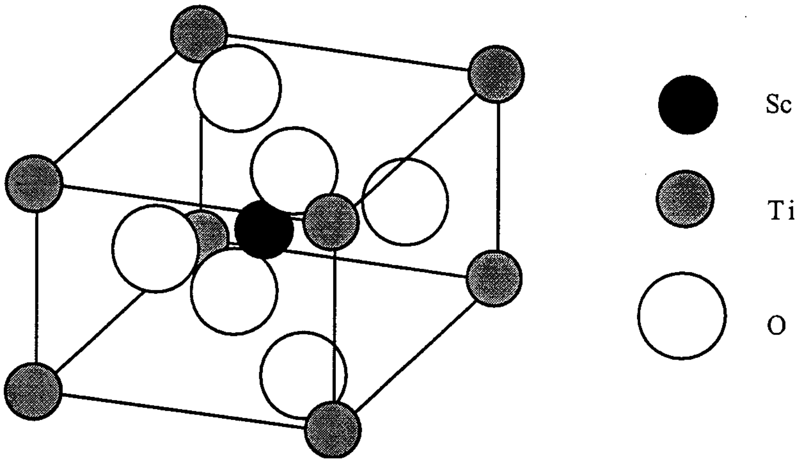

Figure 2.4: Crystal structure of TiO_2
The recoiled Sc atoms are expected to be located at the substitutional sites of Ti atoms in a TiO_2 crystal.

2.3.2 Location of implanted nuclei

The substitutional location of ^{41}Sc was supported in the present measurement, at least, for those that maintained nuclear polarization in the crystal during its nuclear lifetime of 0.596 s. This was because the Sc (III group) ion by borrowing a single electron from somewhere else can play an atomic role of the substituted atom Ti (IV group). It was empirically shown that the rate of such survival was about $\frac{2}{3}$ of the total Sc ions implanted in the crystal. Also observed was that such a survival rate for those ions substituted with ions having a group difference larger than 2 was less then $\frac{1}{10}$ of the total Sc ions. Such an example was well shown in the experiment on ^{41}Sc ions substituted for Ca atoms in CaO; about one half of the ^{41}Sc ions were at Ca sites with a long spin-lattice-relaxation time [4]. Also, a similar empirical rule was given in the experiments concerning ^{39}Ca in KBr and ^{8}Li in $LiIO_3$ crystals [17]. Regarding the relaxation times, for those ions located in the substitutional site of oxygen, or interstitial sites in the insulator crystal TiO_2, the spin-lattice-relaxation time is expected to be very short compared with the nuclear lifetime. Should the spin-relaxation time be long for the interstitial ions, or for the substitutional ion with odd electronic configurations, the interactions of the Sc nucleus with the surrounding hyperfine fields were paramagnetic and the transition frequencies were very much separated from the present NMR frequency. Therefore, if we followed such empirical rules, only the ^{41}Sc nuclei located in a substitutional site of Ti atoms in a TiO_2 crystal would be detected by the β-NMR technique or the modified β-NMR technique.

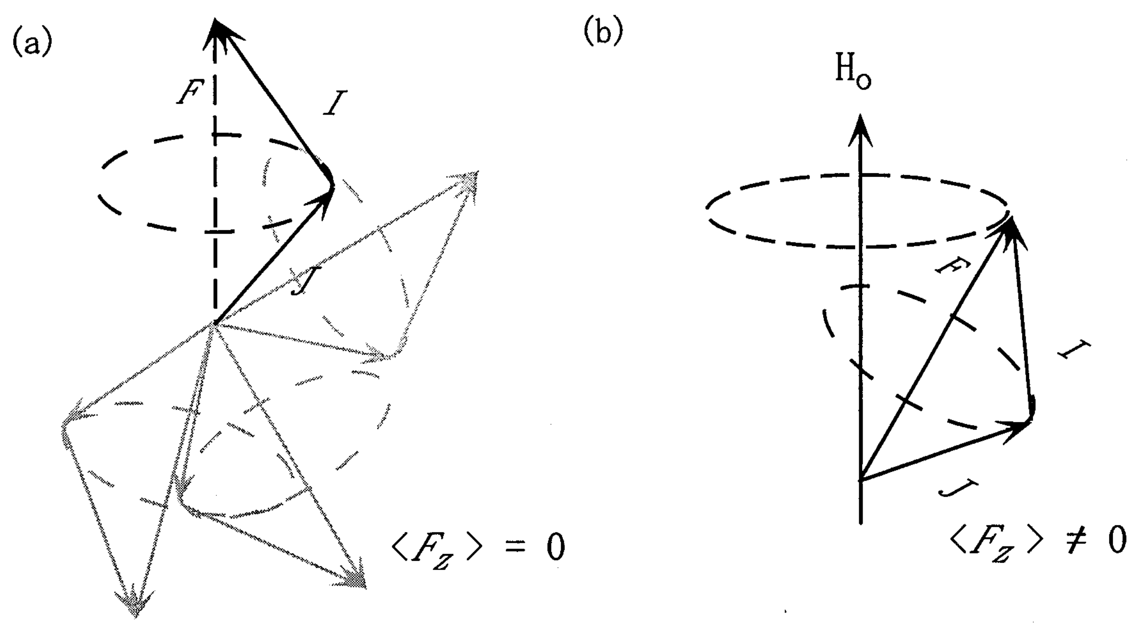

Figure 2.5: Precession of the total angular momentum in external fields
(a) The nuclear spin $\boldsymbol{I}$ precesses around the total angular momentum, $\boldsymbol{F} = \boldsymbol{I} + \boldsymbol{J}$. In the absence of a magnetic field, $\langle |I_z| \rangle = \langle |F_z| \rangle = 0$. (b) In a magnetic field, H_0, $\boldsymbol{F}$ precesses around H_0. This means that $\langle |F_z| \rangle \neq 0$ and the preservation of the nuclear polarization, $\langle |I_z| \rangle \neq 0$.

2.4 Detection of nuclear magnetic resonance

The β-NMR method utilizes the asymmetric β-ray distribution from the spin-polarized β-emitter. The angular distribution of the β-rays emitted from polarized ^{41}Sc nuclei as a function of the electron (positron) ejection angle, θ, defined relative to the polarization, P, is given as [Fig. 2.6]

$$W(\theta) = 1 + \frac{v}{c} A P \cos(\theta), \tag{2.1}$$

where A is the asymmetry factor, which is given by β-decay theory, v/c is the ratio of the β-ray velocity to the light velocity, and the polarization, P, is defined in terms of the magnetic substate, m, and its population, p_m, as

$$P = \frac{\sum_{m=-I}^{I} m p_m}{I \sum_{m=-I}^{I} p_m}. \tag{2.2}$$

Since we manipulate the spin polarization by RF magnetic fields in the β-NMR technique, the present method involves the detection of any change in the degree of the asymmetric β-ray distribution.

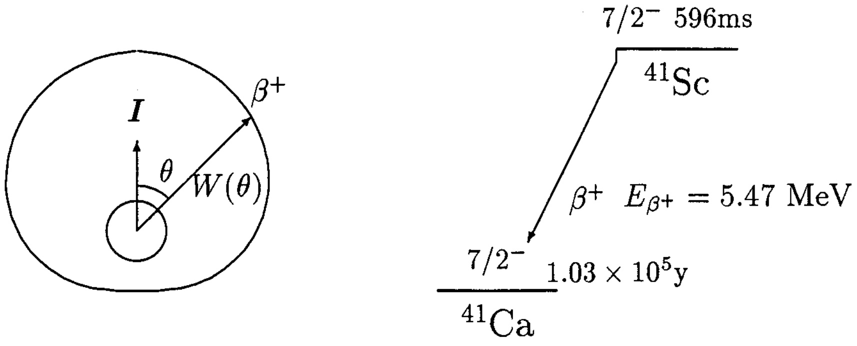

Figure 2.6: Angular distribution of the β-rays emitted from polarized nuclei
Angular distribution of the β-rays emitted from the polarized nuclei $W(\theta) = 1 + \frac{v}{c}AP\cos(\theta)$ was shown.

In order to determine the β-decay asymmetry, the β-rays from ^{41}Sc implanted in a recoil catcher were detected using the two sets of plastic-scintillator-counter telescopes placed above and below the catcher relative to the polarization. The β-rays were detected only during beam-off counting times, typically a duration of 1.4s, following a beam-on production time of 0.8s. The RF for the NMR was applied for 100 ms in between the production time and the following counting time. The up-down counting-rate of the time section for which the polarization was manipulated by the RF(RF-on) was normalized by the other ratio for the section without any manipulation (RF-off) as

$$\Delta = \frac{\{\frac{W(0)}{W(\pi)}\}_{on}}{\{\frac{W(0)}{W(\pi)}\}_{off}} - 1, \sim 2A(P_{on} - P_{off}) \tag{2.3}$$

where P_i is the time average of the time-dependent polarization due to the finite spin-lattice-relaxation time.

2.5 Manipulation of nuclear spin by use of RF

2.5.1 New Nuclear Quadrupole Resonance Technique (NNQR)

The characteristic of the NNQR method is in the way to manipulate the nuclear spin with RF's, whose frequencies are represented by the quadrupole coupling frequency, ν_Q. Basically, the way used in the present experiment to manipulate the nuclear spin was the depolarization method, that is, equalization of the populations of the adjacent magnetic substates. When the preset ν_Q, which determines the RF frequencies, f_i, are in agreement with the true ν_Q, all populations of the magnetic substates are equalized, and the observed change in the nuclear polarization is maximum. Compared with the single RF, which equalizes only two adjacent substates, the NNQR method is very efficient; for ^{41}Sc($I^\pi = 7/2^-$), the NNQR is able to gain an 84-times change in the polarization. As explained in the following, the NNQR method is a modified β-NMR method which effectively extracts from the β-NMR effect by the RF's whose frequencies are associated by a parameter, ν_Q. To understand the NNQR method, we firstly need the knowledge concerning the electric-quadrupole interaction which causes the splitting of the resonance frequency.

2.5.2 Electric quadrupole interaction in a high field

Polarized ^{41}Sc nuclei were implanted into a TiO$_2$ crystal placed in a strong magnetic field, H_0, of 0.6 T. There are two directions of the field gradient, q, in the substitutional site of Ti ions of TiO$_2$ crystal having a rutile structure (tetragonal). One is parallel to the <110> axis; the other is parallel to the <1$\bar{1}$0> axis. In the present experiment a TiO$_2$ single crystal was placed so that each angle between a q and the magnetic field was 90.0 degrees, in order to make the resonance spectrum simple. The resonance frequency was split into the $2 \times I = 7$ frequencies due to the electric-quadrupole interaction of ^{41}Sc nuclei with the field gradient at the nucleus, as follows.

In an electromagnetic field, the Hamiltonian of the nucleus with spin I is given as [16]

$$\mathcal{H} = \mathcal{H}_M + \mathcal{H}_Q. \tag{2.4}$$

$\mathcal{H}_M$ is the magnetic interaction of the magnetic moment, μ, with a magnetic field $\mathbf{H} = (H_x, H_y, H_z) = (0, 0, H_0)$ in the xyz-coordinate system, and can be written as

$$\begin{aligned} \mathcal{H}_M &= -\mu\mathbf{H} \\ &= -g\mu_N I_z H_0 \\ &= -h\nu_L I_z, \end{aligned} \tag{2.5}$$

where ν_L is the Larmor frequency and g the g-factor of the nuclei. $\mathcal{H}_Q$ is represented as

$$\mathcal{H}_Q = \frac{h}{6}\nu_Q\{3I_Z^2 - I(I+1) + \frac{1}{2}\eta(I_+^2 + I_-^2)\} \tag{2.6}$$

with $I_\pm = I_X \pm iI_Y$ in the XYZ-coordinate. The quadrupole coupling frequency, ν_Q, is associated with the constant of the quadrupole interaction, eqQ, as

$$\nu_Q = \frac{3eqQ}{2I(2I-1)h}. \tag{2.7}$$

In equation 2.6 the X, Y, Z axis are also the principal axes of the tensor V_{ij}, which describe the electric-field gradient, q, with

$$q = V_{ZZ} \tag{2.8}$$

and

$$\eta = \frac{V_{XX} - V_{YY}}{q}, \text{ with } |V_{ZZ}| \geq |V_{YY}| \geq |V_{XX}|. \tag{2.9}$$

The xyz-coordinates are associated with the XYZ-coordinates by a rotation of $R(\theta, \varphi, 0)$, which is characterized by Euler angles θ and φ, as shown in figure 2.7. By using these Euler angles, equation 2.4 can be represented in the xyz-coordinates:

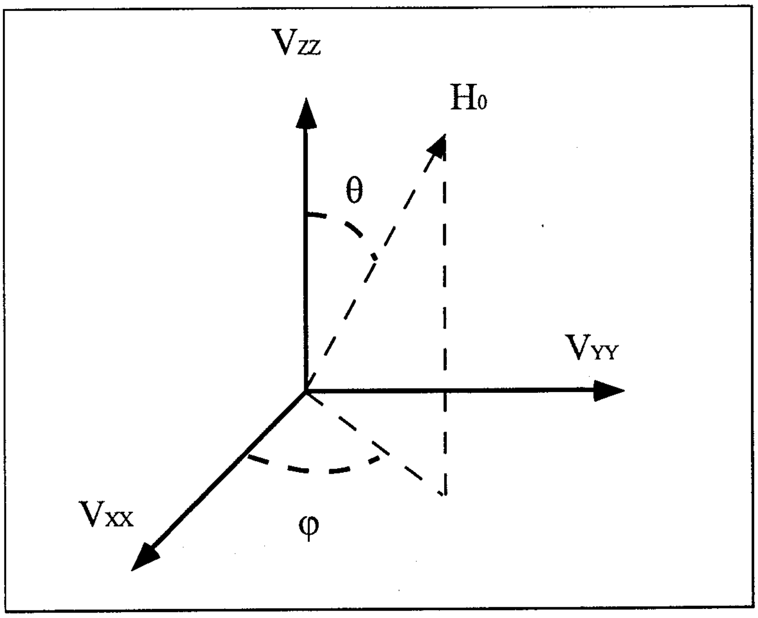

Figure 2.7: Orientation of the field gradient relative to the external magnetic field applied parallel to the z-axis

$$\begin{aligned}
\mathcal{H} = & -h\nu_L I_z \\
& + \frac{h\nu_Q}{6}\left[\frac{1}{2}(3\cos^2\theta - 1 + \eta\sin^2\theta\cos 2\varphi)\left\{3I_z^2 - I(I+1)\right\}\right. \\
& + \left\{\frac{3}{2}\sin\theta\cos\theta - \frac{\eta}{4}(\sin 2\theta\cos 2\varphi - 2i\sin\theta\sin 2\varphi)\right\}(I_z I_+ + I_+ I_z) \\
& + \left\{\frac{3}{2}\sin\theta\cos\theta - \frac{\eta}{4}(\sin 2\theta\cos 2\varphi + 2i\sin\theta\sin 2\varphi)\right\}(I_z I_- + I_- I_z) \\
& + \left\{\frac{3}{4}\sin^2\theta + \frac{1}{4}(1 + \cos^2\theta)\cos 2\varphi\right\}(I_+^2 + I_-^2) \\
& \left. - i\frac{\eta}{2}\cos\theta\sin 2\varphi(I_+^2 - I_-^2)\right]
\end{aligned} \tag{2.10}$$

The energy, E_m, of a magnetic state, m, is given by solving the eigenvalue problem,

$$\mathcal{H}|\Psi_m\rangle = E_m|\Psi_m\rangle. \tag{2.11}$$

In a high magnetic-field limit, the energy is given to first order by perturbation theory,

$$E_m = -h\nu_L m + \frac{\nu_Q}{4}(3\cos^2\theta - 1 + \eta\sin^2\theta\cos 2\varphi)\left\{3m^2 - I(I+1)\right\}. \tag{2.12}$$

The transition frequencies among magnetic substates m and $m-1$ are defined as

$$\nu_m = |E_m - E_{m-1}|. \tag{2.13}$$

Due to the quadrupole interaction, $2 \times I$ transition frequencies separate from the Larmor frequency, ν_L, as shown in figure 2.8. In general, the E_m's are eigenvalues of equation 2.11, and are calculated by diagonalizing the Hamiltonian (2.4).

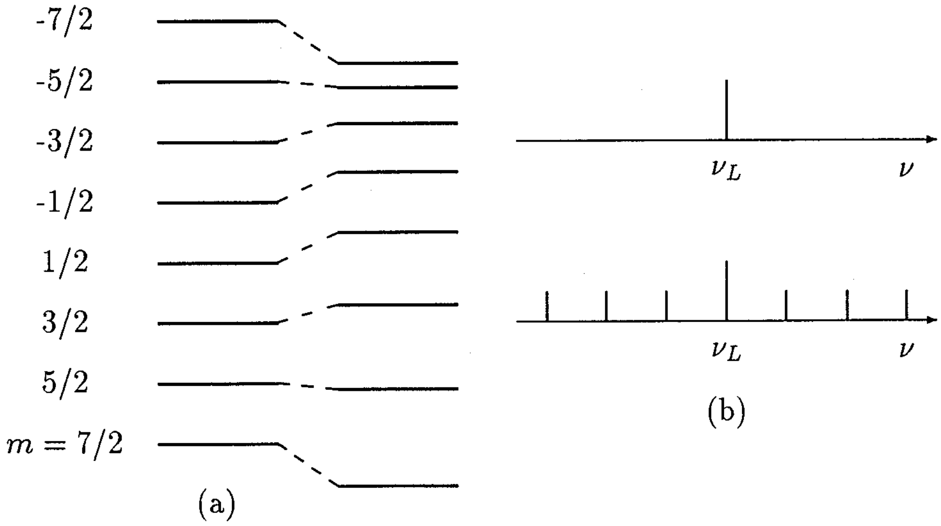

Figure 2.8: Energy levels of the magnetic substates and transition frequencies of $I = 7/2$ system in a high field
(a) The energy levels of the magnetic substates of the nuclei with $I = 7/2$ are shown. The energy levels at regular intervals shift due to the quadrupole interaction keeping the center of gravitation. (b) The transitions frequencies are separated from the Larmor frequency ν_L to the $2 \times I$ frequencies due to the quadrupole interaction.

In the present experiment the Larmor frequency of ^{41}Sc in the TiO$_2$ crystal was calculated using the resonance frequency of ^{41}Sc implanted in an ionic CaO (cubic) crystal [4] and knowledge concerning the chemical shifts. Also, the Larmor frequency without any correction of the chemical shift, $\nu_L = 7072.8$ kHz, was determined by detecting the $1/2 \leftrightarrow -1/2$ transition using the 3-RF's technique used in the previous β-NMR study [13, 17], and by calculating the second-order shift using the preliminary value of ν_Q. The difference in the chemical shift in CaO from that is about a few kHz. The asymmetry factor of the field gradient of TiO_2, $\eta = 0.58$, was determined by the FT-NMR of ^{45}Sc in the TiO_2 crystal. With these values of the Larmor frequency and so on we calculated the transition frequencies as a function of the quadrupole coupling constant based on the above-mentioned formalism.

Figure 2.9 shows the transition frequencies and RF frequencies represented by ν_Q with modulations in the present experiment. The widths of the frequency modulation

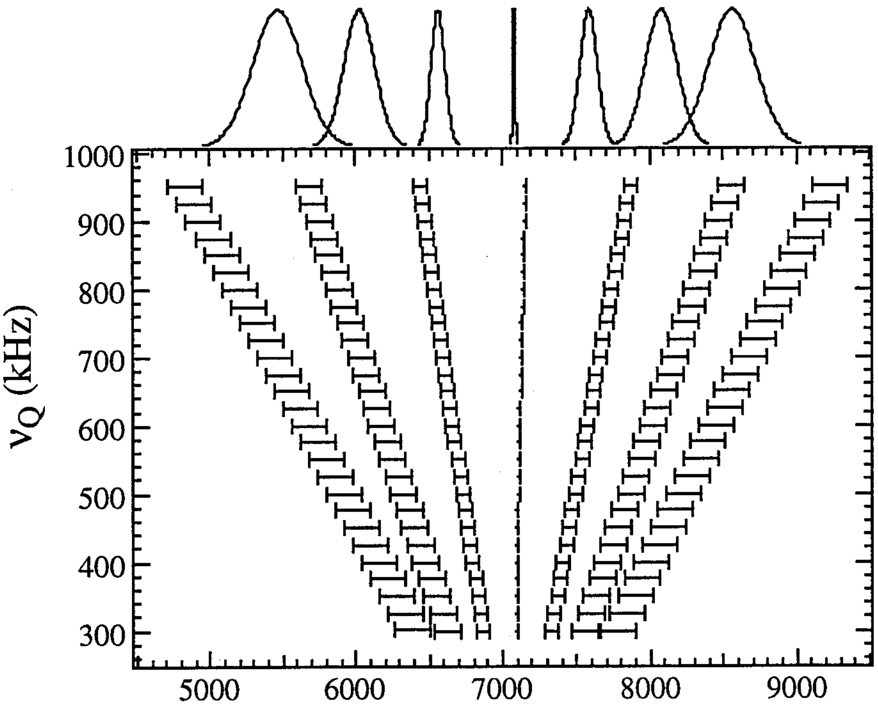

Figure 2.9: Transition frequencies and RF frequencies
The transition frequencies of ^{41}Sc in TiO_2 crystal are shown with the applied RF's corresponding to the assumed ν_Q.

were about $\Delta f = \pm 140$ kHz for $\pm 7/2 \leftrightarrow \pm 5/2$ transitions, ± 90 kHz for $\pm 5/2 \leftrightarrow \pm 3/2$ transitions, ± 50 kHz for $\pm 3/2 \leftrightarrow \pm 1/2$ transitions, and ± 12 kHz for $\pm 1/2 \leftrightarrow \mp 1/2$ transitions.

2.6 Theoretical NNQR spectrum

Simply, an NNQR spectrum can be defined as a function of the coupling frequency of the electric quadrupole interaction, ν_Q,

$$F = F(\nu_Q). \tag{2.14}$$

F is the shape function of the NNQR spectrum, representing any change in the nuclear polarization due to spin manipulation. Here, the ν_Q parameter indicates $2 \times I$ frequencies f_i $(i = 1, 2, \ldots, 2I)$ determined by solving the eigenvalue problem using equation 2.11. In other words, F is the change in the nuclear polarization upon applying an RF consisting of $2 \times I$ frequencies. $F(\nu_Q)$ is therefore expected to have a peak when the ν_Q parameter is the true ν_Q, which means that all of the resonance frequencies are in agreement with the applied RF frequencies.

More generally, the NNQR spectrum is a function of the following parameters:

- ν_Q, coupling frequency of the electric quadrupole interaction.
- ν_L, Larmor frequency.
- I, nuclear spin.
- Δf_i, modulation of RF's.
- Δq, distribution of an electric field gradient.
- δH, local field giving rise to a dipolar broadening of the spectrum.
- p_m, population of a magnetic substate of the nuclei.

For simplicity, we make some assumptions. First, the magnetic substates of a nucleus with spin I are assumed to be populated linearly, $p_m = am + b$. This assumption means that the nucleus has no nuclear alignment, which is rather realistic in the case that the nuclei are produced through such a reaction as ^{40}Ca(d,n)^{41}Sc. By using the normalization of populations,

$$\sum_{m=-I}^{I} p_m = 1, \tag{2.15}$$

and the definition of polarization,

$$P \equiv \frac{1}{I} \sum_{m=-I}^{I} m p_m, \tag{2.16}$$

the population can be written as

$$p_m = \frac{3P}{(I+1)(2I+1)}m + \frac{1}{2I+1}. \tag{2.17}$$

Secondly, the quadrupole coupling constant is so small that the second-order shift of resonance frequencies can be neglected. This leads to the following relation between the frequency of the RF's and ν_Q:

$$f_i = \alpha_i \nu_Q. \tag{2.18}$$

Figure 2.10 shows the NNQR spectra for $I = 1/2, 1, 3/2, 7/2$ calculated under the above-mentioned assumptions. It is clear that the change in the nuclear polarization is maximum when the RF's correspond to the true coupling frequency, ${\nu_Q}^0$. As the nuclear spin, I, is greater, the NNQR spectrum has more sub peaks. Those peaks are very small compared to the main peak due to the partial depolarization. The spread in the resonance curve is due to dipolar broadening and the spread in the field gradient. In the case that ν_Q is comparable with ν_L, a spread in the field gradient causes dominantly the spread in the resonance curves. NNQR line-shapes as a function of $\Delta q/q$ are given in figure 2.11.

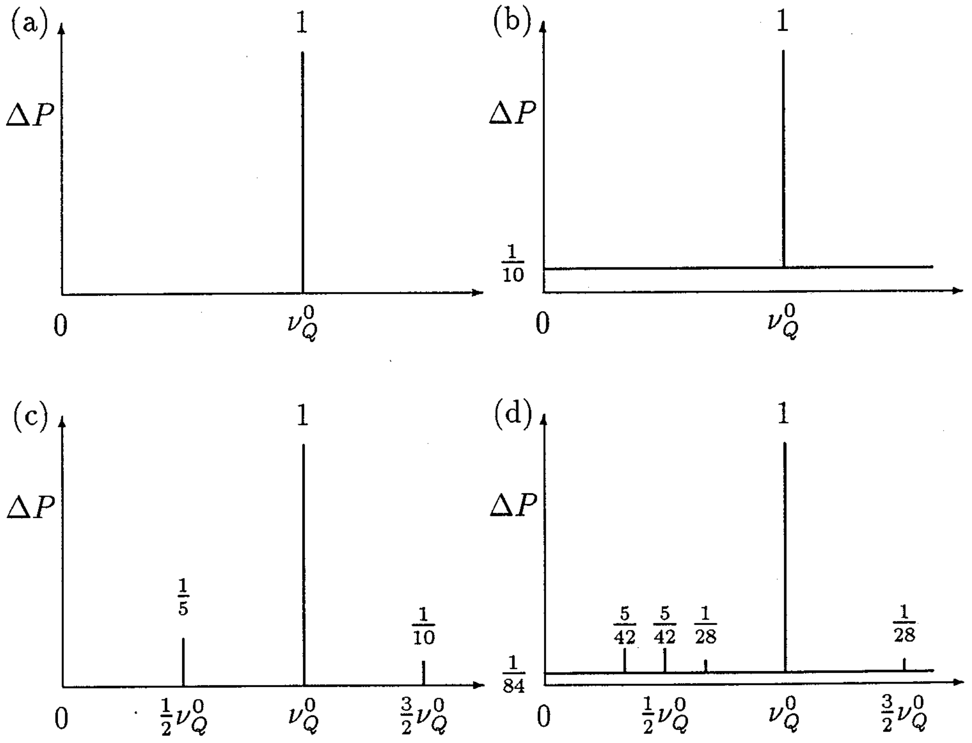

Figure 2.10: Theoretical NNQR spectrum
Ideal NNQR spectra were shown for (a) I=1, (b) I=3/2, (c) I=2, (d) I=7/2.

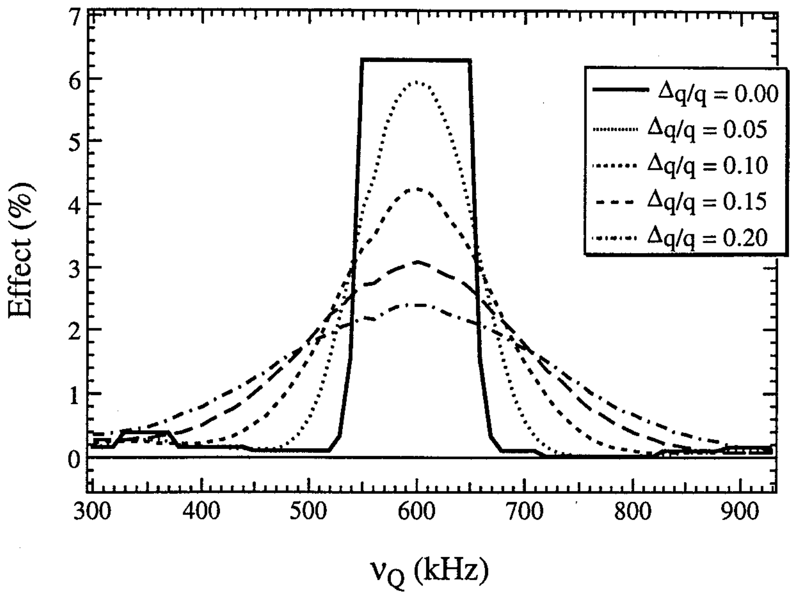

Figure 2.11: Calculated NNQR effects as a function of the coupling frequency. The widths of the RF modulations are proportional to $|\nu - \nu_L|$. Only the single quantum transitions are considered. NNQR line-shapes are shown as a function of $\Delta q/q$.

It can be said that the NNQR method can be used to extract the quadrupole coupling frequency from the β-NMR spectra. In fact, even if the assumed ν_L is slightly different from the true ν_L, the NNQR spectrum has a peak value at the true ν_Q, as shown in figure 2.12.

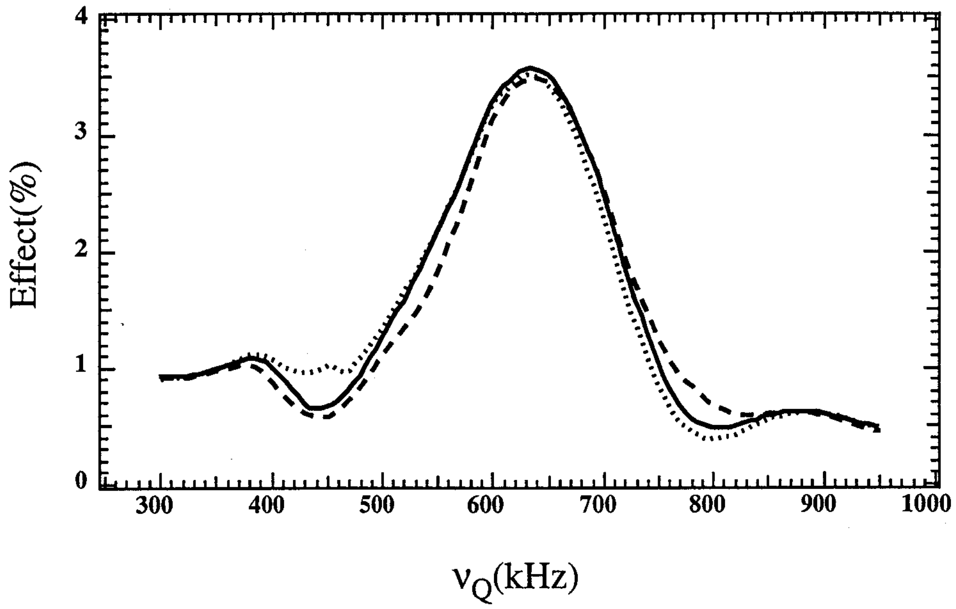

Figure 2.12: Change in the NNQR spectrum due to the Larmor frequency
Calculated NNQR spectra in the case that the assumed Larmor frequency is different from the true one. The dashed line is a spectrum with $|\nu'_L - \nu_L|/\nu_Q = -0.44\%$ and the dotted line with $|\nu'_L - \nu_L|/\nu_Q = +0.44\%$.

2.7 Time-sequence program for NNQR

The time-sequence program is shown in figure 2.13 for the NNQR detection of ^{41}Sc. In the 800 ms beam-on time, through the ^{41}Ca(d, n)^{41}Sc reaction with an incident deuteron energy of 4.1 MeV, the ^{41}Sc nuclei ejected at a recoil angle, θ, of 20° were implanted in a TiO$_2$ crystal. The spin polarization maintained in the TiO$_2$ crystal was about 3%.

Following the beam-on ^{41}Sc-production time, there was a 100 ms RF time, which comprised the 14 × 7 RF's. All 7 RF's corresponding to a presumed coupling frequency, ν_Q, were successively applied within 7.15 ms; the time duration for one RF was 1 ms, while for each switching of the RF it took about 20 μs. A set of 7 RF's were repetitively applied 14 times during the RF time.

After the RF time, a β-ray counting time of 2.4 s followed. The average β-ray counting rate was about 100 counts/sec.

Typically, 27 presumed coupling frequencies were mapped in a NNQR spectrum measurement; a coupling frequency was switched to the next one at the end of each beam-count cycle by a controlling computer. The set of 27 coupling frequencies were repeated until necessary counting statistics were obtained.

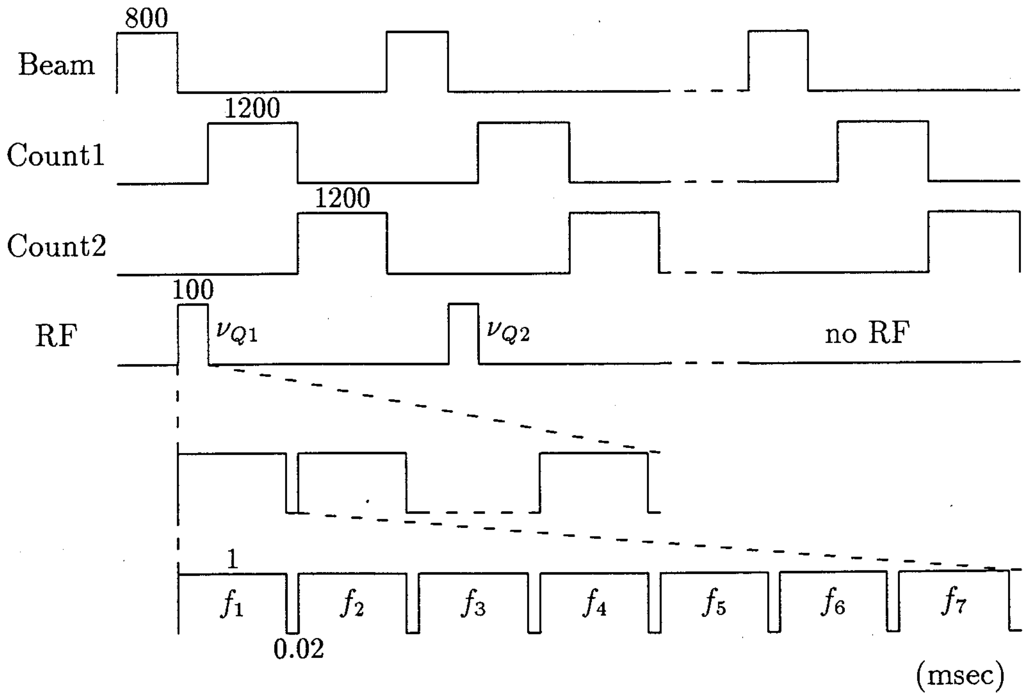

Figure 2.13: Time-sequence program of the NNQR detection of ^{41}Sc in TiO$_2$

In addition, normalization cycles were added. In order to reject any long-term time-dependent fluctuations in the up-down counting ratio due to fluctuations of the beam position on the target and of the beam intensity, a beam-count cycle without spin manipulation (RF off) was inserted in between two successive beam-count cycles for two coupling frequencies. Therefore, extra 27 beam-count cycles were added, for which RF was not applied (Off RF) for normalization.

2.8 Experimental equipment

2.8.1 RF system

The RF system comprised a controller and a resonator. The RF controller system used in the present experiment was designed so as to meet the requirement of the NNQR technique. As shown in diagram 2.14, this system mainly comprised a CPU, NIM modules, four ramp generators, and a function generator. As a CPU, a PC-9801VX (NEC; INTEL 80286) was used; its bus of it was harnessed so as to connect a PPI (parallel port interface), a GPIB interface and a DAC (digital to analog converter). The PPI had 8 inputs and 40 outputs at the TTL level that generate gate signals to select one RG (ramp generator) and to inhibit the output of any unnecessary frequencies produced during changing the RF frequency. The VCF (voltage converter to frequency) function of the FG (function generator) was utilized to control the RF frequency. The level of an input signal to the VCF was proportional to the output frequency within 0.1% precision.

The VCF input signal was generated with a DAC and RG's. The DAC provided a voltage level corresponding to the frequency $f_i + \Delta f_i$ ($i = 1, 2, ..., 7$). The DAC used in this experiment was a 12-bit DAC; one bit corresponded to 1kHz. An RG is a device which generates a ramp signal during a gating time; each four RGs produces a different amplitude. Each ramp generator gave a ramp of the voltage from the 0 to $-2\Delta V_i$, the span of which corresponded to $2\Delta f_i$ in frequency. The phase of the ramp signals was random, or not synchronized, for a complete depolarization of the nuclear spin. Figure 2.15 shows the transition frequencies for $I = 7/2$, and a set of RF frequencies given for the assumed coupling frequency, ν_Q.

In order to realize the NNQR method, the RF resonator system was required to have a wide-range frequency characteristic of the RF output. The range of the RF frequencies used in this experiment was 5 $\sim$ 9 MHz, ±30% of the Larmor frequency, ν_L. Therefore,

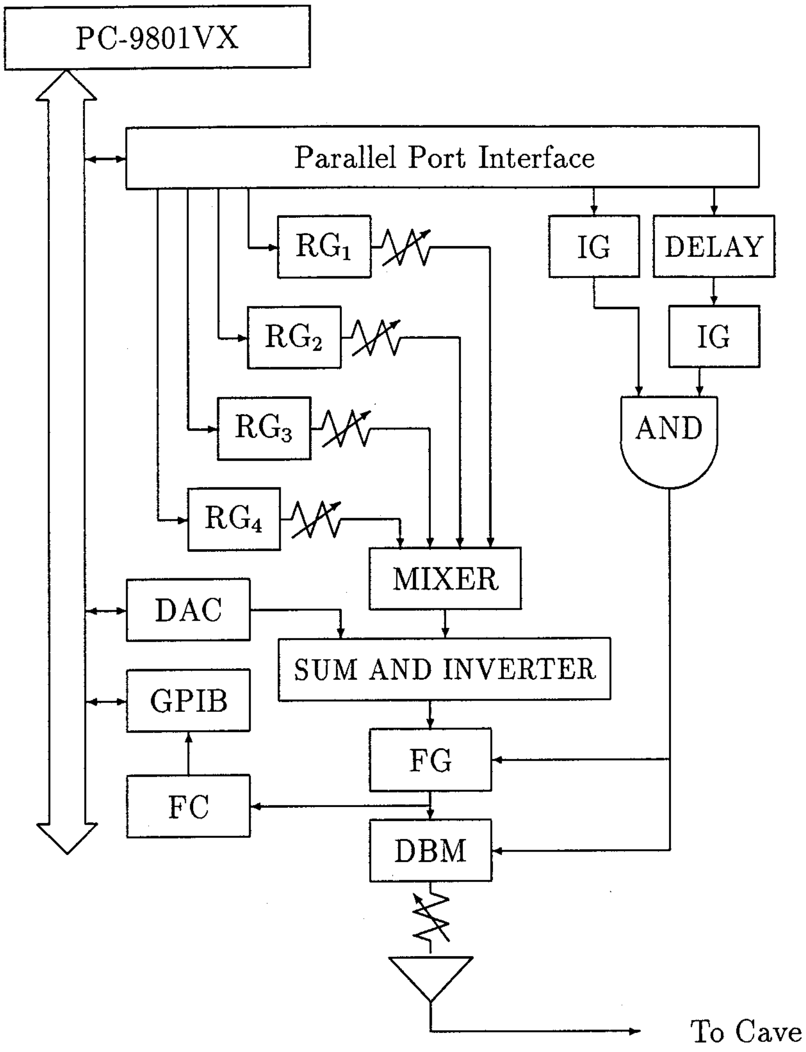

RG	Ramp Generator
IG	Interval Generator
FG	Function Generator
DBM	Double Balanced Mixer
FC	Frequency Counter

Figure 2.14: RF control system

the resonance frequency, represented by

$$f = \frac{1}{2\pi\sqrt{LC}}, \tag{2.19}$$

was set to a high frequency, f, of 10.6 MHz. The capacitance, C, was 15 pF and the inductance, L, was 15 μH, as shown in figure 2.16. A 100 Ω resistor, R, played the role of making the Q-curve of the resonator become dull. Being different from the usual usage of a resonance system, the RF system used in this experiment was a so-called off-resonance system. By using this system, an RF strength greater than the 2 mT was able to gain

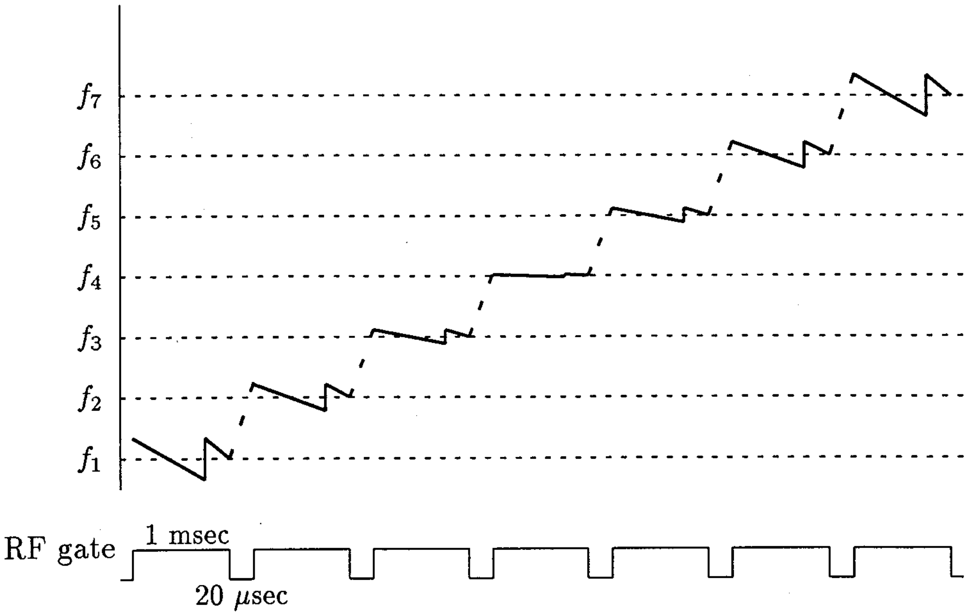

Figure 2.15: RF frequencies
Transition frequencies f_i ($i = 1, 2, \ldots, 7$) for $I = 7/2$, and a set of RF frequencies given for a preset coupling frequency, ν_Q.

over the necessary range of the RF frequencies.

2.8.2 Data-acquisition system

In the same way as the RF control system, the data-acquisition system used in the present experiment comprised a CPU, NIM modules, and three counter boards connected to the bus of the CPU (figure 2.17). The gate signal through PPI was used in order to prevent the discrimination level from being unstable, due to high rate counts during the beam time. Also, PPI was used for controlling the beam chopper and the current integrator was used to monitor the beam current on the target.

The program running on the CPU to control this system in the way explained in the above section was written using the BASIC and Assembler language. BASIC was mainly used for the interactive process, which provided a user interface, and for analyzing the data and displaying the results. Assembler was used to control the RF system and data-acquisition system, which required the speed. The main routine of data acquisition is explained in appendix C.

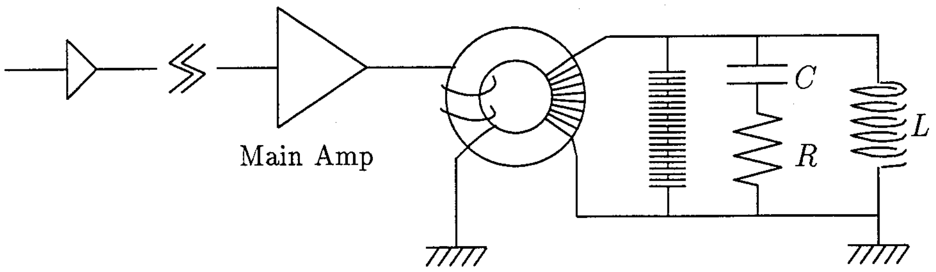

Figure 2.16: RF-resonator system

The RF resonator system used in the present experiment is shown. The condition of the parameters, $C = 15\text{pF}$, $R = 100\Omega$, $L = 15\mu\text{H}$, were determined so as to obtain the wide-range characteristics required in the NNQR method.

2.8.3 Target

Metallic Ca was best as a Ca target used for the production of ^{41}Sc nuclei in the present experiment. This is because a Ca compound target has the following difficulties: (a) the extra element causes possible background nuclide and (b) the lower concentration of Ca results in a smaller yield. Metallic Ca is, however, rapidly damaged in natural air, *i.e.*, it is oxidized or hydroxidized. We thus developed a reliable procedure for treating a metallic Ca target. The essential point was to keep the metallic Ca from the natural air in the following way.

The metallic Ca surface was coated with silicone oil immediately after evaporation of Ca on a Cu backing. The coating was removed in the vacuum of the reaction chamber before use. The target was always handled in a simple dry bag containing dry nitrogen. It was then stored in a small desiccator with phosphorus pentaoxide (P_4O_{10}) used as a desiccant. A schematic view of the apparatus is shown in figure 2.18; the detailed procedure to make metallic Ca targets was as follows.

1. Vacuum evaporation of metallic Ca. Granular Ca metal was evaporated for 20 min in a tantalum boat at 800°C. The thermal shield plate shown in the figure kept the coating oil in the other boat from being heated up and evaporating. In addition, a shutter covered the oil boat during the evaporation of Ca, because contamination of the oil causes a suspension to form on the backing instead of the metallic target.

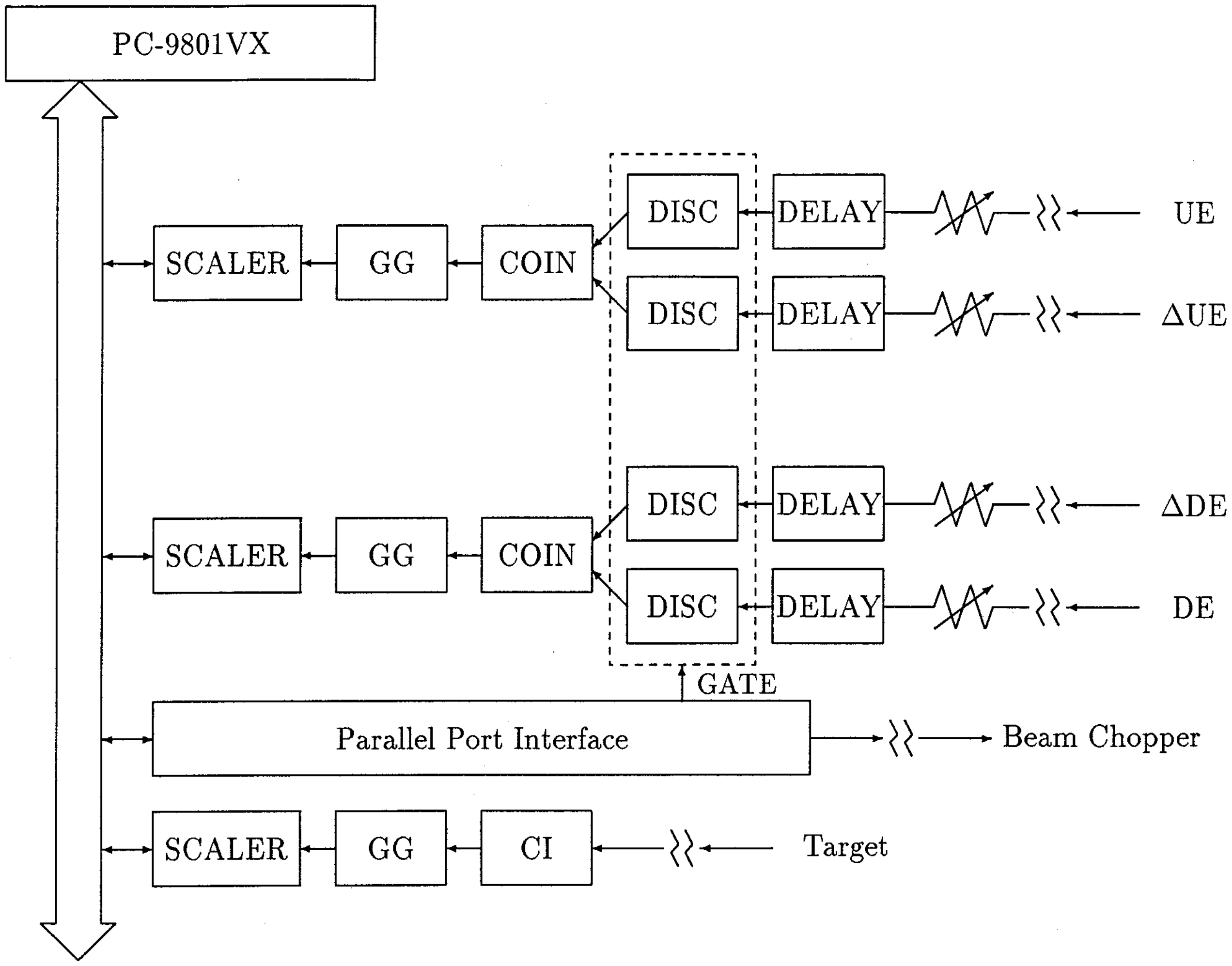

GG	Gate Generator
COIN	Coincidence
CI	Charge Integrator
ΔUE, UE	counter telescope of up
ΔDE, DE	counter telescope of down

Figure 2.17: Data acquisition system

The target thickness was evaluated based on the evaporated weight, assuming that the amount was deposited uniformly onto the upper hemisphere.

2. Coating the surface of the Ca target with the oil. The coating oil was put in the boat previously and the amount of oil was such that the whole evaporation resulted in a coating thickness of about 100 μg/cm^2. After a short preheating time, the shutter was opened and the oil was heated moderately until it completely evaporated. The coating oil was silicone diffusion oil (DC705, Dow Corning), which was carbon free

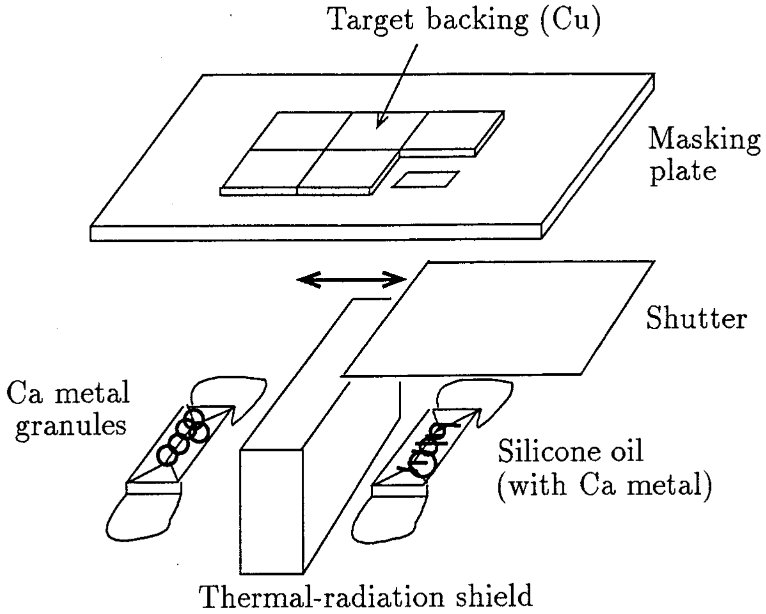

Figure 2.18: Schematic view of vacuum evaporation in preparing a metallic Ca targets.

and hardly decomposed upon heating. The oil had been kept in a tight vessel with many pieces of metallic Ca in it in order to inactivate the oil. These metal pieces had consumed all contaminants that would react with Ca. The deactivation was confirmed by putting the Ca in the oil on the boat.

3. Storing the targets. After evaporation and the coating, the apparatus was left to cool to room temperature. A desiccator was placed in a bag made of polyethylene film attached to the vacuum evaporation apparatus shown in figure 2.19. After a few cycles of flushing, the dry bag with nitrogen gas, the bell jar was leaked with dry nitrogen and opened. The targets were then transferred and stored in a desiccator with phosphorus pentoxide.

4. Setting the target in the reaction chamber. The targets were transferred from the desiccator into the chamber through a dry bag, similar to that explained above.

5. Removing the coating oil. The coating oil was removed in a good vacuum by baking at 60 W for 1 hour. The target was heated up by a ribbon heater that was wound around the copper pipes of the target cooling system. After leaving and cooling to room temperature, the metallic Ca target was ready to use.

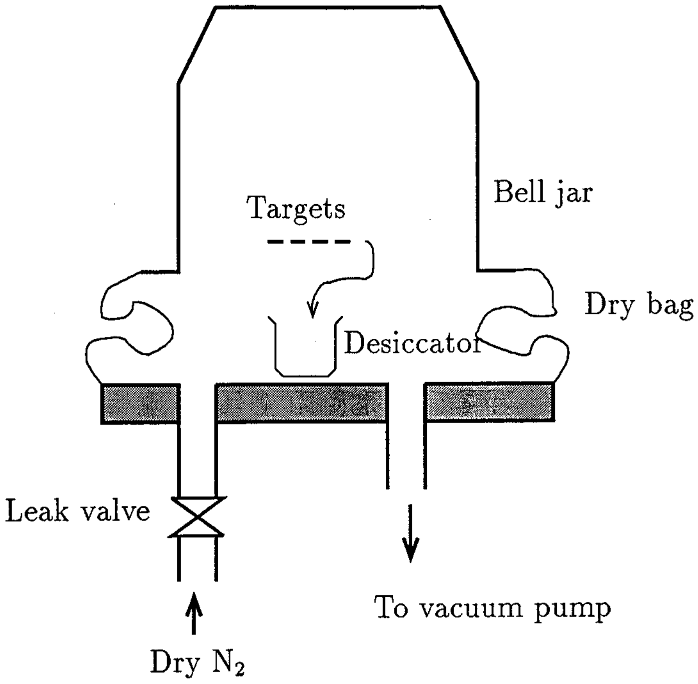

Figure 2.19: Dry bag used to keep the target from natural air.

2.8.4 Catcher

The catcher used in the present experiment was a TiO_2 crystal. The crystal was 20 mm long, 15 mm wide and 300 μm thick, as shown in figure 2.20. It was sliced so that c-axis of the TiO_2 crystal was parallel to the longer side. The crystal was processed so as to make its surface as smooth as glass by polishing with the silicon dioxide. Because the recoil ^{41}Sc nuclei were implanted and distributed in the TiO_2 crystal uniformly from the surface to 0.32 μm, the surface of the crystal was required to have no strain which might

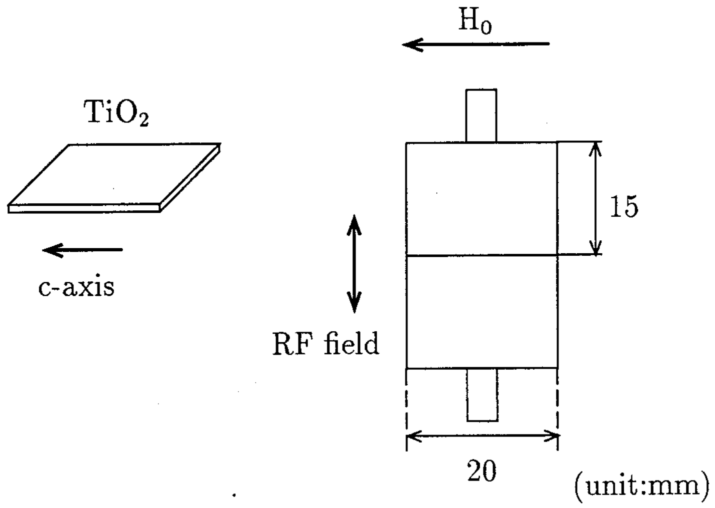

Figure 2.20: Catcher used in the present experiment

cause a broadening of the electric-field gradients.

The catcher comprised the two TiO_2 crystals on a catcher holder made of oxygen-free copper. The catcher was set up in a static magnetic field, H_0, so that the c-axis of the TiO_2 crystal was parallel to H_0 and perpendicular to the RF field, *i.e.*, both electric field gradients were perpendicular to H_0.

2.9 Electric-field gradient detected by ^{45}Sc substituted at a Ti site in TiO_2 and its measurement by detecting FT-NMR of the ^{45}Sc

The strength of the field gradient as well as its orientation was measured using the FT-NMR (pulsed Fourier-transformed NMR) detection of $^{45}Sc(I^{\pi} = 7/2^{-})$ implanted in a TiO_2 crystal at $H_0 = 4.7$ T and at room temperature. The concentration of the ^{45}Sc atoms in the crystal was dilute, 0.5% (atomic per cent relative to the Ti atoms in the crystal) [Appendix C]. In the detection, second-order quadrupole shifts were detected at the resonance frequency between the magnetic substates, $m = 1/2$ and $-1/2$. The typical FT-NMR spectrum is shown in figure 2.21. The resonances were measured as a function of the rotating angle of the crystal around a fixed axis, that was placed perpendicular to the

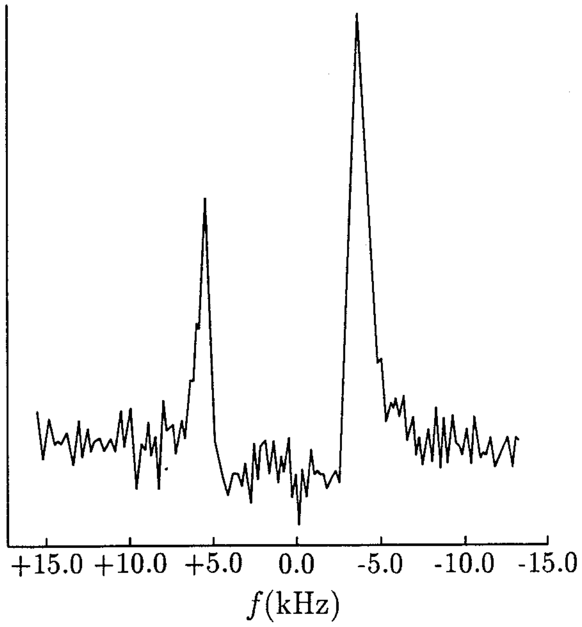

Figure 2.21: Typical spectrum of the FT-NMR of $TiO_2(^{45}Sc)$.

static magnetic field. The crystalline ⟨010⟩ axis was placed close to the rotation axis. The frequencies of the two resonance lines that originated from the two field gradients parallel to ⟨110⟩ or/and ⟨1$\bar{1}$0⟩ are given in figure 2.22. The angular dependencies of the two transitions were accounted for mainly by the second-order quadrupole shifts. In analyses of the spectra, data were compared with the exact solution of the interactions calculated by a computer. The solid curves shown in the figure were the theoretical curves best fit to the data. The experimental results concerning the quadrupole interactions of ^{45}Sc are given in table 3.1, and are summarized as

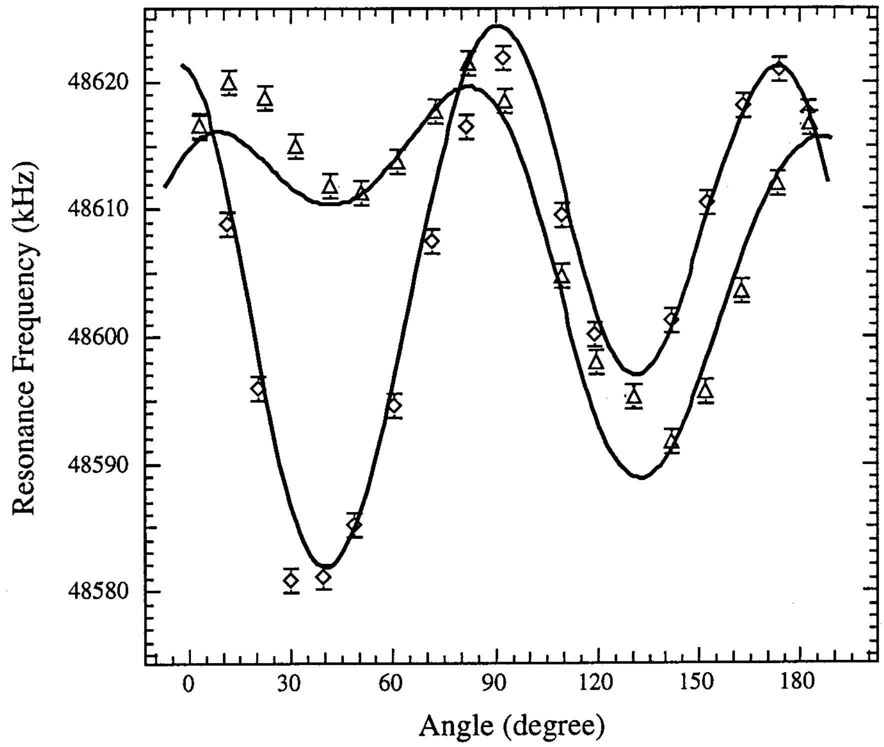

Figure 2.22: NMR of ^{45}Sc($I^{\pi} = 7/2^{-}$) in substitutional sites of Ti atoms in TiO$_2$. The abscissa is the rotation angle around an axis , *i.e.*, close to ⟨100⟩, that is perpendicular to the static magnetic field. The NMR signals corresponded to the two transitions between $m = 1/2 \leftrightarrow m = -1/2$ for the two field gradients in the (110) plane in the substitutional site of Ti in TiO$_2$.

$$\begin{aligned} |eqQ(^{45}\text{Sc in TiO})_2/h| &= 11.99 \pm 0.12 \text{ MHz}, \\ \eta &= 0.538 \pm 0.020. \end{aligned} \tag{2.20}$$

Chapter 3

Experimental results

3.1 Experimental results of NNQR of ^{41}Sc and FT-NMR of ^{45}Sc

A typical experimental spectrum of the NNQR detection of ^{41}Sc in a TiO_2 crystal, giving the asymmetry change as a function of the quadrupole coupling frequency, ν_Q, is shown in figure 3.1. In the figure, the theoretical curve best fit to the data is shown by a solid curve. In a calculation of the theoretical NNQR effect, the spread in the field gradient,

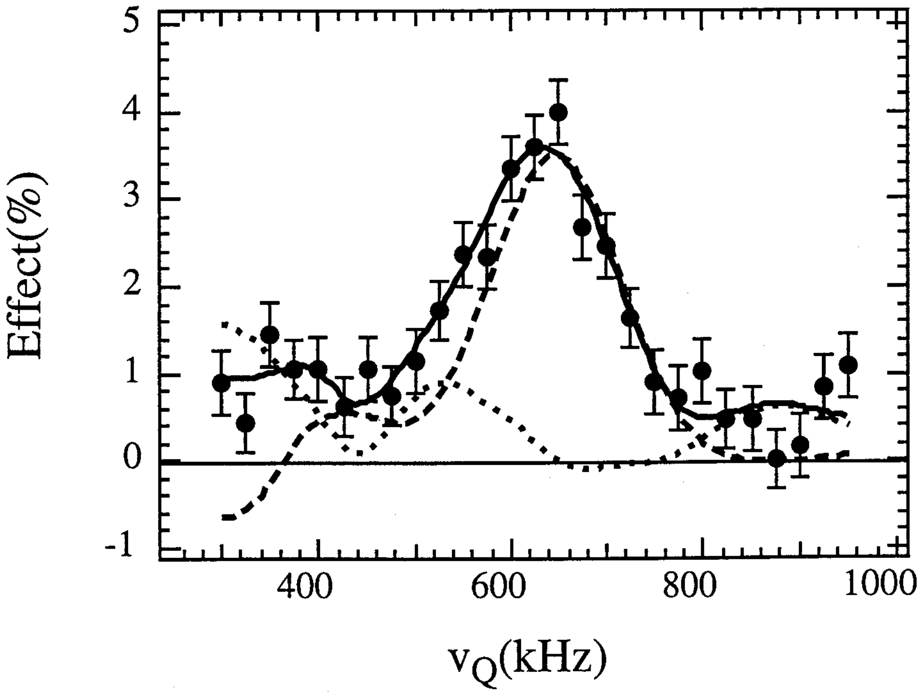

Figure 3.1: Quadrupole spectrum (NNQR) of ^{41}Sc implanted in TiO_2 at a high field The asymmetry change was measured as a function of the quadrupole coupling frequency, $\nu_Q = 3eqQ/2I(2I-1)$. The solid curve is the theoretical best fit to the data, resulting in $\Delta q/q = 8.7\%$, $f_1 = 0.03$ and $f_2 = +0.028$. The broken and dotted curves are the separated components for the single and double quantum transitions, respectively.

Δq, the dipolar broadening, the intensities of the RF's, the double quantum transitions (DQ), and the widths of the frequency modulations, were taken into account. Also, the relative differences in the populations between any adjacent levels were simultaneously taken into account. The small NNQR effects detected at the higher coupling frequencies in the figure than the observed main one, and at the lower frequencies are due to a partial saturation of several RF transitions among the true 7 transitions ($\pm 7/2 \leftrightarrow \pm 5/2$, $\pm 5/2 \leftrightarrow \pm 3/2$, $\pm 3/2 \leftrightarrow \pm 1/2$, and $+1/2 \leftrightarrow -1/2$) by several RF's among the applied 7 RF's; the polarization was only partly destroyed. The dotted curve is the partial NNQR effect calculated for the transitions due only to the DQ (double quantum) transitions. The broken curve is due only to the single quantum transitions.

The experimental results are following; the quadrupole coupling constant of ^{41}Sc in a TiO$_2$ crystal was

$$\begin{aligned} |\nu_Q| = \left|\frac{3eqQ}{2I(2I-1)h}\right| &= 646 \pm 6 \text{ kHz}, \\ |eqQ(^{41}\text{Sc in a TiO}_2\text{ crystal})| &= 9.05 \pm 0.08 \text{ MHz}, \end{aligned} \tag{3.1}$$

the spread in the electric field gradient at the Ti site in a TiO$_2$ crystal was

$$\left|\frac{\Delta q}{q}\right| = 8.7 \pm 0.7\% \qquad \text{(HWHM)}, \tag{3.2}$$

and the polarization and the alignment of ^{41}Sc nuclei preserved in a TiO$_2$ crystal were

$$\begin{aligned} P &= \frac{1}{I}\sum_{m=-I}^{I} m p_m = 0.03, \\ f_2 &= \frac{1}{I^2}\{\sum_{m=-I}^{I} m^2 p_m - \frac{I(I+1)}{3}\} = 0.03 \pm 0.01, \end{aligned} \tag{3.3}$$

and summarized in table 3.1 for both the ^{41}Sc and ^{45}Sc cases. By combining the present result of ^{41}Sc (3.1) with that of ^{45}Sc determined by FT-NMR detection as

$$|eqQ(^{45}\text{Sc in a TiO}_2\text{ crystal})| = 11.9 \pm 0.12 \text{ MHz}, \tag{3.4}$$

the ratio of the quadrupole moment of ^{41}Sc to that of ^{45}Sc was then deduced as

$$\begin{aligned} \left|\frac{Q(^{41}\text{Sc})}{Q(^{45}\text{Sc})}\right| &= \left|\frac{eqQ(^{41}\text{Sc; TiO}_2)}{eqQ(^{45}\text{Sc; TiO}_2)}\right| \\ &= 0.755 \pm 0.012. \end{aligned} \tag{3.5}$$

The spread in the observed field gradient for which a Gaussian spread was assumed in the data analysis, is $|\Delta q/q| = 0.087 \pm 0.007$, is rather wide compared with other cases. It was about 5.6% for ^{17}F in MgF$_2$, for which the ambient of the final sites was considered to be more stable than that of the present case, since ^{17}F was implanted in the substitutional site of the same F isotope [13].

Table 3.1: Experimental results of ^{41}Sc in TiO$_2$ and ^{45}Sc in TiO$_2$

	NNQR of ^{41}Sc in TiO$_2$	FT-NMR of ^{45}Sc in TiO$_2$
Magnetic field	$H_0 = 0.6000$T	4.7T
RF	multi RF's(7 RF's)	pulsed NMR (Fourier transformed)
RF magnetic field	~0.2 mT	
Crystal orientation	c-axis parallel to H_0	Measurement as a function of rotation angle around an axis close to $\langle 100\rangle$ which is vertical to H_0
Results:		
eqQ/h	9.05 ± 0.08 MHz	11.99 ± 0.12 MHz
Asymmetry parameter	obtained in FT-NMR of ^{45}Sc	$\eta = 0.54 \pm 0.02$
$\Delta q/q$	$(8.7 \pm 0.7)\%$	
f_1[a]	0.03	
f_2[b]	$+0.03 \pm 0.01$	
$\lvert Q(^{41}\mathrm{Sc})/Q(^{45}\mathrm{Sc})\rvert =$	0.755 ± 0.012	

[a] Nuclear polarization $f_1 = P = \sum m \cdot p_m / I$

[b] Nuclear alignment $f_2 = \{\sum m^2 \cdot p_m - \frac{1}{3} I(I+1)\}/I^2$

The electric quadrupole moment of ^{45}Sc without the Sternheimer correction (Appendix E) was determined as summarized in table 3.2. It should be noted that these values did not include the effect of the Sternheimer effect. We call then these values uncorrected quadrupole moments and adopted an uncorrected quadrupole moment of ^{45}Sc,

Table 3.2: $Q(^{45}\mathrm{Sc})$ without Sternheimer correction

	$Q_{uncorr}(^{45}\mathrm{Sc})$ (fm^2)	Observed states of ^{45}Sc
G. Fricke, *et al.* [18]	-22 ± 1	$^2D_{3/2}$, $^2D_{5/2}$
W. Ertmer and B. Hofer [19]	-22 ± 1	$^4F_{3/2}$, $^4F_{9/2}$
W. J. Childs [20]	-21.6	$^2D_{3/2}$, $^2D_{5/2}$

$$Q_{uncorr}(^{45}\mathrm{Sc}) = -22 \pm 1 \ \mathrm{fm}^2, \tag{3.6}$$

with an uncertainty that originated from a calculation of the electric-field gradient. By inserting this value into equation 3.5 we obtained the uncorrected electric-quadrupole moment of ^{41}Sc,

$$Q_{uncorr}(^{41}\mathrm{Sc}) = -16.6 \pm 0.8\ \mathrm{fm}^2. \tag{3.7}$$

Chapter 4

Discussion

4.1 Derivation of the quadrupole moment of ^{41}Sc

4.1.1 Quadrupole moment of ^{45}Sc

By a study of the quadrupole interaction of ^{41}Sc and ^{45}Sc in a TiO_2 crystal, the ratio of the quadrupole moment of ^{41}Sc to that of ^{45}Sc could be deduced to be

$$|\frac{Q(^{41}\mathrm{Sc})}{Q(^{45}\mathrm{Sc})}| = 0.755 \pm 0.012. \tag{4.1}$$

By inserting the uncorrected quadrupole moment of ^{45}Sc into this relation, we obtained the uncorrected quadrupole moment of ^{41}Sc

$$Q_{uncorr}(^{41}\mathrm{Sc}) = -16.6 \pm 0.8\ \mathrm{fm}^2 \tag{4.2}$$

as explained in the last chapter.

However, there are two problems to be solved. One is the Sternheimer correction, because it is necessary to know the true or corrected quadrupole moment of ^{41}Sc in order to discuss the nuclear structure, and to compare the theoretical values and so on. The Sternheimer correction to the electric field gradient of the Sc atom was estimated as explained later.

Another is the poor precision of the quadrupole moment of ^{45}Sc. The precision of the ratio of the quadrupole moment of ^{45}Sc to that of ^{41}Sc is 1.6%, but the precision of quadrupole moment of ^{45}Sc is 4.5%.; this means that we can determine the quadrupole moment of ^{41}Sc with only 5% precision. Fortunately, we could obtain the quadrupole moment of ^{45}Sc with better precision, by combining the study on the hyperfine interaction of ^{45}Sc atom by G. Fricke, *et al.* and that by W. J. Childs., as following.

The relation between the quadrupole interaction constant in atom, B, and the quadrupole moment, Q, is

$$B(^{2S+1}L_J) = \frac{2J-1}{2(J+1)} b_{nl} \tag{4.3}$$
$$= eqQ$$
$$q = \frac{e}{4\pi\varepsilon_0}\langle\frac{1}{r^3}\rangle, \tag{4.4}$$

where q is the electric-field gradient at the nucleus of the atom studied, and the parameter b_{nl} is independent of the total angular momentum, J. G. Fricke, *et al.* measured the hyperfine structure constants of ^{45}Sc in a weak magnetic field. They derived the parameters $b_{3d}(^2D_{3/2})$, $b_{3d}(^2D_{5/2})$ from equation 4.3, and showed that their values differ by about 5%, indicating that the configuration $3d4s^2$ of the ground states is perturbed by higher configurations.

Table 4.1: Hyperfine interaction constant of a Sc atom

	$B(^2D_{3/2})$	$B(^2D_{5/2})$
G. Fricke ,*et al.*	-26.37(10)	-37.31(10)
W. J. Childs	-26.345(4)	-37.387(12)

W. J. Childs likewise made more precise measurements of the hyperfine constants in a zero field and a strong field. They reduced the parameter b_{nl} by taking the off-diagonal hyperfine effect into account [20],

$$b_{3d}(^2D_{3/2}) = -65.865(10) \text{ MHz}, \tag{4.5}$$

and

$$b_{3d}(^2D_{5/2}) = -65.427(21) \text{ Mhz}. \tag{4.6}$$

These two values, although they are not in agreement within the experimental uncertainties, differ by less than 0.7%. We therefore adopted as the value of b_{3d}

$$b_{3d} = 65.64(23) \text{ MHz}, \tag{4.7}$$

so that the error includes the values of both b_{3d} parameters.

A valence-only calculation of the electric-field gradient of the ground state of Sc atom, q_{uncorr}, was made by G. Fricke ,*et al.*

$$q_{uncorr}(^2D_{3/2}) = 0.5220 \text{ a.u.}, \tag{4.8}$$

where a.u. means atomic unit, which is a unit system with

$$\begin{aligned} e &= 1 \qquad \text{(absolute value of electron charge)}, & (4.9)\\ m_e &= 1 \qquad \text{(mass of electron)}, & (4.10) \end{aligned}$$

and

$$\hbar = 1 \qquad \text{(Plank's constant divided by } 2\pi). \tag{4.11}$$

With these units, relation 4.3 can be represented in a useful form as

$$Q(\mathrm{fm}^2) = -\frac{2J-1}{2(J+1)}\frac{b(\mathrm{MHz})}{2.349647q(\mathrm{a.u.})}. \tag{4.12}$$

From this relation, we could obtain the uncorrected quadrupole moment of ^{45}Sc

$$Q_{uncorr}(^{45}\mathrm{Sc}) = -21.41 \pm 0.08\ \mathrm{fm}^2. \tag{4.13}$$

There are two ways to estimate the electric-field gradient of an atom. That is, (a) combine the valence-only calculation and Sternheimer correction. (b) *ab initio* calculations allowing for a deformation of the core orbitals. While no *ab initio* calculation has been performed, Sternheimer corrections [Appendix E] for the ground state of Sc atom has already been estimated by Sternheimer [22] as well as by Gupta and Sen [23]. The relation between the quadrupole moment, Q_{corr}, (electric-field gradient, q_{corr}) corrected with a Sternheimer correction factor, $C = 1/(1-R)$, and an uncorrected one Q_{uncorr} (q_{uncorr}) is

$$\begin{aligned} B &= eq_{uncorr}Q_{uncorr} \\ &= eq_{corr}Q_{corr}, & (4.14)\\ q_{corr} &= (1-R)q_{uncorr} \\ &= \frac{q_{uncorr}}{C}, & (4.15)\\ Q_{corr} &= CQ_{uncorr} \\ &= \frac{Q_{uncorr}}{1-R}. & (4.16) \end{aligned}$$

The estimated Sternheimer correction factor is listed in table 4.2. Here, we adopted the correction factor

$$C = 1.102 \pm 0.009 \tag{4.17}$$

by averaging the above two factors and adding the uncertainty, so as to include both values. Combining this correction factor into a relation between the true quadrupole moment, Q, and the uncorrected quadrupole moment, Q_{uncorr},

$$Q = C \cdot Q_{uncorr} = \frac{Q_{uncorr}}{1-R}, \tag{4.18}$$

Table 4.2: Sternheimer correction for the ground state of a Sc atom

	R	C
Sternheimer	0.099	1.110
Gupta and Sen	0.085	1.093

the corrected quadrupole moment of ^{45}Sc was reduced to

$$Q(^{45}\mathrm{Sc}) = -23.6 \pm 0.2 \quad \mathrm{fm}^2. \tag{4.19}$$

The precision of the quadrupole moment of ^{45}Sc is 0.85%, which is comparable to that of the ratio of the quadrupole moment of ^{41}Sc to that of ^{45}Sc. Therefore, this enables us to determine the quadrupole moment of ^{41}Sc with better precision.

4.1.2 Quadrupole moment of ^{41}Sc

Substituting this value into equation 4.1, we obtained the corrected quadrupole moment of ^{41}Sc,

$$Q(^{41}\mathrm{Sc}) = -17.8 \pm 0.3 \quad \mathrm{fm}^2. \tag{4.20}$$

The hyperfine constants of Sc isotopes, ^{43}Sc, ^{47}Sc, ^{44}Sc, ^{44m}Sc[1], were measured by R.G. Cornwell, *et al.* using the atomic-beam magnetic resonance method. Measurements were made of the hyperfine structure of these isotopes in the $^2D_{5/2}$ state of the Sc atom; the results are listed in table 4.3 [24]. From these values of B, we could reduce the quadrupole moment of Sc isotopes using the relation

Table 4.3: Hyperfine constant of Sc isotopes

Nucleus	I	$A(^2D_{5/2})$(MHz)	$B(^2D_{5/2})$(MHz)
^{43}Sc	7/2	105.7 ± 0.9	-44 ± 10
^{47}Sc	7/2	122.2 ± 0.5	-38 ± 6
^{44}Sc	2	102.5 ± 1.2	$+18 \pm 8$
^{44m}Sc	6	51.7 ± 0.2	-33 ± 3

$$Q(^{A}\mathrm{Sc}) = \frac{B(^2D_{5/2};^{A}\mathrm{Sc})}{B(^2D_{5/2};^{45}\mathrm{Sc})} Q(^{45}\mathrm{Sc}), \qquad A = 43, 47. \tag{4.21}$$

The results are given in table 4.4 and in figure 4.1. In the figure, the solid line shows

---

[1] isomer of ^{44}Sc ($Ex = 271$ keV, $T_{1/2} = 2.44$ days)

Table 4.4: Quadrupole moments of Sc isotopes

The quadrupole moments of Sc isotopes were derived from the ratio of the hyperfine constant B.

Nucleus	I	Q (fm^2)
^{41}Sc	7/2	-17.8 ± 0.3
^{43}Sc	7/2	-27.7 ± 6.3
^{45}Sc	7/2	-23.6 ± 0.2
^{47}Sc	7/2	-23.9 ± 3.8
^{44}Sc	2	$+11.3 \pm 0.5$
^{44m}Sc	6	-20.8 ± 1.9

the theoretical values calculated by M.G. van der Merwe, *et al.* [30]. They used the effective two-body interaction whose matrix elements were fitted to 494 energy levels in $A = 41 - 66$ nuclei, and they assumed that a ^{40}Ca core and a model space consisting of $0f^n_{7/2}(1p_{3/2}0f_{5/2}1p_{1/2})^m + 0f^{n-1}_{7/2}(1p_{3/2}0f_{5/2}1p_{1/2})^{1+m}$ configurations for the shell-model basis. They obtained the effective charges, $e_p^{eff} = 1.486$ and $e_n^{eff} = 0.846$ as fitted values.

4.2 Core deformation of ^{40}Ca

4.2.1 Effective charges

As explained in the introductory chapter, the quadrupole moment comprises that of the proton group and that of the neutron group as

$$\begin{aligned} Q(N_p, N_n) &= \sqrt{\frac{16\pi}{5}}\Big[\langle \sum e_n^{eff}(\frac{1}{2} + t_z) r_i^2 Y_{20}(\Omega_i)\rangle \\ &\quad + \langle \sum e_p^{eff}(\frac{1}{2} - t_z) r_i^2 Y_{20}(\Omega_i)\rangle\Big] \\ &= e_n^{eff}\tilde{Q}(N_n) + e_p^{eff}\tilde{Q}(N_p), \end{aligned} \tag{4.22}$$

where $t_z = \frac{1}{2}\tau_z$ is the isospin operator, and e_p^{eff} and e_n^{eff} are the effective charges for protons and neutrons, respectively. In many cases, the effective charges are fitted phenomenologically to the experimental data under the assumption of constancy for many transitions in one or several nuclei, as listed in table 4.5. Dhar and Bhatt obtained the effective charges by a least-squares fit between the deformed configuration mixing shell-model calculated and the observed 38 $B(E2)$ values [25]. The best-fit values of the effective charges turned out to be $e_p^{eff} = 1.33 \pm 0.09$ and $e_n^{eff} = 0.64 \pm 0.10$. Recently, Van der Merwe *et al.* derived a new two-body interaction for nuclei in a large part of the 0f1p shell by fitting two-body matrix elements to 494 energy levels of $A = 41 - 66$ nuclei [30].

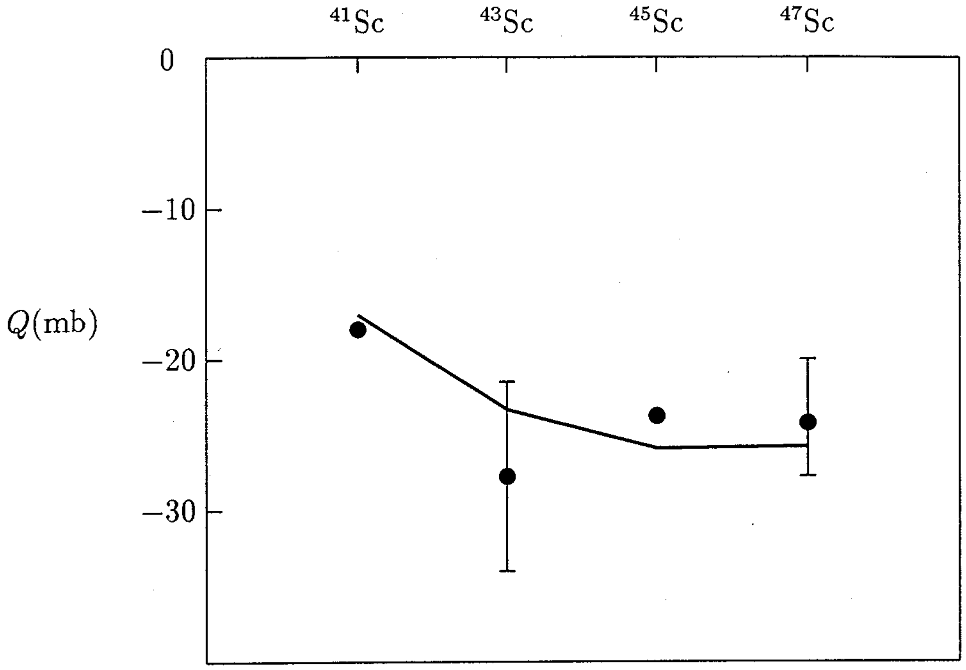

Figure 4.1: Quadrupole moments of Sc isotopes
The solid line shows the theoretical values calculated by M.G. van der Merwe, *et al.* [30]

This study was performed as an extension of a previous study by Richter *et al.* [26], in which they derived for nuclei in the lower part of the 0f1p shell by fitting semi-empirical potential forms and two-body matrix elements to 61 binding and excitation energy data of $A = 41 - 49$ nuclei. They deduced the effective charges, $e_p^{eff} = 1.486$ and $e_n^{eff} = 0.840$, by fitting the theoretical values of quadrupole moments calculated using the new two-body interaction to the experimental values.

There is another way to estimate the effective charges, which was developed by Sagawa and Brown [1] in order to study the core-polarization on the 1s0d-shell single-particle electro-magnetic quadrupole transitions due to coupling with the quadrupole giant resonance. They used perturbation theory to calculate the core-polarization effect due to the

Table 4.5: Effective charges obtained by a fit to the experimental values

	e_p^{eff}	e_n^{eff}
A.K. Dhar *et al.*	1.33±0.09	0.64±0.10
M.G. Van der Merwe *et al.*	1.486	0.840

giant resonance with a modified single-particle wave function expressed as

$$|\tilde{i}\rangle = |i\rangle + \sum_{j,\lambda,\omega_\lambda} \frac{\langle (j \times \omega_\lambda) i | V_{ph} | i \rangle}{\varepsilon_i - (\varepsilon_j + \omega_\lambda)} |(j \times \omega_\lambda) i\rangle. \tag{4.23}$$

In this expression, V_{ph} is the residual particle-hole interaction, which can be derived by the SGII Skyrme-type interaction [Appendix G]. For the calculations of the modified single-particle wave functions and response functions of the giant resonance, they used the self-consistent Hartree-Fock+RPA method. Due to using Skyrme-type interaction, it was easy to solve numerically the differential operator equation concerning the self-consistent Hartree-Fock Hamiltonian, and enabled us to avoid the problem of truncating the particle-hole configuration space. By using this modified single-particle wave functions, they deduced the proton and neutron effective charges with the following definitions:

$$e_p^{eff} = \frac{\langle \tilde{j} \| T_\lambda(q=0) \| \tilde{i} \rangle_\pi}{\langle j \| T_\lambda(q=0) \| i \rangle_\pi} \tag{4.24}$$

and

$$e_n^{eff} = \frac{\langle \tilde{j} \| T_\lambda(q=0) \| \tilde{i} \rangle_\nu}{\langle j \| T_\lambda(q=0) \| i \rangle_\pi}, \tag{4.25}$$

where $T_\lambda(q=0)$ is a one-body operator. Table 4.6 gives the effective charges for the 1s0d hole state and 0f particle state of the ^{40}Ca core. The effective charges obtained by fitting to experimental values are rather larger than those estimated by the Sagawa-Brown method. This indicates the core deformation of the ^{40}Ca core because such a configuration as a core deformation cannot be handled by perturbation theory. We now adopt the effective charges by Sagawa as the effective charges of the quadrupole moments of doubly closed shell+1 nucleon nuclei; that is,

Table 4.6: E2 effective charges for the 1s0d hole states and the 0f particle state in ^{40}Ca

i	j	$e_p^{eff}(i,j)$	$e_n^{eff}(i,j)$
$0d_{3/2}$	$0d_{3/2}$	1.291	0.511
$0d_{3/2}$	$0d_{5/2}$	1.350	0.588
$1s_{1/2}$	$0d_{3/2}$	1.342	0.544
$0d_{5/2}$	$0d_{5/2}$	1.301	0.535
$1s_{1/2}$	$0d_{5/2}$	1.384	0.600
$0f_{7/2}$	$0f_{7/2}$	1.311	0.525

$$e_p^{eff} = 1.311 \tag{4.26}$$

and

$$e_n^{eff} = 0.525. \tag{4.27}$$

4.2.2 Additional quadrupole moment due to core deformation

As shown in table 4.7, each theory estimated almost the same values of $\tilde{Q}(21)_p$ and $\tilde{Q}(21)_n$. The table also gives another calculation by Sagawa *et al.*. In that calculation, they used the Wood-Saxon potential as a valance nucleon potential outside of the core in order to account for the loosely bound proton in ^{41}Sc having a separation energy of 1.1 MeV. Aside from a potential depth, the parameters of the Wood-Saxon potential were taken from the ref. [28], and the depth parameter was adjusted so as to reproduce the experimental separation energy of the single-particle state in each shell-model configuration [27]. The nuclear structure of ^{41}Sc is not identical to that of ^{41}Ca, at least concerning its radial extensions. Such distributions give separation energies of 8.9 and 8.4 MeV for the deeply bound protons and neutrons in ^{41}Ca, respectively.

From these values and each effective charge, the zero values of $\tilde{Q}(20)_p$ and $\tilde{Q}(20)_n$ can be deduced. The zero value of $\tilde{Q}(20)$ means that each theory calculated the physics property under the assumption of a spherical ^{40}Ca core, though they used different interactions. As can be seen in the table, no theoretical calculation could explain the so far known experimental values. Especially, all theoretical absolute values of the quadrupole moment of ^{41}Sc were rather smaller than that of the experimental value. Even if we adopt large effective charges, $e_p^{eff} = 1.486$ and $e_n^{eff} = 0.84$, as performed by Van der Merwe, we cannot explain the experimental values, and these discrepancies indicate something wrong, *i.e.*, in deriving field gradients for Ca, or in neglecting core-deformation.

Table 4.7: Theoretical values of $\tilde{Q}(21)$ and $\tilde{Q}(20)$.

	$\tilde{Q}(21)_p$	$\tilde{Q}(21)_n$	e_p^{eff}	e_n^{eff}	$Q_{th}(^{41}\mathrm{Sc})$	$Q_{th}(^{41}\mathrm{Ca})$
a)Sagawa *et al.*	-11.0	-10.6	+1.311	+0.525	-14.5	-5.6
b)Sagawa *et al.*	-11.54	-10.75	+1.311	+0.525	-15.13	-5.64
Richter *et al.*	-11.4	-11.4	+1.33	+0.64	-15.1	-7.3
Van der Merwe *et al.*	-11.36	-11.36	+1.486	+0.840	-16.88	-9.55
experimental value					-17.8 ± 0.3	-6.65 ± 0.18 [2] -9.00 ± 0.18

a) b) In the calculation of b) the Wood-Saxon potential for the valance nucleon as substitute for the interaction used in a) calculation was used.

In order to account for these discrepancies between the theoretical values and the known experimental one, we suggest a core deformation. Such an additional quadrupole

---

[2] See next section.

moment due to a core deformation can be estimated based on the difference in the experimental value of the quadrupole moment and the theoretical value based on the assumption of a spherical core. For the case of ^{41}Sc nuclei, the core-deformation effect to the quadrupole moment can be extracted as follows:

$$Q_{def}(\mathrm{Sc}) = Q_{exp}(^{41}\mathrm{Sc};7/2) - Q_{th}(p)e_p^{eff}. \tag{4.28}$$

Using the value, $Q_{exp}(^{41}\mathrm{Sc}) = -17.8 \pm 0.3$ fm^2, the effective charge, $e_p^{eff} = 1.311$, and $\tilde{Q}(21)_p = -11.54$ fm^2, we can deduce the core deformation effect as

$$Q_{def} = -2.7 \pm 0.3 \quad \mathrm{fm}^2. \tag{4.29}$$

This value can account for the discrepancy in ^{41}Sc.

4.2.3 Quadrupole moment of ^{41}Ca

As performed in the estimation of the deformation of ^{40}Ca core using the experimental value of the quadrupole moment of ^{41}Sc, we can similarly estimate the core deformation from the quadrupole moment of ^{41}Ca using the equation

$$Q_{def}(\mathrm{Ca}) = Q_{exp}(^{41}\mathrm{Ca};7/2) - Q_{th}(n)e_n^{eff}. \tag{4.30}$$

We first study the atomic field gradient of Ca-atom, since different values of quadrupole moments of ^{41}Ca were reported based on the quadrupole moments of ^{43}Ca and ^{45}Ca, as listed in table 4.8. Their values were deduced from a combination of the identical hyperfine constant, B, of the stable isotope ^{43}Ca, $B = -4.642 \pm 0.012$ MHz [31], and the estimation of the electric field gradient, q, at the nucleus of the Ca atom, as shown in table 4.8. In the estimation of the field gradient, Salomonsson performed many-body perturbation theory (MBPT) calculations on the hyperfine structure parameters of the $4s3d$ and $4s4p$ configurations of Ca [32]. In the MBPT calculation, the core-valence and core-core pair effects were evaluated by solving the radial pair equations for excitations involving one or

Table 4.8: Quadrupole moments of ^{41}Ca, ^{43}Ca, and ^{45}Ca

	q(a.u.)	$Q(^{41}\mathrm{Ca})$	$Q(^{43}\mathrm{Ca})$	$Q(^{45}\mathrm{Ca})$
S. Salomonsson [32]	-0.4032	-8.0 ± 0.8	-4.9 ± 0.5	56 ± 20
D. Sundfolm *et al.* [33]	-0.4841	-6.65 ± 0.18	-4.08 ± 0.08	4.7 ± 1.2

two core electrons. He deduced a weighted average for $Q(^{43}\text{Ca})$ of -4.9 ± 0.5 fm^2, which has been considered to be a standard value for $Q(^{43}\text{Ca})$.

Also, D. Sunderholm *et al.* performed a finite-element multiconfiguration Hartree-Fock (MCHF) calculation for the electric-field gradient of Ca atom. They extended the active space in the MCHF calculation to a range including the $2p$ orbit, which has a lower limit for the number of electrons; they deduced an electric-field gradient, q, of -0.4841 a.u. and a $Q(^{43}\text{Ca})$ of -4.08 ± 0.08 fm^2, which was 17% less than the Salomonsonn's value. They insisted that this discrepancy between their result and Salomonsson's result was probably due to the polarization of the $2p$ shell. They found that the effect of $2p$ polarization is -0.0889 a.u. on the value of electric-field gradient.

In order to obtain a reliable value of q, we performed an MCHF calculation using another program code, which had been developed by C. F. Fischer [34], and modified for the large active space by us. With the program code used to evaluate the hyperfine constants from the wavefunctions obtained by MCHF calculation [35], we estimated the electric-field gradient at the nucleus of Ca($3d4s,^1D_2$) as a function of the active space, as shown in table 4.9. The active space was divided into the three restricted active space

Table 4.9: Electric-field gradient at the nucleus, q, of Ca($3d4s,^1D_2$) as a function of the active space

Active space [3]	ID	q(a.u.) present work	q(a.u.) Sundholm [33]
$3s2p//1s1d$ HF	Ca1	-0.35961	-0.3596
$3s2p//2s2p2d$	Ca2	-0.35004	-0.3500
$3s2p//4s3p4d$	Ca3		-0.3486
$3s3p//4s3p4d2f$	Ca4	-0.32800	-0.3281
$3s2p//4s3p4d2f1g$	Ca5	-0.32678	-0.3269
$3s2p//2s2p2d1f$	Ca6	-0.32953	-0.3295
$2s1p//1s1p\{7\}/2s2p2d-5s5p2d$	Ca7		-0.4369
$2s1p//1s1p\{7\}/2s2p2d-4s4p4d$	Ca8	-0.42929	-0.4369
$2s//1s2p\{13\}/2s2p2d-5s5p2d$	Ca9		-0.5253
$2s//1s2p\{13\}/2s2p2d-4s4p4d$	Ca10	-0.39197	-0.5258
$2s1p//1s1p\{6\}/1s1p1d/1s1p1d1f-2s2p2d(2)$	Ca11		-0.4070

(RAS): RAS I, where a lower limit for the number of electrons was given; RAS II, where no restriction on the number of electrons; and RAS III, where a upper limit for the number of electrons was given [33]. With these RAS's the active space was represented by the following notations as

IO // RAS I {n1} // RAS II // RAS III (n3)

IO : inactive orbitals

n1 : minimum number of electrons in RAS I

n3 : maximum number of electrons in RAS III

When a hyphen appears in the notation, this means that all of the orbitals to the left are frozen, while those to the right are optimized.

Based on the present calculation we obtained the effect of $2p$ polarization, that is, the difference $q(\mathrm{Ca10})$-$q(\mathrm{Ca8})$, of +0.0373 a.u., which had an opposite sign to Sundholm's result, −0.0889 a.u. With our result, the electric-field gradient of $\mathrm{Ca}(3d4s,{}^1D_2)$ was deduced,

$$q(\mathrm{Ca}(3d4s,{}^1D_2)) = 0.3579 \text{ a.u.} \tag{4.31}$$

This result includes the f-shell contribution, the g-shell contribution, and a relativistic correction to the $3s3p$ correlation *spd* limit, just as in Sundholm's result and a different $2p$ contribution. The uncertainty of the calculated q was estimated to be about 2.1%. From the present result(4.31) and the known relation(4.12), we deduced the quadrupole moment of $Q(^{43}\mathrm{Ca})$ as -5.52 ± 0.08 fm^2. From the following relations:

$$\frac{Q(^{41}\mathrm{Ca})}{Q(^{43}\mathrm{Ca})} = 1.630 \pm 0.011 \qquad \text{ref. [36]} \tag{4.32}$$

$$\frac{Q(^{45}\mathrm{Ca})}{Q(^{41}\mathrm{Ca})} = -0.70 \pm 0.18 \qquad \text{ref. [37]} \tag{4.33}$$

and

$$\frac{Q(^{47}\mathrm{Ca})}{Q(^{43}\mathrm{Ca})} = -0.42 \pm 0.07 \qquad \text{ref. [38]}, \tag{4.34}$$

the nuclear quadrupole moments of the ^{41}Ca, ^{45}Ca and ^{47}Ca were deduced to be -9.00 ± 0.12 fm^2, $+6.3 \pm 1.2$ fm^2 and $+2.3 \pm 0.3$ fm^2, respectively, as shown in table 4.10. We can now discuss the core deformation using the quadrupole moment of ^{41}Ca and the given equation 4.30. With the present quadrupole moment, $Q(^{41}\mathrm{Ca})$, of -9.00 ± 0.12 fm^2 and the effective charge, e_n, of 0.525, the quadrupole moment due to core deformation was deduced to be

$$Q_{def}(^{41}\mathrm{Ca}) = -3.0 \pm 0.1 \quad \mathrm{fm}^2. \tag{4.35}$$

---

[3] See text and reference [33]

Table 4.10: Present nuclear quadrupole moments of calcium isotopes

They are compared to the standard values and the Sundholm's values

Isotope	Q (fm^2) present work	Q (fm^2) Sundholm and *et al.*[33]	Q (fm^2) standard value [39]
^{41}Ca	-9.00 ± 0.12	-6.65 ± 0.18	-8.0 ± 0.8
^{43}Ca	-5.52 ± 0.08	-4.08 ± 0.08	-4.9 ± 0.5
^{45}Ca	$+6.3 \pm 1.2$	$+4.7 \pm 1.2$	4.6 ± 1.4
^{47}Ca	$+2.3 \pm 0.3$	$+1.7 \pm 0.3$	2.1 ± 0.4

This value is in good agreement with the value obtained from an analysis of the quadrupole moment of ^{41}Sc.

However, we have to realize that the present result depends on the restricted active-space calculation of the field gradient. We thus need to develop a full active-space calculation.

4.2.4 Core deformation of ^{40}Ca core

As explained in the last section, we could deduce the quadrupole moment originating from the core deformation of ^{40}Ca core in A=41 nuclei as

$$Q_{def} = -2.7 \pm 0.3 \text{ fm}^2. \tag{4.36}$$

In principle, by use of spectroscopic methods, we cannot observe a finite quadrupole moment of the ground state of ^{40}Ca nucleus, because it has a zero spin. It can, however, have a finite intrinsic quadrupole moment, and in generally the relation between an observed quadrupole moment, Q, and an intrinsic quadrupole moment, Q_0, is represented by the following equation

$$Q = \frac{2I-1}{2(I+1)} Q_0. \tag{4.37}$$

By using the experimental value, $Q_{def} = -2.7 \pm 0.3$ fm^2, and equation 4.37, we can obtain for the A=41 nuclei an intrinsic deformation Q_{def0} as

$$Q_{def0}(A = 41) = -4.1 \pm 0.5 \text{ fm}^2 \tag{4.38}$$

Because Q_{def0} does not include any contribution of an extra nucleus out of the core to the charge distribution, we can assume

$$Q_{def0}(A = 40) \simeq Q_{def0}(A = 41). \tag{4.39}$$

If we assume an oblate deformation for the Ca core, we can relate the distortion parameter, δ, to the intrinsic quadrupole moment due to the core deformation, Q_{def}, in a simple form as follows [29]:

$$\delta = \frac{R_z - R_x}{R_0}, \tag{4.40}$$

$$Q_{def0} = \frac{4}{3}\langle r^2 \rangle Z\delta. \tag{4.41}$$

$$\tag{4.42}$$

Here, R_0 is the spherical radius that makes the same volume as the deformed core, that is, $R_0^3 = R_x^2 R_z$. This radius can be represented empirically using the mass number, A, as

$$R_0 = r_0 A^{1/3} \qquad r_0 \sim 1.2 \text{ fm}^2, \tag{4.43}$$

and can be related to $\langle r^2 \rangle$ as

$$\langle r^2 \rangle = \frac{3}{5} R_0^2. \tag{4.44}$$

Substituting these relations (4.43, 4.44) into the equation with $A = 40$ and Z=20, Q_{def0} is reduced to

$$Q_{def0} = 270\ \delta\ \text{ fm}^2. \tag{4.45}$$

From the experimental value, $Q_{def0} = -4.1 \pm 0.5$ fm^2, we can obtain a core deformation of $\delta = -1.5 \pm 0.2\%$ in order to account for the experimental quadrupole moment of ^{41}Sc. This deformation parameter is very small but makes a large contribution to the quadrupole moment, that is, 15%.

4.3 Correction to isovector magnetic moments due to core deformation

Though the core deformation of the Ca core in a ^{41}Sc nucleus is small, $\delta = -1.5\%$, as seen from the analysis performed in the last section, it can make an appreciable contribution to the magnetic moment of ^{41}Sc. The reason is that some configurations causing an extra quadrupole moment cannot be handled by the perturbation theory. In other words, the space of configurations of a ^{41}Sc nucleus including a deformed state of ^{40}Ca core are larger than the space constructed by the second-order configuration mixing based on the spherical ^{40}Ca core.

The core deformation does not affect isoscalar magnetic moments [7]. Therefore, we focus on the discussion on isovector magnetic moments. Because isovector magnetic moments are strongly depend on a core deformation, in order to extract conclusive results on effective g-factors, $g^{(1)}_{\ell eff}$ and $g^{(1)}_{S eff}$, from the analysis of mirror nuclei, we must estimate the correction to the magnetic moment due to the core deformation, $\delta\mu_{def}$. This enables us to understand the common mechanism of nuclei over the different shell, *i.e.,* the difference of the set of g factors between A=16 system and A=40 one will be disclosed reliably.

In order to estimate the correction to the magnetic moment due to the core deformation, we adopt the Nillson's wave function to describe the deformed-wave function of the Ca core, namely, a 3p-2h configuration as seeing in figure 4.2. This deformed wave

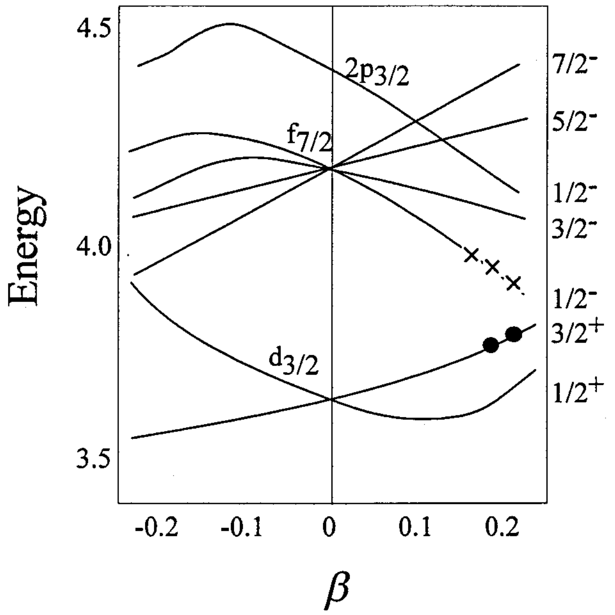

Figure 4.2: Relevant section of Nillsson diagram showing three-particle-two-holes state.

function was originally used by W.J. Gerace and A.M. Green in order to explain the low-lying levels of ^{40}Ca, ^{41}Ca, ^{42}Ca, and ^{41}Ca [40]. As seen in the Nillson's diagram, the single particle energy of $d_{3/2}$ orbit comes near that of $f_{7/2}$ orbit around $\beta \sim 0.25$. This deformed-wave function can be represented by the following equation:

$$\begin{aligned} |\mathrm{def.}, J = 7/2\rangle &= NP_{J=7/2}|d^{-2}_{3/2}(T_h = 1, K = 0) \qquad (4.46) \\ &\quad (f_{7/2}p_{3/2})^3(T_p = 1/2, K = 1/2)T = 1/2, K = 1/2\rangle, \end{aligned}$$

where N and $P_{J=7/2}$ are the normalization factor and the projection operator for the $J = 7/2$ state, and T_h and T_p are the total isospins of the two holes and the three particles, respectively. The wave function of ^{41}Sc is written as a mixed state of this 3p-2h

Table 4.11: Dependence of overlap factor α^2 on deformation parameter β

β	0.15	0.23	0.31
α^2	0.08	0.15	0.26

deformed state with $\beta = 0.25$ and the 1p-0h spherical state

$$\Psi(^{41}\mathrm{Sc}) = \sqrt{1-\alpha^2}|f_{7/2}\rangle + \alpha|def.J = 7/2\rangle, \tag{4.47}$$

where α^2 is the overlap factor of the $f_{7/2}$ single-particle wave function and the deformed state wave function. The overlap factor, α^2, depends strongly on the parameter β [40] as shown in table 4.11 and in figure 4.3. Generally, the deviation of the matrix element of a one body operator $\hat{\theta}$ from its single-particle value is given by

$$\delta\langle\hat{\theta}\rangle = \alpha^2\{\langle def.J = 7/2|\hat{\theta}|def.J = 7/2\rangle - \langle f_{7/2}|\hat{\theta}|f_{7/2}\rangle\}. \tag{4.48}$$

Therefore, the extra quadrupole moment due to the core deformation of the ^{40}Ca core, δQ, for ^{41}Sc is given by

$$\delta Q_{def} = \alpha^2\{\langle def.J = 7/2|\hat{Q}|def.J = 7/2\rangle - \langle f_{7/2}|\hat{Q}|f_{7/2}\rangle\}. \tag{4.49}$$

The quadrupole moment of deformed waved function, $\langle def.J = 7/2|\hat{Q}|def.J = 7/2\rangle$, can be represented approximately by

$$\begin{aligned} Q_{def} &= \langle def.J = 7/2|\hat{Q}|def.J = 7/2\rangle & (4.50) \\ &= \frac{3K^2 - I(I+1)}{(I+1)(2I+3)} \cdot \frac{3}{\sqrt{5\pi}} R_0^2 Z\beta. & (4.51) \end{aligned}$$

on the assumption that the deformation of the density distribution is as almost same as that of the deformation of potential, which is true if the binding energy of the nucleon is not very small.

Using the following parameters, $I = 7/2$, $K = 1/2$, $A = 41$, and $Z = 21$, we can obtain $Q_{def} = -105\beta$ fm^2. In the meanwhile, if we assume the observed quadrupole moment can be explained by the deformed wave function, the observed quadrupole moment can be represented as

$$\begin{aligned} Q_{exp} &= Q_{SP} + \delta Q_{CM} + \delta Q_{def} & (4.52) \\ &= Q_{theory} + \alpha^2(Q_{def} - Q_{SP}) & (4.53) \end{aligned}$$

where $Q_{theory} = Q_{SP} + Q_{CM}$ is the theoretical value based on the perturbation approach with a spherical potential, $Q_{SP} = \langle f_{7/2}|\hat{Q}|f_{7/2}\rangle$ is a single-particle value, and δQ_{CM} is the deviation form single-particle quadrupole moment due to configuration mixing. Using the extra quadrupole moment derived from the experimental value, $\delta Q_{def} = -2.7$ fm^2, and the single-particle quadrupole moment, $Q_{SP} = -11.4$ fm^2, we can obtain another relation between α^2 and β as shown in figure 4.3. From the cross point of the experimental line

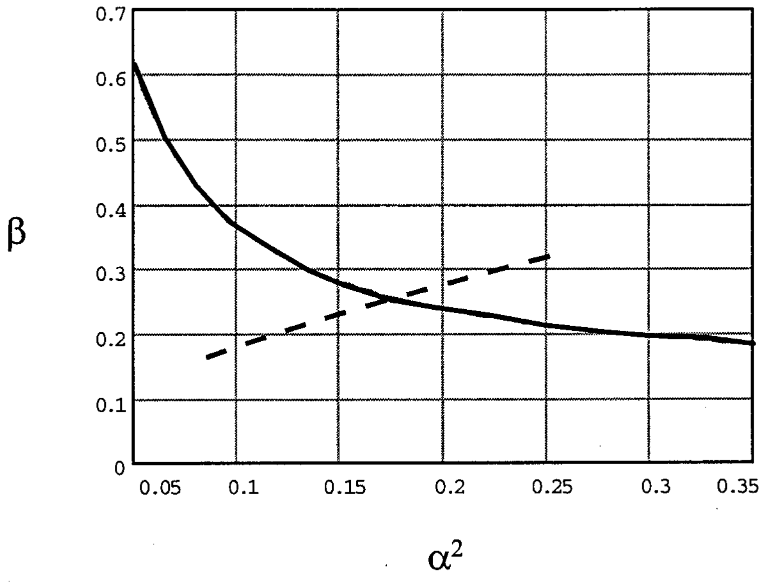

Figure 4.3: Relation between deformation parameter β and overlap factor α^2
The solid line shows the relation between α^2 and β obtained from the experimental value and the dashed line shows that obtained from the wave function based on the deformed potential of Nillson model.

and theoretical line based on the deformed potential of Nillson model, we obtained the overlap factor $\alpha^2 = 0.17$.

In the same way as quadrupole moment, the deviation of magnetic moment from the single-particle value can be written as

$$\delta\mu_{def} = \alpha^2\{\langle def.J = 7/2|\hat{\mu}|def.J = 7/2\rangle - \langle f_{7/2}|\hat{\mu}|f_{7/2}\rangle\}, \tag{4.54}$$

with $\alpha^2 = 0.17$. The correction to $\langle\mu^{(1)}\rangle$ and $\langle\tau s\rangle$ for A=41 nuclei is given in the first row of table 4.12. Because the second-order perturbation calculation contains 3 particles-2 holes configuration mixing, we must subtract the correction coming from 3p-2h configuration mixing by the perturbation calculation from the correction due to the deformed state. This 3p-2h configuration-mixing correction coming from $2\hbar\omega$ excitations are given in the second row of table 4.12 [7]. Then we can obtain the correction to the isovector magnetic moment due to the core deformation, $\delta\mu^{(1)}/\langle\mu^{(1)}\rangle_S = -0.099$, and the correction

Table 4.12: Correction to isovector magnetic moment due to the deformed state of the ^{40}Ca core

	$\delta\langle\mu^{(1)}\rangle/\langle\mu^{(1)}\rangle_S$ (%)	$\delta\langle\tau s^{(1)}\rangle/\langle\tau s^{(1)}\rangle_S$ (%)
(a) Deformed state	-13.5	-12.5
(b) CM (3p-2h)	-3.6	-0.9
(c) {(a)-(b)}	-9.9	-11.6

Table 4.13: Isovector magnetic moment of A=41 nuclei
Corrections to the isovector magnetic moment of A=41 nuclei due to the configuration mixing, the exchange current, the relativistic effect, and the core deformation was shown. Corrections due to the configuration mixing and the exchange current was cited from [7, 5], and the relativistic correction from [12].

(a) Schmidt value	$\langle\mu^{(1)}\rangle_S$	3.853
(b) configuration mixing	$\delta\langle\mu^{(1)}\rangle_{CM}$	-0.892
(c) exchange current	$\delta\langle\mu^{(1)}\rangle_{EX}$	0.763
(d) relativistic correction	$\delta\langle\mu^{(1)}\rangle_{rel}$	-0.0685
(e) core deformation	$\delta\langle\mu^{(1)}\rangle_{def}$	-0.381
(f)	(a)+(b)+(c)+(d)	3.660
(g)	(a)+(b)+(c)+(d)+(e)	3.279
Experimental value	$\langle\mu^{(1)}\rangle_{exp}$	3.5126

to Gamov-Teller-type β-decay matrix element coming from the deformed state of ^{40}Ca core, $\delta\langle\tau s^{(1)}\rangle/\langle\tau s^{(1)}\rangle_S = -0.116$.

Adding this correction to the isovector magnetic moment due to the core deformation to the corrections due to the configuration mixing and the exchange current, which were calculated by Arima [7], we can obtain $\langle\mu^{(1)}\rangle = 3.3472\ \mu_N$, as shown in table 4.13. In this table, $\delta\langle\mu^{(1)}\rangle_{CM}$ and $\delta\langle\mu^{(1)}\rangle_{EX}$ are composed of the contributions from the isovector angular moment, the isovector spin, and the isovector tensor term

$$\begin{aligned} \delta\langle\mu^{(1)}\rangle_{CM} &= \delta g_{\ell CM}\langle\tau_3\ell_z\rangle_S + \delta g_{S CM}\langle\tau_3 S_z\rangle_S + \delta g_{P CM}\langle\tau_3 Y\times S\rangle_S \\ \delta\langle\mu^{(1)}\rangle_{EX} &= \delta g_{\ell EX}\langle\tau_3\ell_z\rangle_S + \delta g_{S EX}\langle\tau_3 S_z\rangle_S + \delta g_{P EX}\langle\tau_3 Y\times S\rangle_S, \end{aligned} \qquad (4.55)$$

where $\delta\langle\mu^{(1)}\rangle_{EX}$ includes the contribution of the crossing term, $\delta\langle\mu^{(1)}\rangle_{cross}$, between the meson exchange currents and the modified wave functions due to the configuration mixing. The theoretical value without correction due to the core deformation, (f), was 4.2% larger than the experimental value. On the other hand, the correction due to the core deformation, $\delta\langle\mu^{(1)}\rangle_{def}$ decreased the isovector magnetic moment but made an overcorrection, *i.e.*, the corrected value was, (g), was 6.7 % smaller than the experimental value. This overcorrection may be due to the uncertainty of the meson effect on the isovector magnetic moment and/or the rough formation of the deformed wave function of the ground state of A=41 nuclei.

4.4 Meson effects in g-factors of orbital and spin angular momenta

In order to look into the meson effects, let us discuss the effective isovector g-factors, $g^{(1)}_{\ell eff}$ and $g^{(1)}_{S eff}$. As explained in the introduction, if we assume the correction due to the configuration mixing mainly affects the matrix elements of the isovector orbital angular momentum operator and isovector spin operator, $\langle\tau_3 l_z\rangle$ and $\langle\tau_3 S_z\rangle$, and the other corrections such as the exchange currents affect the g-factors, the observed isovector magnetic moment can be represented as

$$\begin{aligned}\langle\mu^{(1)}\rangle_{exp} &- (\delta\langle\mu^{(1)}\rangle_{cross} + \delta\langle\mu^{(1)}\rangle_{P} + \delta\langle\mu^{(1)}\rangle_{def} + \delta\langle\mu^{(1)}\rangle_{rel}) \\ &= \langle\tau_3\ell_z\rangle_{eff} g^{(1)}_{\ell eff} + \langle\tau_3 S_z\rangle_{eff} g^{(1)}_{S eff},\end{aligned} \tag{4.56}$$

where $\langle\tau_3 S_z\rangle = \langle\tau_3 S_z\rangle_S + \delta\langle\tau_3 S_z\rangle_{CM}$ and $\langle\tau_3\ell_z\rangle = \langle\tau_3\ell_z\rangle_S + \delta\langle\tau_3\ell_z\rangle_{CM}$ as shown in table 4.14. Applying the equation 4.57 to the A=39 system and A=41 system with use of the correction values, relativistic corrections, tensor term corrections, crossing term corrections, and deformation correction, listed in table 4.15, we can obtain the effective g-factors as listed in table 4.16. Because the deformation correction, $\delta\langle\mu^{(1)}\rangle_{def}$ has isovector nature, we can assume that $\delta\langle\mu^{(1)}\rangle_{def}$(A=39) = -$\delta\langle\mu^{(1)}\rangle_{def}$(A=41). By combining the effective isoscalar g-factors listed in table A.4 and the effective isovector g-factors, we can obtain the effective g-factors for proton and neutron as listed in table 4.17. The experimental values of δg_ℓ for A=40 region have the same sign as the theoretical predictions $\delta g_\ell(\tau) \sim 0.1\tau$ [52, 53] but the values are about 2.5 times of the prediction, as well as A=16 system.

Table 4.14: Quenched matrix elements of $\tau_3\ell_z$ and $\tau_3 S_z$ quenched due to configuration mixing
The matrix elements of $\tau_3\ell_z$ and $\tau_3 S_z$ are quenched due to configuration mixing as, $\langle\tau_3\ell_z\rangle_{eff} = \langle\tau_3\ell_z\rangle_S + \langle\tau_3\ell_z\rangle_{CM}$, $\langle\tau_3 S_z\rangle_{eff} = \langle\tau_3 S_z\rangle_S + \langle\tau_3 S_z\rangle_{CM}$.

A	$\langle\tau_3 S_z\rangle_S$	$\langle\tau_3 S_z\rangle_{eff}$	$\langle\tau_3\ell_z\rangle_S$	$\langle\tau_3\ell_z\rangle_{eff}$
39	-3/10	-0.2370	9/5	0.7737
41	1/2	0.4260	3	1.9118

Table 4.15: Corrections to isovector moments

A	$\langle\mu^{(1)}\rangle_{cross}$	$\langle\mu^{(1)}\rangle_{P}$	$\langle\mu^{(1)}\rangle_{rel}$	$\langle\mu^{(1)}\rangle_{def}$
39	0.0594	-0.10999	-0.0275	0.3814*
41	0.4123	0.0451	-0.0685	-0.3814

* from isovector nature of $\delta\langle\mu^{(1)}\rangle_{def}$.

Table 4.16: Effective g-factor derived from the isovector magnetic moment including the correction due to the core deformation

	corrected values	uncorrected values	free values
$g_\ell^{(1)}$(eff)	0.725	0.793	0.500
$g_S^{(1)}$(eff)	4.975	3.82	4.71

Table 4.17: Effective nucleon g-factors

	A=40		A=16
	corrected values	uncorrected values	
δg_ℓ(proton)	0.240	0.332	0.269
δg_ℓ(neutron)	-0.210	-0.302	-0.255
δg_S(proton)	0.376	-0.932	-0.173
δg_S(neutron)	-0.162	1.146	0.380

In order to confirm this result, however, we should measure the quadrupole moment of ^{39}Ca of which the quadrupole moment of the mirror partner ^{39}K, $Q(^{39}\mathrm{K})$ was already known. Because there can be a correction due to the core deformation to the isovector magnetic moment of A=39 nuclei as well as A=41 nuclei. In the same way of A=41 case, the wave function of ^{39}Ca may be represented as a mixture of a single hole state and 2p-3h deformed state. From the analysis of the mirror quadrupole moments of ^{39}Ca and ^{39}K, we can obtain the knowledge on the core deformation and derive the correction to the isovector magnetic moment for A=39 nuclei by using the deformed wave function. Furthermore, we will derive also effective g-factor of proton and neutron for A=40 region by combining the results obtained from the isoscalar analysis and the isovector analysis.

Chapter 5

Summary

We measured the nuclear quadrupole moment of ^{41}Sc($I^{\pi} = 7/2^{-}, T_{1/2} = 0.596$s) by using a modified β-NMR technique. and determined, $|Q(^{41}\text{Sc};7/2^{-})| = 17.8 \pm 0.3$ fm^2 In the process of obtaining this result, we measured the field gradient effective to the Sc atoms substituted at Ti site in TiO$_2$ by detecting the FT-NMR of ^{45}Sc in TiO$_2$, and also calculated the Sternheimer effect for the atomic field gradient of Sc atoms. The nuclear quadrupole moments of Sc isotopes were, therefore, deduced as $Q(^{43}\text{Sc}) = -23.9 \pm 3.8\text{fm}^2$, $Q(^{44}\text{Sc}) = +11.3 \pm 0.5\text{fm}^2$, $Q(^{44m}\text{Sc}) = -20.8 \pm 1.9\text{fm}^2$, $Q(^{45}\text{Sc}) = -23.6 \pm 0.2\text{fm}^2$, and $Q(^{47}\text{Sc}) = -23.9 \pm 3.8\text{fm}^2$.

By combining the value with its mirror quadrupole moment, $Q(^{41}\text{Ca}; 7/2^{-})$, it is shown that the valence proton in ^{41}Sc carries more than 85% of the moment, and that of the remaining core carries about 15%. This is consistent with a picture in which the core of ^{41}Sc, ^{40}Ca, is deformed by about $\delta = -1.5 \pm 0.2\%$.

We estimated the correction to the isovector magnetic moment due to the core deformation, $\delta\mu^{(1)}_{def}$, by using the deformed wave function. Furthermore, from the analysis of the 2 pairs of mirror magnetic moments, of A=39 and 41, in which the core-deformation correction was included in A=41 and 39 systems, we extracted the mesonic effect in the g-factors of orbital and spin angular momenta, g_ℓ, g_S, of proton and neutron in A=40 nuclei. The core-deformation correction was estimated from the isovector nature of $\delta\langle\mu^{(1)}\rangle_{def}$. Large enhancement of 24% for proton and reduction of 21% for neutron compared with g_ℓ for free proton were obtained. The absolute values of δg_ℓ's for A=41 and 39 systems are comparable with those for A=17 and 15 systems. In order to confirm this result, we should know the potential shape for A=39; we should measure the quadrupole moment of ^{39}Ca from where we derive $\delta\mu^{(1)}_{def}$ for A=39.

Appendix A

Meson and quark effects in magnetic moments

Table A.1 summarizes the magnetic moments of the LS doubly closed shell ±1 nucleon nuclei together with the isoscalar magnetic moments, defined as

$$\mu^{(0)} = \frac{1}{2}\left\{\mu(T_z = +1/2) + \mu(T_z = -1/2)\right\}. \tag{A.1}$$

The value for the mass-41 system is given as $+1.91785 \pm 0.00085$nm. The deviation of the experimental value from the single-particle value, defined by

$$\frac{\delta\mu^{(0)}_{exp}}{\mu^{(0)}_{S}} = \frac{\mu^{(0)}_{exp} - \mu^{(0)}_{S}}{\mu^{(0)}_{S}}, \tag{A.2}$$

is $-1.14 \pm 0.05\%$.

Regarding the second-order configuration-mixing corrections to the isoscalar magnetic moments of the nuclide around the doubly closed shells, Ichii, Bentz and Arima (IBA) [5], and Towner and Khanna (TK) [6] have independently given theoretical results. In their calculations it was necessary to include the mixing of highly excited configurations up to $12\hbar\omega$ of harmonic-oscillator excitations, as well as tensor correlation, in order to account for the experimental deviations. As can be seen in table A.3, IBA and TK give essentially similar values. Although these theoretical predictions agree fairly well with the experimental values, it should be noted that the configuration-mixing corrections for the mass-41 and mass-17 systems are about twice the experimental values.

Assuming that the sum of the effective g-factors of the proton and neutron inside the nucleus are the same as those of the free proton and neutron, the experimental spin-matrix element of the $A = 41$ system can be extracted from the isoscalar magnetic moment using the following equation, in which the free proton and neutron magnetic moments are used:

$$\langle S_z \rangle_{exp} = \frac{\mu^{(0)}_{exp} - \frac{1}{2}I}{\mu_p + \mu_n - \frac{1}{2}}. \tag{A.3}$$

Table A.1: Magnetic moments of the LS doubly closed-shell ±1 nucleon nuclei

A		I^π	μ_S [nm]	μ_{exp} [nm]	$\delta\mu_{exp}^{(0)\ a)}$ [nm]	$\delta\mu_{exp}^{(0)}/\mu_S^{(0)\ b)}$ (%)	$\delta\mu_{CM}^{(0)}/\mu_S^{(0)}$ (%)	$\Delta/\mu_S^{(0)c)}$
15	^{15}N	1/2$^-$	-0.26428	-0.2831892(3)				
	^{15}O	1/2$^-$	+0.63773	(+)0.7189(8)				
		$2\mu^{(0)}$:	+0.37345	+0.4357(8)	+0.0312(4)	+16.7(2)	+22.85	-6.2(2)
17	^{17}O	5/2$^+$	-1.91315	-1.89379(9)				
	^{17}F	5/2$^+$	+4.79274	(+)4.7223(12)				
		$2\mu^{(0)}$:	+2.87959	+2.8285(12)	-0.0256(6)	-1.78(4)	-2.95	-1.17(4)
39	^{39}K	3/2$^+$	+0.12435	+0.3915063(2)				
	^{39}Ca	3/2$^+$	+1.14789	(+)1.0216(2)				
		$2\mu^{(0)}$:	+0.37345	+1.4131(2)	+0.0705(1)	+11.08(2)	+12.49	-1.41(2)
41	^{41}Ca	7/2$^-$	-1.91315	-1.594780(9)				
	^{41}Sc	7/2$^-$	+5.79274	(+)5.4305(18)				
		$2\mu^{(0)}$:	+3.87959	+3.8357(17)	-0.0221(9)	-1.14(5)	-2.70	1.56(5)

a) $\delta\mu_{exp}^{(0)} = \mu_{exp}^{(0)} - \mu_S^{(0)}$, where the isoscalar magnetic moment is defined by $\mu^{(0)} = \frac{1}{2}\{\mu(T_z = 1/2) + \mu(T_z = -1/2)\}$.
b) $\delta\mu_{CM}^{(0)}/\mu_S^{(0)}$ is the configuration-mixing correction to the isoscalar magnetic moment divided by $\mu_S^{(0)}$ given by Ichii *et al.* [5].
c) $\Delta/\mu_S^{(0)} = \{\mu_{exp}^{(0)} - (\mu_S^{(0)} + \delta\mu_{CM}^{(0)}\}/\mu_S^{(0)}$

The deviation of $\langle S_z\rangle_{exp}$ from the single-particle value, $\langle S_z\rangle_S$, is defined as

$$\frac{\delta\langle S_z\rangle_{exp}}{\langle S_z\rangle_S} = \frac{\langle S_z\rangle_{exp} - \langle S_z\rangle_S}{\langle S_z\rangle_S}. \tag{A.4}$$

A theoretical prediction of IBA based on a configuration-mixing correction to the isoscalar magnetic moment, $\delta\langle S_z\rangle_{CM}$, of the mass-41 system was given as $\delta\langle S_z\rangle_{CM}/\langle S_z\rangle_S = -27.62\%$. The large over-correction of the theoretical value, compared with the experimental one, suggested that we needed to consider not only those small corrections due to the spin-tensor term, the relativistic process and the mesonic exchange currents, but also that due to a renormalization of the nucleon mass in the nucleus.

In a similar way, the isovector magnetic moment is defined by

$$\mu^{(1)} = \frac{1}{2}\left\{\mu(T_z = +1/2) - \mu(T_z = -1/2)\right\}. \tag{A.5}$$

The value for the mass-41 system was 8.83% smaller than that given by the Schmidt moments. The theoretical correction predicted by IBA to the single-particle value for the isovector magnetic moment was -3.21%. In this correction, a large configuration-mixing contribution of -23.14% was almost totally compensated for by a large mesonic exchange correction of 19.93%. Towner also predicted in a formalism similar to that of Ichii *et al.* a tiny deviation of -0.9%. In all events, the theoretical correction is too small to account for the experimental deviation. Experimental and theoretical values are summarized in table A.2. In terms of the spin-isospin matrix element, the theoretical configuration-mixing correction of IBA was -14.80%, and that of TK was -12.1%, showing mutual agreement between the two theories.

Table A.2: Corrections to the isovector combination of the magnetic moment

Mass	$\delta\mu^{(1)}/\delta\mu_S^{(1)}$[%]				
number	IBA CM.	IBA exch.	IBA total	TK	exp.
15	5.49	7.18	12.67	8.9	11.09(9)
17	-16.93	15.52	-1.41	-0.5	-1.34(2)
39	42.22	-48.32	-6.10	-23.9	-38.45(2)
41	-23.14	19.93	-3.21	-0.9	-8.83(2)

Isoscalar moments and deconfinement effect

Based on assumptions that the mesonic exchange current affects the orbital and spin g-factors, and also that the free motion of the renormalized nucleon in a nucleus affects the nuclear magneton, μ_N, these parameters can be rewritten for the proton ($\tau_3 = +1$) and neutron ($\tau_3 = -1$) as

$$\begin{aligned} g_l^{eff}(\tau_3) &= g_\ell^{free}(\tau_3) + \delta g_\ell(\tau_3), \\ g_S^{eff}(\tau_3) &= g_S^{free}(\tau_3) + \delta g_S(\tau_3) \end{aligned} \tag{A.6}$$

and

$$\mu_N^{eff} = \mu_N(1+\kappa), \tag{A.7}$$

where $\mu_N = e\hbar/2M_p$, M_p is the free proton mass and κ is the degree of the renormalization. The deviations of the orbital and spin g-factors satisfy relations in which

$$\delta g_{\ell EX}^{(0)} = \delta g_\ell(\tau_3 = +1) + \delta g_\ell(\tau_3 = -1) = 0 \tag{A.8}$$

and

$$\delta g_{S EX}^{(0)} = \delta g_S(\tau_3 = +1) + \delta g_S(\tau_3 = -1) = 0, \tag{A.9}$$

because of the isovector character of the mesonic exchange currents. Then, the isoscalar magnetic moment is given in units of the nuclear magneton as

$$\begin{aligned}\mu^{(0)} &= \Big[(\langle\ell_z\rangle_S + \delta\langle\ell_z\rangle_{CM})\left\{g_\ell^{(0)} + \left(\delta g_{\ell EX}^{(0)}(1+\kappa) + \kappa g_\ell^{(0)}\right)\right\} \\ &\quad + (\langle S_z\rangle_S + \delta\langle S_z\rangle_{CM})\left\{g_S^{(0)} + \left(\delta g_{SEX}^{(0)}(1+\kappa) + \kappa g_S^{(0)}\right)\right\}\Big]. \qquad \text{(A.10)}\end{aligned}$$

Here, $\delta\langle\ell_z\rangle_{CM}$ and $\delta\langle S_z\rangle_{CM}$ are the configuration-mixing corrections to the orbital and spin angular-momentum expectation values; $g_\ell^{(0)}$ and $g_S^{(0)}$ are the orbital and spin isoscalar g-factor for single particles. Provided that nucleon effective g-factors are obtained experimentally, the degree of renormalization, κ, of the proton mass is given as

$$\kappa = \frac{g_\ell^{(0)}(\text{experiment}) - g_\ell^{(0)}}{g_\ell^{(0)}} = \frac{\delta g_\ell^{(0)}(\exp)}{g_\ell^{(0)}} \qquad \text{(A.11)}$$

and

$$\kappa = \frac{g_S^{(0)}(\text{experiment}) - g_S^{(0)}}{g_S^{(0)}} = \frac{\delta g_S^{(0)}(\exp)}{g_S^{(0)}}. \qquad \text{(A.12)}$$

In order to extract an effective g-factor from the experimental values, corrections due to the spin-tensor term, the cross term between the configuration mixing and the mesonic exchange current, the relativistic process and core deformation corrections must be subtracted from the experimental isoscalar magnetic moments,

$$\begin{aligned}\mu_{exp}^{(0)} &- \left(\delta\mu_{cross}^{(0)} + \delta\mu_P^{(0)} + \delta\mu_{def}^{(0)} + \delta\mu_{rel}^{(0)}\right) \\ &= \left[(I - \langle S_z\rangle_{eff})\left(g_\ell^{(0)} + \delta g_\ell^{(0)}(\exp)\right) + \langle S_z\rangle_{eff}\left(g_S^{(0)} + \delta g_S^{(0)}(\exp)\right)\right]\mu_N. \text{(A.13)}\end{aligned}$$

Here, $\langle S_z\rangle_{eff} = \langle S_z\rangle_S + \delta\langle S_z\rangle_{CM}$ are values for the LS doubly closed shell ±1 nucleon nuclei given theoretically by IBA [5, 7, 8] or TK [6]; these values are listed in table A.3. Since the deformation correction, $\delta\mu_{def}^{(0)}$, does not contribute to the isoscalar magnetic moment, it does not affect these isoscalar g-factors. Also, $\delta\mu_{cross}^{(0)}$ and $\delta\mu_P^{(0)}$ are less than 1/100 and 2/30 of the relativistic correction, respectively, and thus do not appreciably contribute to the isoscalar g-factors, compared with the effects due to relativistic corrections.

By combining equations A.13 for $A = 39$ and $A = 41$ system, we can obtain the effective g-factors; the crossing point of the two solid lines for mass 41 and 39 in the $g_\ell - g_s$ graphs given in figure A.1 gives a set of effective g-factors. The lines shown in the figure were obtained by using the theoretical angular-momentum expectation value given by IBA, summarized in table A.4 with the theoretical values given by TK. If we take nuclear matrices from IBA, we obtain

$$\kappa = \frac{\delta g_\ell^{(0)}(\exp)}{g_\ell^{(0)}} = +2.7\% \qquad \text{(A.14)}$$

Table A.3: Spin expectation values of the LS doubly closed-shell ±1 nucleon nuclei

A		I^π	$\langle S_z\rangle_{exp}{}^{(a)}$	$\delta\langle S_z\rangle_{exp}/\langle S_z\rangle_S{}^{(b)}$	$\delta\langle S_z\rangle_{CM}/\langle S_z\rangle_S[\%]$		$\delta\mu_{rel}/\mu_S{}^{(e)}$
			[nm]	[%]	IBA$^{(c)}$	TK$^{(d)}$	[%]
15	^{15}N	1/2$^-$					9.8
	^{15}O	1/2$^-$					2.0
			-0.0845(11)	-49.3(7)	-67.36	-53.7	
17	^{17}O	5/2$^+$					-0.5
	^{17}F	5/2$^+$					-1.9
			+0.4326(16)	-13.5(3)	-22.36	-15.2	
39	^{39}K	3/2$^+$					-37.0
	^{39}Ca	3/2$^+$					+0.8
			-0.1143(3)	-61.9(1)	-69.68	-54.1	
41	^{41}Ca	7/2$^-$					-0.4
	^{41}Sc	7/2$^-$					-2.2
			+0.4418(24)	-11.6(5)	-27.62	-19.4	

(a) $\langle S_z\rangle_{exp} = (\mu^{(0)}_{exp} - \frac{1}{2}I)/(\mu_P + \mu_n - \frac{1}{2})$.
(b) $\delta\langle S_z\rangle_{exp}/\langle S_z\rangle_S = \{\langle S_z\rangle_{exp} - \langle S_z\rangle_S\}/\langle S_z\rangle_S$.
(c) Theoretical values given by Ichii *et al.* [5].
(d) Theoretical values given by Towner *et al.* [6].
(e) Theoretical relativistic corrections given by Ohtsubo *et al.* [12].

and

$$\kappa = \frac{\delta g_S^{(0)}(\text{exp})}{g_S^{(0)}} = +13.9\%. \tag{A.15}$$

Although the two values are not in agreement, possible renormalization effects in the nucleon mass are suggested. In spite of the difference in the theoretical spin expectation values given by TK and by IBA for each mass system, the results obtained by using TK were similar to those seen with IBA, as

$$\kappa = \frac{\delta g_\ell^{(0)}(\text{exp})}{g_\ell^{(0)}} = +3.9\% \tag{A.16}$$

and

$$\kappa = \frac{\delta g_S^{(0)}(\text{exp})}{g_S^{(0)}} = +3.1\%. \tag{A.17}$$

Therefore, a renormalization effect is shown for mass 40 from both the g_ℓ and g_S values, simultaneously; the nucleon mass in the nuclei of this mass region was less than that of the free nucleon by about 3%.

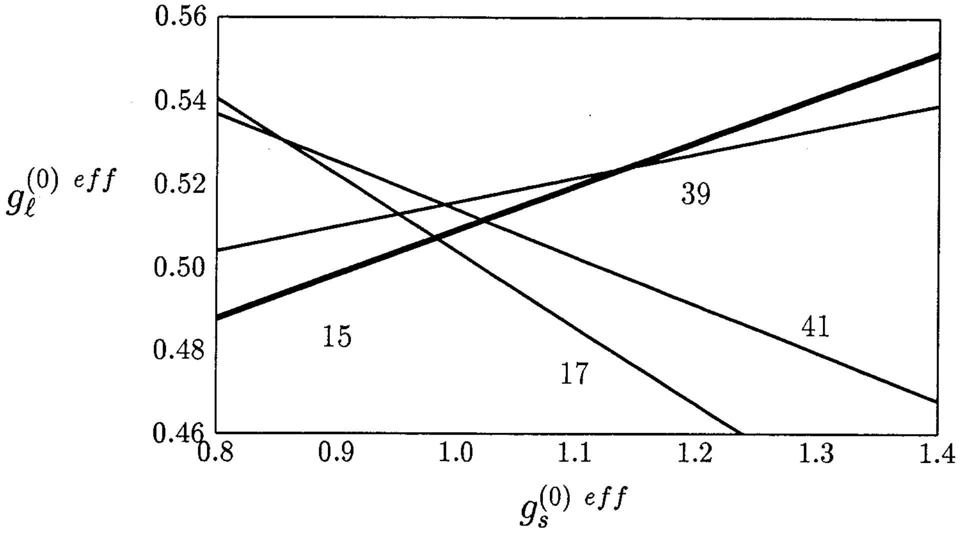

Figure A.1: Effective isoscalar g-factors obtained from LS doubly closed-shell ±1 nucleon nuclei.
Isoscalar magnetic moments are plotted using the matrix elements given by Ichi *et al.* The width shown for each bold line indicates each experimental error.

Table A.4: Isoscalar g-factors and quark deconfinement

	Matrix from IBA		Matrix from TK	
	mass-16	mass-40	mass-16	mass-40
$g_\ell^{(0)}$(experiment)	0.507	0.515	0.511	0.521
$g_S^{(0)}$(experiment)	0.983	0.987	0.928	0.962
$\delta g_\ell^{(0)}(\mathrm{exp})/g_\ell^{(0)}(\%)$	1.4	3.0	2.4	4.2
$\delta g_S^{(0)}(\mathrm{exp})/g_S^{(0)}(\%)$	11.7	12.2	5.5	9.3

Nuclear matrices were obtained from IBA [5, 7, 8] and TK [6]. Relativistic corrections were obtained from Ohtsubo *et al.* [12].

Effective g-factors of the proton and neutron

An analysis similar to those given above was carried out concerning the isovector magnetic moments of nuclei around mass 40 and 16, respectively,

$$\begin{aligned} \mu_{exp}^{(1)} &- \left(\delta\mu_{cross}^{(1)} + \delta\mu_P^{(1)} + \delta\mu_{def}^{(1)} + \delta\mu_{rel}^{(1)}\right) \\ &= \left(\langle\tau_3\ell_z\rangle_{eff} g_\ell^{(1)}(\mathrm{exp}) + \langle\tau_3 S_z\rangle_{eff} g_S^{(1)}(\mathrm{exp})\right)\mu_N, \end{aligned} \tag{A.18}$$

where $\langle\tau_3 S_z\rangle_{eff} = \langle\tau_3 S_z\rangle_S + \delta\langle\tau_3 S_z\rangle_{CM}$. The isovector orbital angular-momentum expectation value is given by $\langle\tau_3\ell_z\rangle_{eff} = \langle\tau_3\ell_z\rangle_S + \delta\langle\tau_3\ell_z\rangle_{CM}$, where $\delta\langle\tau_3\ell_z\rangle_{CM}$ is derived from the relation

$$\delta\mu^{(1)}_{CM} = g^{(1)}_{\ell}\,\delta\langle\tau_3\ell_z\rangle_{CM} + g^{(1)}_{S}\,\delta\langle\tau_3 S_z\rangle_{CM}. \tag{A.19}$$

$\delta\mu^{(1)}_{CM}$ and $\delta\langle\tau_3 S_z\rangle_{CM}$ are obtained from IBA. By definition, the $g^{(1)}_{\ell}$ and $g^{(1)}_{S}$ values are the free orbital and spin isovector g-factors. Note that in equation A.19, $\delta\mu^{(1)}_{CM}$ ($\delta\langle\tau_3 S_z\rangle_{CM}$) does not include the contribution from the tensor term, $\delta g_{PCM}\langle\tau_3 Y \times S\rangle_S$ ($\delta f_{SPCM}\langle\tau_3 S_z\rangle_S$) ,that is, $\delta\mu^{(1)}_{CM} = \delta g_{\ell CM}\langle\tau_3\ell_z\rangle_S + g_{SCM}\langle\tau_3 \S_z\rangle_S$ ($\delta\langle\tau_3 S_z\rangle_{CM} = \delta f_{SSCM}\langle\tau_3 S_z\rangle_S$ + $\delta f_{S\ell CM}\langle\tau_3 S_z\rangle_S$).

The effective isovector g-factors of A=16 and A=40 nuclei can be obtained from the combination of the equations for A=15, 17 and the combination for A=39, 41, respectively, as shown in table A.5. Furthermore, we obtained the effective g-factor of the proton and neutron by combining the results of the isoscalar moment and the isovector moment. As seen in table A.5, $g^{(1)}_{\ell}$ in mass 40 system is in fairly agreement with that in mass 16 system, while $g^{(1)}_{S}$ in mass 40 system is about 17% smaller than that in mass 16 system. This disagreement can mean that there is another unknown mechanism besides exchange currents, which makes a contribution to magnetic moments. However, the isovector values derived in the analysis are very much dependent on the choice of the deformation and relativistic corrections. More reliable values of corrections and information concerning the core deformation of the core are needed in order to give conclusive results for individual proton and neutron g-factors. Since a core deformation has direct relation to the charge distribution in a concerned nucleus, its quadrupole moment can be used as a probe of the core deformation, as explained in the discussion section.

Table A.5: Effective g-factors in the mass 16 and 40 system

Nuclear matrices and isoscalar and isovector $\langle SY_2\rangle$ values were obtained from IBA. A relativistic correction was obtained from Ohtsubo *et al*[12]. Isoscalar g-factors are given in table A.4. The errors are due to experimental uncertainties only.

	Mass-16	Mass-40	Free values
$g^{(1)}_{\ell}$(experiment)	0.725	0.793	0.500
$g^{(1)}_{S}$(experiment)	4.581 ± 0.002	3.817 ± 0.002	4.706
δg_{ℓ}(proton)	0.232	0.308	
δg_{ℓ}(neutron)	-0.218	-0.278	
δg_{S}(proton)	-0.0217	-0.782	
δg_{S}(neutron)	0.228	0.996	

Appendix B

Asymmetry parameter of β-decay

The asymmetry parameter, A, of β-decay with a change in the nuclear spin, $I_i \to I_f$, is written as

$$\begin{aligned} A &= \frac{\pm|C_A|^2|\langle\sigma\rangle|^2\Delta_{if} - 2C_V^*\langle 1\rangle^* C_A\langle\sigma\rangle\sqrt{I_i/(I_i+1)}}{|C_V|^2|\langle 1\rangle|^2 + |C_A|^2|\langle\sigma\rangle|^2} \\ &= \frac{\pm R^2|\langle\sigma\rangle|^2\Delta_{if} - 2R\langle 1\rangle^*\langle\sigma\rangle\sqrt{I_i/(I_i+1)}}{|\langle 1\rangle|^2 + R^2|\langle\sigma\rangle|^2}, \end{aligned} \tag{B.1}$$

where R is the ratio, $R = C_A/C_V$, of the Gamov-Teller coupling constant, C_A, to the Fermi coupling constant, C_V, and the coefficient Δ_{if} is

$$\Delta_{if} = \begin{cases} 1 & \text{if } I_f = I_i - 1 \\ \frac{1}{I_i+1} & \text{if } I_f = I_i \\ -\frac{I_i}{I_i+1} & \text{if } I_f = I_i + 1. \end{cases} \tag{B.2}$$

The upper sign in A is applied to β^+-decay, and the Fermi matrix element, $\langle 1\rangle$, and the Gamov-Teller matrix element, $\langle\sigma\rangle$, are described as follows:

$$|\langle 1\rangle|^2 = \left|\int 1\right|^2 = T(T+1) - T_3^i T_3^f, \tag{B.3}$$

$$\begin{aligned} |\langle\sigma\rangle|^2 &= \left|\int\sigma\right|^2 \\ &= \begin{cases} \frac{I_i+1}{I_i}|K|^2 & \text{if } I_i = l + \frac{1}{2} \to I_f = l + \frac{1}{2} \\ \frac{2I_i-1}{I_i}|K|^2 & \text{if } I_i = l + \frac{1}{2} \to I_f = l - \frac{1}{2} \\ \frac{2I_i+3}{I_i+1}|K|^2 & \text{if } I_i = l - \frac{1}{2} \to I_f = l + \frac{1}{2} \\ \frac{I_i}{I_i+1}|K|^2 & \text{if } I_i = l - \frac{1}{2} \to I_f = l - \frac{1}{2}. \end{cases} \end{aligned} \tag{B.4}$$

Here, l is the angular momentum of the nucleus, $T = (T_1, T_2, T_3)$ is the isospin of the nucleus, and K is the radial, integration

$$K = \int \phi_f^* \phi_i r^2 dr. \tag{B.5}$$

The half-life, $t_{1/2}$, in nuclear β-decay is represented as

$$ft_{1/2} = \frac{B}{|\langle 1\rangle|^2 + R^2|\langle\sigma\rangle|^2}, \tag{B.6}$$

where f denotes the phase-space volume; $B = 6168(4)$ sec is a coupling constant in nuclear β-decay [42, 43]. From the ft value of the free neutron decay, $|R| = |C_A/C_V| = 1.254(6)$ was deduced [44].

In case of the decay $^{41}\mathrm{Sc}(I^\pi = 7/2^-) \rightarrow {}^{41}\mathrm{Ca}(I^\pi = 7/2^-) + \beta^+$, by using $K = 1$, due to the mirror decay, and equations B.2, B.3 and B.4, the asymmetry parameter was deduced to be

$$A = 0.98. \tag{B.7}$$

Appendix C

Program list for NNQR detection

NNQR control and detection was performed by using personal computers. The program for data-taking involved monitoring and control of the RF system and the detection system. The program for monitoring the data was written in BASIC language, and that for control in macro assembler. Here, the part of the control for the NNQR is explained and, the program for control and the macros used in the program are listed.

macro *parameters*

explanation

in_sem *adctsem,ctch*

reads the beam current. *adctsem* is an address of the data and *ctch* is a channel of the counter board.

bpcntr *port,function,endmode,time*

outputs the bit-pattern given by *function* to the *port*. *endmode* is the bit-pattern at the end of output during the time indicated by *time*. This macro is used for the control of the beam and rf's. For example,

```
bpcntr rfport,045h,044h,lpulse
```

outputs the bit-pattern `0100 0101` to the `rfport` as the pulse signal and sets the bit-pattern of the `rfport` `0100 0100`. In other words, this macro outputs the pulse from the lowest bit of the `rfport`.

wtloopl *time1, time2*

waits for the time indicated by *time1* and *time2*. *time1* is for a global adjustment and *time2* for a fine adjustment.

bmcool

inserts a short time to ensure that the beam current stops completely.

rfdtout *rfdtout, adrfdt*

outputs rf data to control the synthesizer. However, this function was not available in the present experiment. This exists for compatibility with other control programs.

daout *adrfdt, dachl, dachh, dadtl, dadth*

controls the DAC. *dachl* and *dachh* are the data for the module channel of DAC and *dadtl* and *dadth* for the digital data representing to the DC level responding the necessary frequency.

count *bitpattern, ctch, incad, cttime1, cttime2*

opens the channel *ctch* of the counter board during the time indicated by *cttime1* and *cttime2*. This macro sets the bit-pattern of the port of indicating the status of the counting routine *bitpattern*.

countin

gets the number of received signals from the counter board into the memory of the computer.

rfadinc

increases the address of the rf data.

Program list

```
;       NMR control program
;                         by S. Fukuda
;
;       2AP MODE (RF ON / OFF + BACKGROUND)
;                                         RF 1,2,3,4,5,6,7 * 14
;                                         by VCO RF control (use DA board)
;
;       2APCNTRD.M
;
        title 2APCNTRD Main routine
if1
        %out Now 2APCNTRD.ASM has been compiled
endif
;
;       include for initialization
;
        include lab\lab1cntr.asm
;
        ctadinc 04h
;
main:
        in_sem  adctsem,ctch5
```

```
        bpcntr  bmport,bmstart,off,lpulse
        wtloopl bmtime1,bmtime2
        bpcntr  bmport,bmstop,off,lpulse
;
        bmcool
;
        rfdtout adrfdt
        bpcntr  rfport,rfon,rfon,lpulse
        push    cx
        mov     cx,0Eh                                  ; for 14 rf loop

rflp1:  push    cx

        daout   adrfdt,dach1l,dach1h,dadt1l,dadt1h
        bpcntr  rfport,045h,044h,lpulse        ; for ramp gen. 0100 0101
        wtloopl rftime1,rftime2

        daout   adrfdt,dach1l,dach1h,dadt2l,dadt2h
        bpcntr  rfport,025h,024h,lpulse        ; for ramp gen. 0010 0101
        wtloopl rftime1,rftime2

        daout   adrfdt,dach1l,dach1h,dadt3l,dadt3h
        bpcntr  rfport,015h,014h,lpulse        ; for ramp gen. 0001 0101
        wtloopl rftime1,rftime2

        daout   adrfdt,dach1l,dach1h,dadt4l,dadt4h
        bpcntr  rfport,00Dh,00Ch,lpulse        ; for ramp gen. 0000 1101
        wtloopl rftime1,rftime2

        daout   adrfdt,dach1l,dach1h,dadt5l,dadt5h
        bpcntr  rfport,015h,014h,lpulse        ; for ramp gen. 0001 0101
        wtloopl rftime1,rftime2

        daout   adrfdt,dach1l,dach1h,dadt6l,dadt6h
        bpcntr  rfport,025h,024h,lpulse        ; for ramp gen. 0010 0101
        wtloopl rftime1,rftime2

        daout   adrfdt,dach1l,dach1h,dadt7l,dadt7h
        bpcntr  rfport,045h,044h,lpulse        ; for ramp gen. 0100 0101
        wtloopl rftime1,rftime2

        pop     cx
        dec     cx
        jcxz    cont1
        jmp     rflp1
cont1:  pop     cx

        bpcntr  rfport,rfoff,rfoff,lpulse
        rfkill
;
```

```
        count   00000001b,01h,3ch,cttime1,cttime2
        countin
;
        count   00000010b,01h,04h,cttime5,cttime6
                countin
        rfadinc
;
        dec     cx
        jcxz    extgl
        jmp     main
;
extgl:
        countin
        in_sem  adctsem,ctch5
;
;       include for termination
;
        include lab\lab2cntr.asm
;
        end
```

Appendix D

Synthesis of TiO_2(Sc) crystal

To measure the electric-field gradient at a Ti site in a TiO_2 crystal, a TiO_2 crystal with Sc atoms was synthesized by Earth Jewelry Company.[1] The concentration of ^{45}Sc atoms in the crystal was dilute, 0.5% (atomic per cent relative to the Ti atoms in the crystal). A proper amount of $^{45}Sc_2O_3$ powder was mixed into the TiO_2 and the velocity of the crystal growth was 10 mm/hr for 3 hours. After growth, it was annealed for 3 hours. The size of the synthesized crystal was about $15\phi \times 30$ mm^3.

The crystallographic axis of the crystal was determined based on the diffraction of X-rays with the Laue method. A typical Laue pattern of the synthesized crystal is shown in a figure D.1. In the Laue pattern we confirmed the 4-fold axis corresponding to the c-axis in the mixed crystal.

---

[1] Earth Jewelry Company, Ikeda, Osaka, Japan.

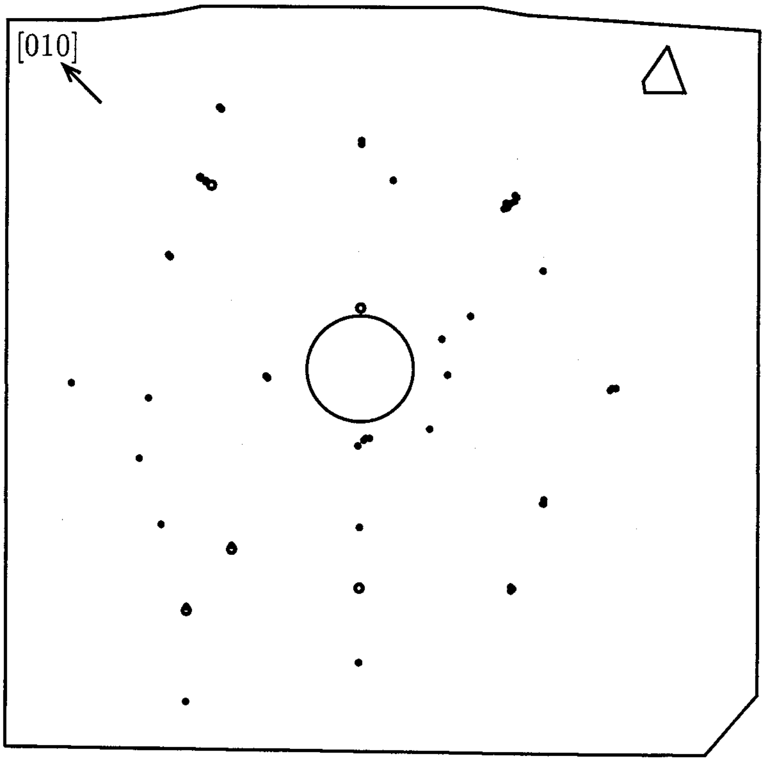

Figure D.1: Laue pattern of a TiO$_2$(Sc) crystal.

Appendix E

Multiconfiguration of Hartree-Fock method (MCHF)

The Hartree-Fock approach is a method used for obtaining approximate total wavefunctions for many-electron systems. It has been successfully applied to many areas of quantum mechanics, including atomic, molecular, and solid-state systems. The method is based on both the central-field approximation and the variational principle. Furthermore, the multiconfiguration Hartree-Fock method is an extended Hartree-Fock method allowing mixing of the configurations making the same state. The mixing coefficients can also be determined variationally, as well as the radial functions. This enables us to construct the better approximate total wavefunctions for the state of the concerned system than the simple Hartree-Fock method.

E.1 Variational principle

Schrödinger's equation for the study of a many-electron system,

$$\mathcal{H}\psi = E\psi, \tag{E.1}$$

is a fundamental equation of quantum mechanics. In this equation E is the total energy of the system, ψ is called the total wavefunction, which describes the state of the system, and $\mathcal{H}$ is the Hamiltonian of the system. For an N-electron atomic system the non-relativistic Hamiltonian, in atomic units,[1] is given by

$$\mathcal{H} = \frac{1}{2}\sum_{i=1}^{N}\left(\nabla_i^2 + \frac{2Z}{r_i}\right) + \sum_{i>j}\frac{1}{r_{ij}}. \tag{E.2}$$

where, Z is the atomic number, r_i the distance of the ith electron from the nucleus, and r_{ij} the distance between the ith and jth electron.

---

[1] $m_e = 1$, $e = 1$, $\hbar = 1$

For bound-state systems the exact total wavefunction, ψ, is an N-electron function for which $\langle\psi|\psi\rangle$ is bounded. From equation E.1 it follows that

$$\langle\psi|\mathcal{H}-E|\psi\rangle = 0, \tag{E.3}$$

and

$$E = \frac{\langle\psi|\mathcal{H}|\psi\rangle}{\langle\psi|\psi\rangle}. \tag{E.4}$$

By considering a variation, $\psi+\delta\psi$, about ψ, the exact solution, we obtain the following equations to first order in $\delta\psi$:

$$\begin{aligned}\delta\langle\psi|\mathcal{H}-E|\psi\rangle &= \langle\delta\psi|\mathcal{H}-E|\psi\rangle + \langle\psi|\mathcal{H}-E|\delta\psi\rangle \\ &= 2\langle\delta\psi|\mathcal{H}-E|\psi\rangle,\end{aligned} \tag{E.5}$$

since $\mathcal{H}$ is Hermitian for bound-state functions. Since the exact function satisfies equation E.1,

$$\langle\delta\psi|\mathcal{H}-E|\psi\rangle = 0 \tag{E.6}$$

for all variations, $\delta\psi$, such that $\langle\psi+\delta\psi|\psi+\delta\psi\rangle$ remains bounded.

Now, let Ψ be an approximate solution of prescribed functional form and consider an arbitrary variation, $\delta\Psi$, such that $\Psi+\delta\Psi$ has the same functional form. The equations

$$\langle\Psi|\mathcal{H}-E|\Psi\rangle = 0 \tag{E.7}$$

and

$$\langle\delta\Psi|\mathcal{H}-E|\Psi\rangle = 0 \tag{E.8}$$

define the best approximation that is consistent with our form. The solutions of equations E.7 and E.8 are functions that leave the energy functional

$$E(\Psi) = \frac{\langle\Psi|\mathcal{H}|\Psi\rangle}{\langle\Psi|\Psi\rangle} \tag{E.9}$$

stationary to the first order. The Hartree-Fock equations are derived using the stationary property of this energy functional.

E.2 Hartree-Fock approximation

The Hartree-Fock method for obtaining an approximation to the total wavefunction consists of three stages. In the first, a functional form is selected and defined in terms of certain functions to be determined later. Then, the expression for the total energy is derived in terms of these functions. Finally, the variational principle is applied and the equations are derived whose solutions are functions that leave the total energy stationary.

There are many variations of the Hartree-Fock approach. Although they differ in the way in which the functional form is defined, they must satisfy the following assumptions [45]: 1) antisymmetry, 2) products of spin-orbitals, and 3) orthogonality.

Antisymmetry

Let p_{ij} be an operator that, when applied to a many electron wavefunction, interchanges the four coordinates, three space coordinates and a spin coordinate, of electron i with those of electron j. Then, the physically significant solution, ψ, of the equation E.1 are those for which

$$p_{ij}\psi = -\psi \tag{E.10}$$

for all $i, j \leq N$, $i \neq j$. A Hartree-Fock approximation, Ψ, must satisfy the asymmetry conditions.

Products of spin-orbitals

An approximate total wavefunction can be obtained by replacing the Hamiltonian, $\mathcal{H}$, by one for which the wave equation is solvable,

$$\mathcal{H} \approx \hat{\mathcal{H}} = \sum_{i=1}^{N} \left\{ \frac{1}{2}\nabla_i^2 - \frac{Z}{r_i} + V(r_i) \right\}, \tag{E.11}$$

where the effect on interactions with other electrons has been replaced by a single-particle potential, V. The wavefunction, Φ, which is an approximation to ψ, gained from the eigenvalue problem,

$$\hat{\mathcal{H}}\Phi = \hat{E}\Phi, \tag{E.12}$$

is separable as

$$\Phi = \phi(1)\phi(2)\cdots\phi(i)\cdots\phi(N), \tag{E.13}$$

where $\phi(i)$ is a one-electron wavefunction for electron i. The one-electron wavefunction satisfies the equation

$$\left[\frac{1}{2}\nabla_i^2 - \frac{Z}{r_i} + V(r_i)\right]\phi(i) = E_i\phi(i), \tag{E.14}$$

which is the wave equation for a particle in a central field, and is represented by

$$\phi(r, \theta, \varphi, \sigma) = \left(\frac{1}{r}\right) P(r) Y_{lm_l}(\theta, \varphi)\chi_{m_s}, \tag{E.15}$$

where $Y_{lm_l}(\theta,\varphi)$ is a spherical harmonic and χ_{m_s} a spin function. The radial function, $P(r)$, is now a solution of the radial Schrödinger, equation

$$\left[\frac{d^2}{dr^2}+\frac{2Z}{r}-2V(r)-\frac{l(l+1)}{r^2}-\varepsilon\right]P(r)=0, \qquad \varepsilon=-2E_i, \tag{E.16}$$

with boundary conditions $P(0)=P(\infty)=0$.

Suppose we have a set of N quantum numbers $\{n_jl_jm_{l_j}m_{s_j}\}$, and let $\phi_j(i)$ be an orbital for the jth set of quantum numbers in terms of the space and spin coordinates of the ith electron: $r_i,\theta_i,\varphi_i,\sigma_i$. Then, using an antisymmetrizing operator, $\mathcal{A}$, to yield an antisymmetric function, the approximate total wavefunction is represented as

$$\begin{aligned}\Phi &= \mathcal{A}\{\phi_1(1)\phi_2(2)\cdots\phi_N(N)\}\\ &= \left(\frac{1}{N!}\right)^{1/2}\sum_{\mathcal{P}}(-1)^p\mathcal{P}\{\phi_1(1)\phi_2(2)\cdots\phi_N(N)\}\\ &= \frac{1}{(N!)^{1/2}}\begin{vmatrix}\phi_1(1) & \phi_1(2) & \dots & \phi_1(N)\\ \phi_2(1) & \phi_2(2) & \dots & \phi_2(N)\\ \vdots & \vdots & \ddots & \vdots\\ \phi_N(1) & \phi_N(2) & \dots & \phi_N(N)\end{vmatrix},\end{aligned} \tag{E.17}$$

where $\mathcal{P}$ is an operator which permutes the coordinates of the electrons, p is the parity of the permutation, and the sum is over all $N!$ possible permutations. The last representation is the Slater determinant for a set of spin-orbitals.

The difficulty with this approach for defining approximate many-electron wavefunctions lies in selecting an appropriate one-electron potential, $V(r)$. The Hartree-Fock method avoids this problem by simply the following requirement:
Ψ must consist of sums of products of N spin-orbitals of the form,

$$\phi_{nlm_lm_s}(r,\theta,\varphi,\sigma)=\left(\frac{1}{r}\right)P(r)Y_{lm_l}(\theta,\varphi)\chi_{m_s}, \tag{E.18}$$

where the precise form of the radial function is not specified in the first stage except that it is a twice-differentiable, square-integralable function.

Orthogonality

As long as the radial functions for a given value of l are all eigenfunctions of the same radial equation, they are orthogonal. However, the Hartree-Fock conditions do not impose this constraint. Instead it is usually required that the spin-orbitals should form an orthonormal set; that is,

$$\int\phi_{nlm_lm_s}(1)\phi_{n'l'm_l'm_s'}(1)d\tau_1=\delta_{nn'}\delta_{ll'}\delta_{m_lm_l'}\delta_{m_sm_s'}, \tag{E.19}$$

where $d\tau_1$ represents integration over all space coordinates and summation over the spin coordinates of electron 1.

E.3 Multiconfiguration of Hartree-Fock method

The multiconfiguration Hartree-Fock (MCHF) approach assumes that

$$\Psi(\gamma LS) = \sigma_i c_i \Phi(\gamma_i LS), \tag{E.20}$$

where not only the radial functions, $P(nl\ldots;r)$, must be determined variationally, but also the mixing coefficients, c_i. The equation E.20 assumes that

$$\sum_i c_i^2 = 1 \tag{E.21}$$

and

$$\langle \Phi(\gamma_i LS) | \Phi(\gamma_j LS) \rangle = \delta_{ij}. \tag{E.22}$$

Here, $\Phi(\gamma LS)$ is an eigenfunction of $\boldsymbol{L}^2$ and $\boldsymbol{S}^2$ and γ represents the configuration, the coupling scheme, and any other quantum numbers required to denote a particular LS term.

By allowing mixing the configuration, the total approximate wave function can come near the exact wavefunction. For example, we consider the two-electron system, He. As shown in table E.1, the total energy obtained by the multiconfiguration Hartree-Fock

Table E.1: Convergence of an MCHF procedure for $1s^2\ ^1S$ of He

Table was cited from ref.[45].

m	Configuration	E_{total}
1	$1s^2$	-2.861680
2	$+2s^2$	-2.877997
3	$+3s^2$	-2.878871
4	$+4s^2$	-2.878990
5	$+2p^2$	-2.898554
6	$+3p^2$	-2.990150
7	$+4p^2$	-2.900399
8	$+3d^2$	-2.902179
9	$+4d^2$	-2.902523
10	$+4f^2$	-2.902909
11	$+5g^2$	-2.903033
E^{exact}		-2.903724
$E - E^{exact}$		0.000691

procedure converges more nearly on the exact energy, as the number of configurations increases.

As another example of MCHF calculation, we consider the $3s\ ^2S$-$3p\ ^2P$ transition in Na [46]. By including the core polarization, the wavelengths for the transition were estimated in excellent agreement with observation for the lower degrees of ionization: for the higher members the lack of agreement was almost entirely due to relativistic effects. The length and velocity form of the f-value are seen to agree to within 1%. In this calculation, the core polarization made a great contribution to the wavelengths and f-values

Table E.2: Wavelengths and f-values for the $3s^2S$-$3p^2P$ transition in the Na isoelectronic sequence

	λ(Å)			f-value		
Atom	Theoretical	Observed	Difference (%)	Length	Velocity	Difference (%)
Na	5907.5	5891.8	0.27	0.962	0.969	-0.69
Mg^{+}	2802.5	2797.9	0.16	0.912	0.913	-0.09
Al^{+2}	1861.2	1857.4	0.20	0.834	0.832	0.29
Si^{+3}	1401.8	1396.7	0.37	0.762	0.758	0.50
Si^{+5}	945.2	937.07	0.87	0.645	0.639	0.81
Ar^{+7}	715.8	704.87	1.55	0.557	0.552	0.92
Ca^{+9}	577.1	563.6	2.40	0.490	0.485	0.96
Fe^{+15}	366.2	343.2	6.70	0.359	0.356	0.92

It should be noticed that the resulting configurations like the core polarization often make important contributions to the atomic property. In fact, the calculation of the electric field gradient of the atom could be dependent on the configurations of inner core, as shown in the discussion on the Ca case.

Appendix F

Sternheimer effect

In general, the nucleus with the spin $I \geq 1$ has an electric quadrupole moment Q. The energy of the atomic system including the nucleus can be represented by the product of Q and q, the electric field gradient at the nucleus. Therefore, we can reduce only the value $q \cdot Q$ from a constant of hyperfine interaction obtained from experiments such as observing the atomic spectrum and the nuclear magnetic resonance. Though we need to know q in order to obtain Q, there is no way to measure q directly.

Because q is caused by the electrons composing the atom, we can calculate q theoretically. As an example, let's consider the case where we calculate q of the atom with the Hartree-Fock approximation. If we assume that each orbit of electrons is the eigenstate of the angular momentum, s-electron and the electrons in the inner core don't produce q because their charge distributions are spherical; only valance electron with the aspherical orbit can produce q. However, because this valance electron can interact with the core electrons and s-electrons, the core electrons and s-electrons contribute q. R. M. Sternheimer estimated this contribution by use of the perturbation theory and indicated that when the electrons like p electron exist outside the inner core, the inner core can be polarized by the interaction with the valance electrons and can produce the significant q with the small decrease of the total energy [47]. This is because that the charge distribution of the nucleus's vicinity, especially, the polarization of the inner core can make a great contribution to q. This polarization of the inner core can make an effect screening q, therefore, Q is larger than the value with no consideration of the polarization of the inner core. This effect is called Sternheimer effect.

Above-mentioned effect can be expressed in the following formulation [23] and schematically in figure F.1. The perturbating potential is considered to originate from a charge distribution of $w(1)$. The direct interaction of $w(1)$ with a point at the perturbed site could be written as

$$H_1(3) = \langle w(1)|\frac{e^2}{r_{13}}(1 - P_{13})|w(1)\rangle, \tag{F.1}$$

where P_{13} is the operator which interchanges coordinates 1 with coordinates 3 and account for the exchange interaction. The expectation value of H_1 over $v(3)$ gives the perturbation energy of the site

$$E_1 = \langle v|H_1|v\rangle. \tag{F.2}$$

The charge distribution $w(1)$ interacts with the closed-shell electrons $u_0(2)$ in a similar way. The proper equation for an unperturbed function u_0,

$$H_0 u_0 = E_0 u_0 \tag{F.3}$$

is considered after introducing the perturbation $H_1(2)$, and is solved for u_1 in the perturbed function $u_0 + u_1$ from the usual second perturbation theory relation

$$(H_0 - E_0)u_1 = -(H_1 - E_1)u_0. \tag{F.4}$$

We have

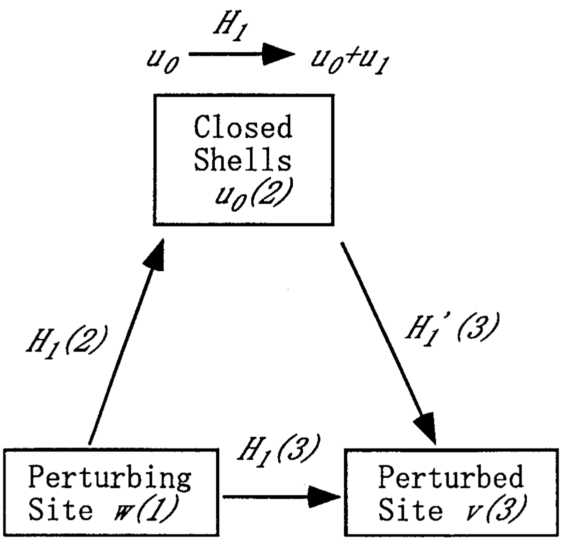

$$\text{Sternheimer effect} = -\frac{\langle V|H_1'|V\rangle}{\langle V|H_1|V\rangle} \tag{F.5}$$

Figure F.1: Schematic diagram showing Sternheimer effect

$$\begin{aligned} E_1 = \langle u_0|H_1|u_0\rangle &= 0 \qquad (F.6)\\ \langle u_1|U_0\rangle &= 0. \qquad (F.7) \end{aligned}$$

The charge distribution $u_0 + u_1$ interacts with $v(3)$ via

$$H_1'(3) = \langle u_0 + u_1 | \frac{e^2}{r_{23}} (1 - P_{23}) | u_0 + u_1 \rangle. \tag{F.8}$$

The term

$$\langle u_0 | \frac{e^2}{r_{23}} (1 - P_{23}) | u_0 \rangle \tag{F.9}$$

summed over all electrons in a closed shell vanishes. Out of the remaining two terms the leading term

$$2 \langle u_0 | \frac{e^2}{r_{23}} (1 - P_{23}) | u_1 \rangle \tag{F.10}$$

is of second order. The expectation value of H_1' over $v(3)$ gives the Sternheimer perturbation energy of the site;

$$E_1' = \sum_{\text{all core electrons}} \langle v | H_1' | v \rangle. \tag{F.11}$$

The Sternheimer parameter is defined as

$$R = -\frac{E_1'}{E_1} \tag{F.12}$$

and some Sternheimer parameters are listed in table F.1.

Table F.1: Sternheimer parameter

Ion	R_0	Ion	R_0	Ion	R_0
Li^+	0.261	Sc	-0.085	Cr^+	0.021
Ti^+	-0.028	Sc^+	-0.078	Mn^+	0.034
V^+	0.002	Sc^{2+}	-0.018	Fe^+	0.043

Appendix G

Skyrme type interaction

The Skyrme interaction is one of the effective interactions between nucleons, which T. H. R. Skyrme offered for allowing for the presence of many-body effects in the shell-model description [48]. Skyrme interaction is composed of the two-body interaction and the tree-body interaction

$$V = \sum_{i<j} t_{ij} + \sum_{i<j<k} t_{ijk}. \tag{G.1}$$

The two-body interaction is represented as the δ function

$$t_{ij} = \delta(\boldsymbol{r}_i - \boldsymbol{r}_j) t(\boldsymbol{k}, \boldsymbol{k}'), \tag{G.2}$$

and $t(\boldsymbol{k}, \boldsymbol{k}')$ is the quadratic equation of $\boldsymbol{k}$ or $\boldsymbol{k}'$. The three-body interaction is also represented as the δ function

$$t_{ijk} = t_3 \delta(\boldsymbol{r}_i - \boldsymbol{r}_j) \delta(\boldsymbol{r}_k - \boldsymbol{r}_i), \tag{G.3}$$

which implies the idea of G-matrix of the Brueckner's theorem [49] that the two nucleons interact under the influence of other nucleons. This three-body interaction can be reduced to the density-dependent two-body interaction by averaging t_{ijk} over the wave function of the particle k.

The parameters of the Skyrme interaction used in the Sagawa's calculation are as following. The two-body interaction $V(\boldsymbol{r}_1, \boldsymbol{r}_2)$ has density-independent terms and a density-dependent term

$$\begin{aligned} V(\boldsymbol{r}_1, \boldsymbol{r}_2) &= t_0(1 + x_0 P_\sigma)\delta(\boldsymbol{r}_1 - \boldsymbol{r}_2) + t_1(1 + x_1 P_\sigma)[\frac{1}{2}(\boldsymbol{k}'^2 + \boldsymbol{k}^2)]\delta(\boldsymbol{r}_1 - \boldsymbol{r}_2) \\ &\quad + t_2(1 + x_2 P_\sigma)\boldsymbol{k}' \cdot \delta(\boldsymbol{r}_1 - \boldsymbol{r}_2) + \frac{1}{6} t_3 (1 + x_3 P_\sigma)\rho^\alpha(\boldsymbol{R})\delta(\boldsymbol{r}_1 - \boldsymbol{r}_2), \end{aligned} \tag{G.4}$$

where $\boldsymbol{R} = \frac{1}{2}(\boldsymbol{r}_1 + \boldsymbol{r}_2)$, $\boldsymbol{k} = (\vec{\nabla}_1 - \vec{\nabla}_2)/2i$, and $\boldsymbol{k}' = (\vec{\nabla}_1 - \vec{\nabla}_2)/(-2i)$. The parameters are selected for having reasonable values for the Landau parameters in comparison with the renormalized G-matrix calculations while keeping realistic properties in the Hartree-Fock calculations. They used the parameter set SGII listed in table G.1, because this interaction gives a successful description for various nuclear collective excitations. The residual interaction V_{ph} can be derived by taking the second derivative of the energy density for equation G.4 with respect to densities [50]. This procedure is equivalent to the Landau prescription in the Fermi liquid theory. The ph interaction is given explicitly as

Table G.1: SGII parameter set

t_0	-2645 MeV·fm^3	x_0	$+0.09$
t_1	$+340$ MeV·fm^5	x_1	-0.0588
t_2	-41.9 MeV·fm^5	x_2	$+1.425$
t_3	15595 MeV·fm^6	x_3	$+0.06044$
	α	$1/6$	

$$\begin{aligned} V_{ph} &= \delta^2 E(\rho)/\delta\rho\delta\rho \\ &= \delta(\boldsymbol{r}_{12})\big\{a + b[\nabla_1^2 + \nabla_2^2 + \nabla_{1'}^2 + \nabla_{2'}^2 - (\nabla_1 - \nabla_{1'})(\nabla_2 - \nabla_{2'})] \\ &\quad + c(\nabla_1 + \nabla_{1'})(\nabla_2 + \nabla_{2'})\big\} \end{aligned} \tag{G.5}$$

with

$$\begin{aligned} a &= \frac{3}{4}t_0 + \frac{3}{48}(\alpha+2)(\alpha+1)t_3\rho^\alpha - \frac{1}{48}t_3(1+2x_3)\alpha(\alpha-1)\rho_t^2\rho^\alpha/\rho^2 \\ &\quad - \left[\frac{1}{4}t_0(1+2x_0) + \frac{1}{24}t_3(1+2x_3)\rho^\alpha\right]\boldsymbol{\tau}\cdot\boldsymbol{\tau}, \\ b &= -\frac{1}{32}\left\{3t_1 + t_2(5+4x_2) + [t_2(1+2x_2) - t_1(1+2x_1)]\boldsymbol{\tau}\cdot\boldsymbol{\tau}\right\}, \\ c &= \frac{1}{32}\left\{3t_1 - 3t_2(5+4x_2) - [t_1(1+2x_1) + 3t_2(1+2x_2)]\boldsymbol{\tau}\cdot\boldsymbol{\tau}\right\}, \end{aligned} \tag{G.6}$$

where $\rho_t = \rho_n - \rho_p$. In equation G.5, the indices 1, 1' refer to the ph (particle-hole) coordinates to the left and 2, 2' are those to the right. The spin-dependent terms are discarded in equation G.6.

Bibliography

[1] H. Sagawa and B.A. Brown, Nucl. Phys. A430(1984)84

[2] T. Minamisono et al., Phys. Rev. Lett. 69(1992)2058

[3] M. Arnold, J. Kowalski, T. Stehlin, F. Träger and G. zu Putliz, Z. Phys. A314(1983)303

[4] T. Minamisono, et al., Nucl. Phys. A516(1990)365

[5] S. Ichii, W. Bentz and A. Arima, Nucl. Phys. A464(1987)575

[6] I.S. Towner and F.C. Khanna, Nucl. Phys. A399(1983)334; Phys. Report 155(1987)264

[7] A. Arima, K. Shimizu, W. Bentz and H. Hyuga, Adv. Nucl. Phys. 18(1988)1

[8] K. Shimizu, H. Huga and A. Arima, Nucl. Phys. A336(1980)363

[9] T. Nomura, J. Phys. Soc. Japan 34 Suppl. (1973)331

[10] W.J. Gerace and A.M. Green, Nucl. Phys. A93(1967)110

[11] T. Minamisono, Y. Yasui, T. Ohtsubo, A. Kitagawa, Y. Matsuo and S. Takeda, Hyp. Int. 59(1990)153

[12] H. Ohtsubo, M. Sano and M. Morita, J. Phys. Soc. Jpn. 34(1973)509

[13] T. Minamisono, Y. Nojiri, A. Mizobuchi and K. Sugimoto, Nucl. Phys. A236(1974)416

[14] Y. Someda, I. Minamai, T. Ohtsubo, Y. Nakayama, A. Kitagawa, K. Matsuta, M. Fukuda, Y. Nojiri and T. Minamisono, OULNS(1990)68

[15] S. Fukuda, T. Ohtsubo, Y. Nakayama, M. Tanigaki, A. Kitagawa, Y. Someda, S. Takeda, M. Fukuda, K. Matsuta, Y. Nojiri and T. Minamisono, OULNS(1990)76

[16] A. Abragam, "The Principles of Nuclear Magnetism", Oxford Univ. Press(1961)

[17] T. Minamisono, J.W. Hugg, D.G. Mavis, T.K. Saylor, S.M. Lazarus, H.F. Glavish and S.S. Hanna, Phys. Rev. Lett. 34(1975)1465; Phys. Lett. B61(1976)155

[18] G. Fricke, H. Kopfermann, S. Penselin and K. Schlüpmann, Z. Phys. 156(1959)416

[19] W. Ertmer and B. Hofer, Z. Phys. A276(1976)9

[20] W.J. Childs, Phys. Rev. A4(1971)1767

[21] P. Pyykkö, Z. Naturforsh. 47a(1992)189

[22] R.M. Stermheimer, Phys. Rev. A6(1972)1702

[23] R.P. Gupta and S.K. Sen, Phys. Rev. A7(1973)850

[24] R.G. Cornwell, W. Happer, Jr., and J.D. McCullen, Phys. Rev. 141(1966)1106

[25] A.K. Dahr and K.H. Bhatt, Phys. Rev. C16(1977)792

[26] W.A. Richter, Van Der Merve, Merve, R.E. Julies and B.A. Brown, Nucl. Phys. A523(1991)325

[27] H. Kitagawa and H. Sagawa, Private communication; Nucl. Phys. A551(1993)16

[28] A. Bohr and B.R. Mottelson, "Nuclear structure, vol. 1", Benjamin, New York (1966)

[29] A. Bohr and B.R. Mottelson, "Nuclear structure, vol. 2", Benjamin, New York (1966)

[30] M.G van der Merwe, W.A. Richter, B.A. Brown, Nucl. Phys. A579(1994)173

[31] R. Aydin, W. Ertmer, and U. Johann, Z. Phys. A306(1982)1

[32] S. Salomonsson, Z. Phys. A316(1994)135

[33] D. Sundholm and J. Olsen, J. Chem. Phys. 38(1993)1

[34] C.F. Fischer, Comput. Phys. Commun. 64(1991)431

[35] P. Jönsson, Comput. Phys. Commun. 74(1993)399

[36] M. Arnold, K. Kowalski, T. Stehlin, F. Träger, and G. zu Putlitz, Z. Phys. A314(1983)303

[37] E. Bergmann, P. Bopp, CH. Dorsch, J. Kowalski, F. Träger, and G. zu Putlitz, Z. Phys. A294(1980)319

[38] A. Andl, K. Bekk, K. Göring, A. Hanser, G. Nowicki, H. Rebel, G. Schantz, and R.G. Thompson, Phys. Rev. C26(1982)2194

[39] P. Raghavan, J. Phys. Chem. Ref. Data 42(1989)189

[40] W.J. Gerace, A.M. Green, Nucl. Phys. A93(1967)110

[41] K. Shimizu, M. Ichimura, A. Arima, Nucl. Phys. A226(1974)282

[42] D.H. Wilkinson and B.E.F. Macefield, Nucl. Phys. A232(1974)58

[43] D.H. Wilkinson et al., Phys. Rev. C18(1978)401

[44] D.H. Wilkinson , Prog. Part. Nucl. Phys. 6(1981)325

[45] C.F. Fischer, "The Hartree-Fock method for atoms", John Wiley & Sons, Inc.(1977)

[46] C.F. Fischer, "Beam-Foil Spectroscopy 1", Plenum Press, p69(1976)

[47] R. Sternheimer, Phys. Rev. 80(1950)102

[48] T.H. R. Skyrme, Nucl. Phys. 9(1959)615

[49] K.A. Brueckner, C.A. Levenson and H.H. Mahmoud, Phys. Rev. 95(1954)217

[50] G.F. Bertsch and S.F. Tsai, Phys. Rep. 18(1975)125

[51] T. Awaya, "Data Analysis (Analog and Digital)", GAKUKAI PRESS CENTER (1983)

[52] H. Miyazawa, Prog. Theor. Phys. 6(1951)801

[53] T. Yamazaki, J.Phys. Japan 34 Suppl.(1973)17; Phys. Lett. B160(1985)227